Topological & conventional order of spinless fermions in 2D lattices

Dissertation
zur Erlangung des akademischen Grades
Doctor of Philosophy (Ph.D.)

vorgelegt von

Stefanos Kourtis

geboren am 02.03.1985 in Athen, Griechenland

Fachrichtung Physik
Fakultät für Mathematik und Naturwissenschaften
Technische Universität Dresden
2014

Eingereicht am 11.06.2014.
Verteidigt am 15.10.2014.
1. Gutachter: Prof. Dr. Jeroen van den Brink
2. Gutachter: Prof. Dr. Matthias Vojta

Στη Φώφη.

Acknowledgments

Throughout the last few years, I have had the privilege to interact with several colleagues, whose guidance and insight – and sometimes their wit and spirit – have shaped not only this dissertation, but also its author. Here, I wish to devote a few lines to express my gratitude to them, starting with Maria Daghofer, who has been the most influential one. In most occasions, a discussion with Maria on any problem, from gritty details to big-picture questions, has left me with the impression that she can immediately be not just one step ahead, but already hinting at the solution. In conjunction with sharing her remarkably sharp insight, Maria has also encouraged me to develop my own intuition, and has had the patience to put up with all the resulting quixotic endeavors and "experimental math". Reflecting upon all the interactions I have had with Maria so far, I converge to the conclusion that she has been an ideally suited mentor. Additionally, her generosity in all respects (there is never a shortage of books to read whenever Maria is around) and her sense of humor (including, but not limited to, the very apt usage of xkcd references) cannot be commended enough.

I owe a considerable amount of my understanding of the topics covered in this dissertation to the guidance of Jeroen van den Brink. When presented with a problem, Jeroen has always posed the most essential questions to ask, thus steering efforts towards the most intriguing results. Jeroen has also taught me the majority of what I know about x-ray scattering and has urged me into a successful collaboration with experimentalists, which led to my first interaction with condensed matter in the real world. Moreover, Jeroen has given me the soundest career advice I could have got at key moments, prompting me to invest some extra effort into my work at the right time – and then graciously granting me the time to do so – in order to get the most out of my stint as a PhD student. This dissertation – and perhaps everything that follows it – would not have been the same without his influence.

As if all of the above was not more than enough, Maria and Jeroen also gave me the opportunity to travel to conferences around the world and enjoy discussions with many knowledgeable colleagues – an opportunity which I have taken with great conviction by clocking in more than 90000 kilometers during my doctoral studies. Even though all these trips have been beneficial, some were particularly gratifying. The most memorable ones were my two visits to Claudio Chamon, who generously allowed me to set camp in his office in Boston for a bit more than a month each time. Claudio's almost childish excitement about physics, along with his mind-boggling breadth and depth of knowledge, have made him a role model for me. This collaboration was made even more fruitful and enjoyable by the contributions of Titus Neupert and Christopher Mudry. Another notable destination was Leeds, where Jiannis Pachos was pa-

tient enough to introduce me to Majorana fermions and their ways. The formalities of all business trips, as well as several other administrative issues, have been taken care of by Grit Rötzer, whose secretarial support and positive attitude has been phenomenal.

When I was not traveling, I was fortunate enough to collaborate with some truly remarkable colleagues. Valentina Bisogni immediately springs to mind, with her tireless determination to explain and to understand during our lengthy discussions and her pleasant temperament. Together, we arrived at a beautiful result, which, alas, did not find its way into this dissertation. The last in the list of collaborators, but without a doubt first in the list of comrades in science, is Jörn Venderbos. Apart from clarifying properties of topological insulators to me, Jörn has helped me quaff several Dresden bars dry of gin and tonic, locked me out of a hotel room in Warsaw, tolerated my heavily intoxicated self in Amsterdam (and everywhere else), joined me to extremely bad concerts in Boston, and so on and so forth. Frankly, I do not know how to reciprocate all this, but I look forward to figuring it out by trial and error.

Another important aspect of my PhD studies was following courses at TU Dresden. I am grateful to Matthias Vojta, Roland Ketzmerick and Arnd Bäcker, as well as their teaching assistants, for some of the most fascinating and constructive hours I have spent in a classroom, as well as for teaching me things that have become indispensable tools ever since.

Several other colleagues have contributed to my wellbeing. Alex Bogdanov was an extremely good-natured officemate and an excellent storyteller for more than three years. He also brought to my attention many interesting historical facts, as well as *"The Master and Margarita"* – one of the most captivating works of literature I have read. Steve Johnston, apart from sharing his knowledge in physics and coding, was the founder of Scotch Friday, a tradition that has flourished, making several scientists around the world, including myself, considerably jollier every Friday. Ulrike Nitzsche, apart from providing technical support on demand without fail, has had to clean up the mess after my poorly designed computation schemes went awfully wrong and endangered the integrity of the entire IFW computer cluster more times than I care to admit. I have had valuable discussions with Krzysztof Wohlfeld, Ioannis Rousochatzakis, Luuk Ament and Panagiotis Kotetes. Thomas Prestel showed me the ropes in and around Dresden. All the colleagues that contributed stories, witticisms and remarks during lunches or the aforementioned Friday evening activities made the work environment much more colorful.

At this point, I have to stress that my excursion into science is a direct consequence of the inexhaustible support from my grandparents and, most importantly, my mother. The latter, in particular, turned circumstances, which to outsiders may have seemed lacking, to a solid foundation for any endeavor I have ever embarked upon. This dissertation is dedicated to her.

Contents

Chapter 0

Background & motivation

The physics of the solid state showcases many fascinating phenomena that contradicted scientific intuition at the time of their discovery, and several that continue to do so today. Some of the most striking and unconventional properties of solids are manifestations of the underlying quantum nature of the constituent particles. A common reason for the unexpected behavior of experimental systems is the confinement of quantum particles in a submanifold of physical space. Structures in which the physics that dominates observations happens mainly in two dimensions, in particular, are hosts to a plethora of impressive phenomena. Some of them, e.g., high critical-temperature superconductivity, are already in use in technological applications today and are expected to be more widely employed in the near future. Relatedly, a large area of research on two-dimensional structures is predicated on ordering. On the theory side, this focus has led to the development of phenomenological and microscopic theories of ordered states and of the transitions into and out of them, whereas experimental progress is geared towards detecting the signatures of ordering.

Recently, the motivation behind a large body of experimental and theoretical work has been the notion of topological states of matter. Topological phases defy description in terms of traditional Ginzburg-Landau theories, have significantly enriched the band theory of solids and have materialized with the discovery of two- and three-dimensional topological insulators. The key features of these phases, which are descendants of the integer quantum Hall effect, can be captured by simple models of non-interacting electrons, while the repercussion of their realization has been a surge of imaginative ideas for applications. Technological innovation, however, which is one of the ultimate goals of condensed-matter research, requires increasingly more advanced engineering. As an example, the pursuit of quantum computation poses stringent requirements on candidate "computers" and has led to the fabrication of intricate structures in the nanoscale as testbeds. Promising prospects to find the ideal balance between functionality and complexity lie beyond non-interacting electrons, in the field of correlated systems. In this regime, competing tendencies of the constituent particles can lead to a plethora of quantum phases. The main goal in this arena is to realize correlated topological quantum states that are complex enough to facilitate desired functionality, while still being easy to engineer and manipulate.

At the basis of the remarkable discoveries in the field of topological insulation

lies a simple non-interacting toy model by Haldane, which describes electrons with frozen spin degree of freedom hopping on a two-dimensional honeycomb lattice. In the Haldane model, time-reversal symmetry is broken by a magnetic-flux pattern flowing through the unit cell and averaging out to zero in total. The energy spectrum consists of two bands, each of which is characterized by a topological invariant called the Chern number. This is nothing but the integer-quantized Hall conductivity of the system whenever one band is full. One of the most intriguing features of Haldane-like models is that they provide a launchpad for highly sought-after topologically ordered states, when interactions between particles are taken into account. Recent developments have demonstrated that, by doping such models and including short-range repulsion between particles, one obtains a novel class of topological states, dubbed fractional Chern insulators (FCI), which resemble in their properties the fractional quantum Hall (FQH) effect. This approach to the FQH regime deprecates the need for a strong magnetic field and is invaluable as a minimal framework for the investigation of interplay between correlations and topology in lattices, whereas proposed material-design schemes based on layered structures or interfaces promise room-temperature realizations.

The search for the optimal structure for the attainment and exploitation of topological phases raises fundamental questions, requiring proof-of-principle answers, on how these phases can be favored by material design: Are weak or strong interactions more favorable? Are insulators or semiconductors more suitable? Are itinerant or localized particles a better starting point? With these questions as a motivation, Part II of this dissertation will present a number of original perspectives on topological ordering in two-dimensional lattices. To this end, the archetypal FCI states will be subjected to strong interactions, in the presence of multiple bands, disorder or competing order, and their stability will be quantitatively assessed. Besides the tremendous implications of accessible topological states for the engineering of electronics, many unexpected opportunities for exceptional properties reside beyond the weakly correlated regime. These opportunities may prove instrumental in discovering complex states for future technological developments. Identifying and understanding **novel, strongly correlated, topological states of matter** with no weak-coupling counterparts is therefore crucial for progress in this field. A first example of such a quantum state that exhibits combined topological and Landau-type charge orders in a simple lattice model will also be presented in Part II.

In summary, this dissertation is aimed at exposing certain aspects of correlations in two-dimensional lattice models with topologically non-trivial content, which are expected to have impact on current and future experimental settings. After a presentation of the most pertinent theoretical facts governing topological states in Part I, the paradigm of FCIs will be employed to illustrate certain attributes of topological ordering, using a combination of numerically obtained intuition, symmetry arguments and phenomenological reasoning. In more detail, the text is organized as follows: Chapter 1 serves as an introduction to the quantum Hall regime, which is the origin of topological insulation. Defining principles of topological states, such as topological invariance, order and degeneracy, are elucidated, in anticipation of their usefulness later on. Chapter 2 introduces the quantum anomalous Hall effect and its derivatives, thus outlining the generalization of topological states to lattices, and highlights relevant physical systems. The topological invariant is redefined as an index categoriz-

ing the energy bands of a solid, with the help of the Haldane model. Part II then details how a single species of fermionic particles organize themselves into correlated topological states in two-dimensional lattices. After the introduction of two representative models in Chapter 3, the possible outcomes of including a short-range repulsion between particles are reviewed in order of increasing complexity, starting with the investigation of charge ordering in Chapter 4. Chapter 5 contains an extensive exposition of fractional Chern insulators and emphasizes their distinctive features. The next two Chapters venture into the realm of strong correlations and demonstrate how interactions can generate states that lie outside the usual classifications of topological phases. In Chapter 6, FCI states are shown to arise even when interactions are strong enough to mix bands with opposite Chern numbers. Finally, Chapter 7 documents the emergence of combined charge and topological order, leading to a new exotic quantum state with unprecedented observable signatures. Chapter 8 concludes the discussion of topological phases of spinless fermions in lattices and offers an outlook towards promising prospects.

Part I

Topological states of matter

Introduction

Topological phases constitute a relatively modern subfield of condensed-matter physics. The relevant notions emerged from the theory of Landau levels, which was formulated to explain the quantum Hall effects [1, 2], but have subsequently been expanded to describe phases occurring in other two- and three-dimensional structures. Research in topological states gained momentum after a number of theoretical predictions were evidenced in appropriate laboratory settings. Advances in this field have inspired scientists to envision technological applications, especially in the fields of device and energy engineering, while they have also led to novel perspectives on the perception of the solid state in general. Correlations, in conjunction with topology, have the potential to offer even more fascinating functionality, at the expense of increased complexity.

In Part I of this text, a number of concepts related to quantum Hall physics will be introduced somewhat thoroughly, because they are essential both to the understanding of topological matter in general and to the exposition of new results in Part II. The discussion will commence in Chapter 1 with a summary of basic facts concerning the integer and fractional quantum Hall effects – the first experimental manifestations of topological phases. Emphasis will be placed on explaining in what sense the origin of these effects is topology, as well as on a series of remarkable properties that set topologically non-trivial phases apart from all other states of matter. The discourse in Chapter 2 will be along the same lines, this time focusing on key features of topological states in lattice systems. Here, the connection between the theory of solids and algebraic topology will be made explicit and some nomenclature useful for following chapters will be put in place.

It should be stressed that seminal theoretical works related to the FQHE, such as the Laughlin wavefunction [3], composite fermions [4] and Chern-Simons field theories [5], will not be touched upon here, because a self-contained exposition would be unnecessarily lengthy for the purposes of this dissertation. The same holds for another defining property of quantum Hall systems, namely, their current-carrying edge states. It can be shown, on very general grounds, that quantum Hall effects are accompanied by the appearance of current-carrying states confined at the edges of a Hall bar [6–8]. These states have received considerable attention, both because they are relevant to the measurement of the Hall conductivity in real samples, but also because, due to the topological nature of the quantum Hall effects, they can carry current without any dissipation, regardless of the presence of disorder. Edge channels are, in fact, a common feature of topological states. Despite their importance and their potential to facilitate technological functionality, edge states will not be dealt with here, as all the discussion will be limited to systems defined in compact spaces.

Chapter 1

Quantum Hall effects

The quantum Hall effects are two of the most striking manifestations of quantum physics in the mesoscopic world. The integer quantum Hall effect (IQHE) was discovered in 1980, while measuring the conductivity of the two-dimensional electron gas (2DEG) forming in semiconductor microdevices at low temperatures and high magnetic fields [1]. The effect consists of a very precise quantization of the Hall conductivity, along with a vanishing longitudinal conductivity, over a range of the strength of a magnetic field applied perpendicular to the device plane, regardless of experimental details. A typical measurement outcome is shown in Figure 1.1(a). The discovery sparked a multitude of experimental and theoretical developments, which collectively led to a fundamentally new understanding of the solid state. The quantum-mechanical description of charged particles in a strong magnetic field, which will be briefly reviewed in Section 1.1, dictates that electrons organize themselves into Landau levels, shown schematically in Figure 1.1(b), each of which is perfectly flat in the bulk of the device. The pinnacle of theoretical progress was the identification of the quantized Hall conductivity as an invariant quantity, which represents the topology of the manifold the electrons reside in. Since topological invariance is a central concept of this work, the necessity for quantization of the Hall conductivity will be proven in Section 1.1.2.

Soon after the discovery of the IQHE, the microdevices used for experiments in the quantum Hall regime saw considerable improvements, especially in terms of impurity concentration. Surprisingly, new Hall plateaus were then discovered upon increasing the magnetic field strength beyond the value corresponding to a fully occupied lowest Landau level. This effect was named fractional quantum Hall effect (FQHE) and it has been an active field of research until today. In contrast to the integer case, interactions play a crucial role in this setting. The FQHE is therefore a many-body problem and its general solution has proven to be extremely challenging. Numerical calculations have been essential in gathering intuition as to the microscopics governing the effect. Some of the most basic properties of FQH states will be summarized in Section 1.2, since observing the analogies and contrasts to the results in Part II will be instrumental to understanding the novel aspects of the latter.

Even though the quantum Hall effects will primarily be of interest as a conceptual basis in what follows, they may also be of practical importance. The integer quantum Hall effect is already used to accurately define the SI unit of

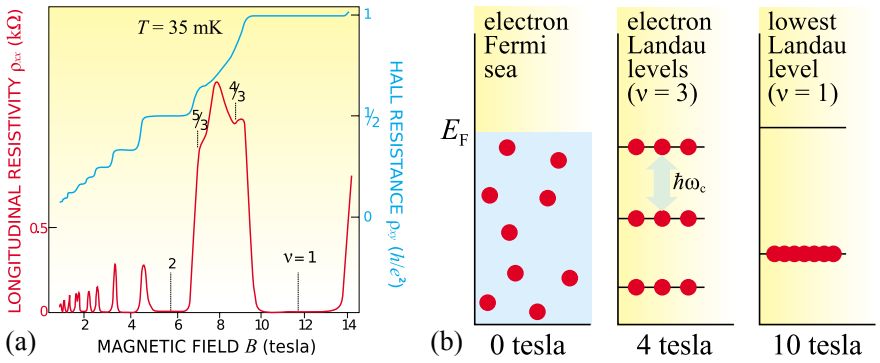

Figure 1.1: (a) Manifestation of the IQHE in resistivity measurements of the two-dimensional electron gas; Hall conductivity is equal in magnitude, but in inverse units, to transverse resistivity, here denoted by ρ_{xy}, whenever longitudinal resistivity vanishes. (b) Qualitative picture: electrons organize themselves into Landau levels, each of which contributes one quantum of conductivity whenever full. Reproduced with permission from: J. Jain, *"The Composite Fermion: A Quantum Particle and its Quantum Fluids"*, Physics Today, volume **53** (April 2000), page 39 [11]; Copyright © 2000, American Institute of Physics.

electrical resistance and can also be employed in more precise and reproducible definitions of mechanical units, such as the kilogram, which are otherwise hard to maintain [9]. On the other hand, the quantum Hall effects have also attracted the attention of high-energy physicists, as they provide a testbed of the AdS/CFT duality [10]. It is probably safe to say that the quantum Hall effects have been two of the most stimulating scientific discoveries of the 20th century.

1.1 Integer quantum Hall effect

1.1.1 Landau levels

Consider a single electron confined in a plane, subject to a perpendicular magnetic field $\boldsymbol{B} = B\boldsymbol{e}_3$, where $\boldsymbol{e}_i$ with $i = 1, 2, 3$ are unit vectors that form an orthogonal right-handed set. It is assumed that B is large enough to fully polarize the spins of all electrons. The vector potential in the symmetric gauge is $\boldsymbol{A}(\boldsymbol{r}) = (\boldsymbol{B} \times \boldsymbol{r})/2$, with the position operator expressed as the vector $\boldsymbol{r} = r_1\boldsymbol{e}_1 + r_2\boldsymbol{e}_2$. From now on, all vectors will be in the (r_1, r_2)-plane, unless explicitly defined otherwise. The magnetic field is $\boldsymbol{B} = \nabla \times \boldsymbol{A}$. The Hamiltonian describing the electron is [12]

$$h_{\mathrm{LL}} = \frac{1}{2m}\left[\boldsymbol{p} - \frac{e}{c}\boldsymbol{A}(\boldsymbol{r})\right]^2 = \frac{\boldsymbol{\pi}^2}{2m}\,, \tag{1.1}$$

where m and $-e$ are the electron effective mass and charge, respectively, and c is the speed of light in vacuum. The operator-valued components of the momentum vector $\boldsymbol{p}$ are defined as $p_j = \frac{\hbar}{\mathrm{i}}\partial_j$ with $j = 1, 2, 3$, where ∂_j denotes the partial derivative along the direction of $\boldsymbol{e}_j$, and i is the imaginary unit. The

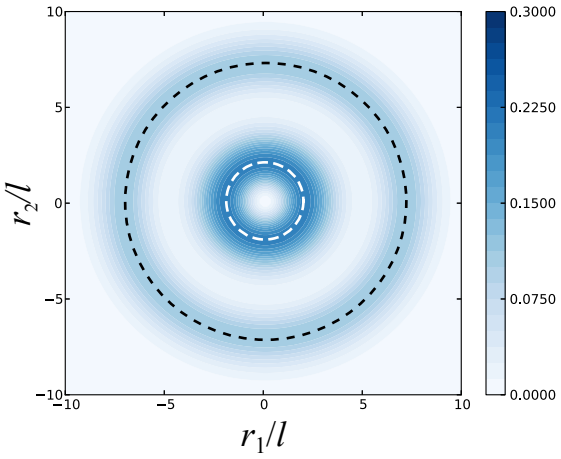

Figure 1.2: Contour plot of the sum $|\psi_{0,2}| + |\psi_{0,20}|$ in the r_1-r_2 plane. The dashed lines trace the maxima of $|\psi_{0,2}|$ and $|\psi_{0,20}|$ with radii $r_{0,2} = 2l$ (white) and $r_{0,20} = \sqrt{40}l$ (black).

components of position and momentum operators obey the canonical commutation relations $[r_i, p_j] = \mathrm{i}\hbar\delta_{ij}$, where $\hbar = h/(2\pi)$ and h is Planck's constant. Equation (1.1) has also introduced the dynamical momenta as

$$\pi_1 := p_1 + \frac{eB}{2c} r_2 \,, \quad \pi_2 := p_2 - \frac{eB}{2c} r_1 \,. \tag{1.2}$$

These obey the commutation relation $[\pi_1, \pi_2] = \mathrm{i}e\hbar B/c$. In second-quantization formalism, h_{LL} can be represented by the ladder operators

$$\hat{a} = \sqrt{\frac{c}{2\hbar eB}}(\pi_1 - \mathrm{i}\pi_2) \,, \quad \hat{a}^\dagger = \sqrt{\frac{c}{2\hbar eB}}(\pi_1 + \mathrm{i}\pi_2) \,, \tag{1.3}$$

which obey the commutation relation $[\hat{a}, \hat{a}^\dagger] = 1$, as

$$\hat{h}_{\mathrm{LL}} = \hbar\omega \left(\hat{a}^\dagger \hat{a} + \frac{1}{2} \right) \,, \tag{1.4}$$

where the cyclotron frequency has been defined as $\omega := eB/(mc)$. The energy spectrum is therefore

$$E_n = \hbar\omega \left(n + \frac{1}{2} \right) \,, \tag{1.5}$$

with $n \geq 0$. The energy branches are called Landau levels and they are manifestly independent of the electron momentum. A cartoon picture of Landau quantization can be seen in Figure 1.1(b).

It is readily seen that the ansatz wavefunction

$$\psi_{n,m}(z, \bar{z}) = \left[\frac{n!}{2\pi l^2 (n+m)!} \right]^{1/2} \left(\frac{z}{\sqrt{2}l} \right)^m \exp\left(-\frac{z\bar{z}}{4l^2} \right) \,, \tag{1.6}$$

where $l := \sqrt{\hbar c/(eB)}$, $z = r_1 - \mathrm{i}r_2$ and $\bar{z}$ its conjugate, is a normalized eigenfunction of h_{LL} with eigenvalue E_n. The states described by $\psi_{n,m}$ are called Landau

orbitals, because m can be seen as an angular-momentum quantum number. In fact, each $\psi_{n,m}$ can be visualized as a circular shell, with its modulus peaked at a radius $r_{n,m} = \sqrt{2ml}$, as illustrated in Figure 1.2. The general lowest Landau-level eigenfunction will be a polynomial of fixed degree m_0, multiplied by a Gaussian factor. It can therefore be expressed as

$$\Psi_0(z,\bar{z}) = C_{m_0} \prod_{i=1}^{m_0} (z - Z_i) \exp\left(-\frac{z\bar{z}}{4l^2}\right) , \tag{1.7}$$

where Z_i are the locations of the zeros of the polynomial factor and C_{m_0} a normalization constant.

1.1.2 Quantization of Hall conductivity

Laughlin's Gedankenexperiment

A simple, yet powerful, qualitative argument that makes the quantization of the Hall conductivity in the IQHE explicit was put forward by Laughlin [13]. Consider an electron confined in an annulus, with a magnetic field applied perpendicular to the plane, as in the previous section. This is the so-called Corbino-disk geometry. Consider also an additional magnetic flux Φ directed through the hole of the disk, without penetrating the annular region. The new Hamiltonian h'_{LL} describing the single electron will then read

$$h'_{\mathrm{LL}} = \frac{1}{2m}\left(\boldsymbol{p} - \frac{e}{c}\boldsymbol{A} - \frac{e}{c}\boldsymbol{A}_\Phi\right)^2 = \frac{\boldsymbol{\pi}'^2}{2m} , \tag{1.8}$$

where the vector potential that generates Φ has been defined as $\boldsymbol{A}_\Phi = \boldsymbol{e}_\theta \Phi/(2\pi r)$, with $\boldsymbol{e}_\theta$ is unit vector in the azimuthal direction and r the radial coordinate. This setting is depicted in Figure 1.3(a). The point of the argument is to evaluate the current induced by an adiabatic variation of Φ from zero to one flux quantum $\Phi_0 \equiv hc/e$. Since the Landau-level wavefunctions of Equation (1.7) extend around the Corbino disk, it is clear that they encircle the flux through the hole and a non-zero Aharonov-Bohm current is hence expected. The current operator is simply $\boldsymbol{j} := e\boldsymbol{\pi}'/m$, where $\boldsymbol{\pi}'$ is the dynamical-momentum vector defined above. It is readily seen that the current is given by the functional derivative of the Hamiltonian with respect to $\boldsymbol{A}_\Phi$, namely, $\boldsymbol{j} = \delta h'_{\mathrm{LL}}/\delta \boldsymbol{A}_\Phi$. Assuming that $|\Psi\rangle$ is the instantaneous normalized ground state of h'_{LL} and E is its corresponding eigenvalue, the expectation value of the current operator at zero temperature will be $\langle \boldsymbol{j} \rangle = \langle \Psi | \delta h'_{\mathrm{LL}}/\delta \boldsymbol{A}_\Phi | \Psi \rangle = \delta E/\delta \boldsymbol{A}_\Phi$. Using the rules of functional derivatives, one can write consecutively

$$\partial_\Phi E = \int_\Omega d\Omega \, \frac{\delta E}{\delta \boldsymbol{A}_\Phi} \cdot \partial_\Phi \boldsymbol{A}_\Phi = \int_\Omega d\Omega \, \frac{\langle \boldsymbol{j} \rangle \cdot \boldsymbol{e}_\theta}{2\pi r} = I , \tag{1.9}$$

where Ω is the area of the annulus and I is the total induced current flowing around the disk. Now Φ is changed adiabatically from 0 to Φ_0. For $\Phi = \Phi_0$, the contribution $\boldsymbol{A}_\Phi$ can be gauged away, since the corresponding phase shift to a wavefunction extending around the annulus is $\frac{e}{\hbar}\int_P \boldsymbol{A}_{\Phi_0} \cdot d\boldsymbol{l} = 2\pi$, for any closed trajectory P encircling the hole. This means that the energy spectrum of h_{LL} must be identical before and after the cycle. Note, however, that this is

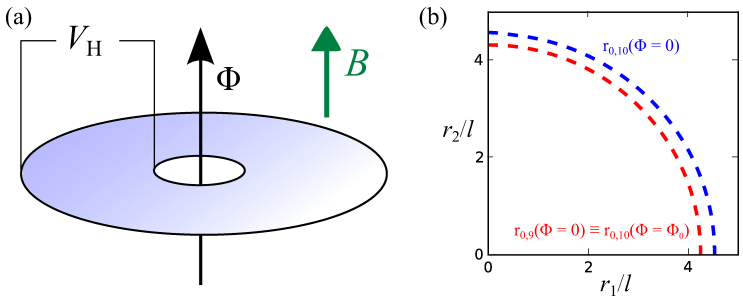

Figure 1.3: (a) Annular geometry for Laughlin's Gedankenexperiment and (b) maxima of $|\psi_{0,10}|$ and $|\psi_{0,9}|$ with radii $r_{0,10} = \sqrt{20}l$ (red) and $r_{0,9}(\Phi = 0) \equiv r_{0,10}(\Phi = \Phi_0) = \sqrt{18}l$ (blue). Insertion of one flux quantum maps $\psi_{0,10}$ to $\psi_{0,9}$.

not the case for all values of Φ: only integer multiples of Φ_0 can be seen purely as a gauge transformation, as all other values do not respect the periodicity in the azimuthal direction.

The effect of inserting flux through the hole of the disk can be deduced directly from the transformed vector potential. In Cartesian coordinates, this is

$$\boldsymbol{A}' = \boldsymbol{A} + \boldsymbol{A}_\Phi = \frac{B}{2}\left(-r_2\left(1 + \frac{\Phi}{\pi r^2 B}\right), r_1\left(1 + \frac{\Phi}{\pi r^2 B}\right)\right), \tag{1.10}$$

where $r = \sqrt{r_1^2 + r_2^2}$. The insertion of flux is therefore equivalent to a generalized coordinate transformation, which leads to a shrinkage of the eigenfunctions. The net effect of the flux insertion is therefore an inward movement of charge density. Insertion of exactly one flux quantum maps $\psi_{0,m}$ to $\psi_{0,m-1}$ [see Figure 1.3(b) for an example]. When all Landau orbitals in the lowest Landau level are full, this corresponds to a net transfer of precisely one electron from the outer to the inner edge of the annulus. Gauge invariance guarantees that the energy after inserting a flux quantum is the same as with no flux. The energy change ΔE is therefore solely the change of the electrostatic potential caused by moving one charge from outer to inner edge, and is equal to eV_H, where V_H is the measured Hall voltage. The current can then be written as

$$I = c\partial_\Phi E = c\frac{\Delta E}{\Phi_0} = \frac{e^2}{h}V_H\,. \tag{1.11}$$

The quantization of the Hall conductivity has thus been derived. The power of this argument lies in its generality. The expectation value $\langle \boldsymbol{j} \rangle$ can be taken at finite temperatures. The argument is also robust against impurities and interactions, as long as there are extended states that encircle the flux, and its validity also encompasses fractionally filled Landau levels. Finally, it should be noted that, even though it may seem like gauge selection affects the properties of the quantum Hall liquid, this is actually not the case. Similar considerations hold for every other gauge, even though the symmetries of the lowest Landau-level eigenfunctions are different[1].

[1]The original argument by Laughlin, for example, was made using the Landau gauge [13].

Hall conductivity as a topological invariant

An alternative modeling of electrons in a strong magnetic field is apt for a more formal identification of the Hall conductivity as an invariant and quantized quantity that characterizes Landau levels. The Corbino disk of Figure 1.3(a) is deformed, so that the inner and outer edges are connected. The resulting manifold is a torus. The system can then be seen as the area $[0, L_1) \times [0, L_2)$ with periodic boundary conditions, where L_1 and L_2 are the extents along directions $\boldsymbol{e}_1$ and $\boldsymbol{e}_2$, respectively. The magnetic field is still assumed to be uniform and perpendicular to the toroidal surface everywhere. The vector potential must correspondingly be linearly dependent on the coordinates of the position vector $\boldsymbol{r}$. On the other hand, translation symmetry dictates that the Hamiltonian h_{LL} should be unchanged after the shift $\boldsymbol{r} \to \boldsymbol{r} + \boldsymbol{R}$, where $\boldsymbol{R}$ is an arbitrary vector. However, the typical translation operators, defined as $T(\boldsymbol{R}) := \exp[(i/\hbar)\boldsymbol{R} \cdot \boldsymbol{p}]$, do not commute with the Hamiltonian. In order to restore the translational symmetry, one has to define the so-called magnetic translation operators [14, 15]

$$\tilde{T}(\boldsymbol{R}) := e^{\frac{\mathrm{i}}{\hbar}\boldsymbol{R}\cdot\boldsymbol{\pi}}\,, \tag{1.12}$$

where $\boldsymbol{\pi}$ is the dynamical-momentum vector. The magnetic translation operators corresponding to two arbitrary translations $\boldsymbol{R}_a$ and $\boldsymbol{R}_b$, with $\boldsymbol{R}_a \neq \boldsymbol{R}_b$, commute with the Hamiltonian, but generally do not commute with each other. Indeed,

$$\begin{aligned}\tilde{T}(\boldsymbol{R}_a)\tilde{T}(\boldsymbol{R}_b) &= \tilde{T}(\boldsymbol{R}_b)\tilde{T}(\boldsymbol{R}_a)\exp\left[-\frac{2\pi\mathrm{i}}{l^2}(\boldsymbol{R}_a \times \boldsymbol{R}_b)\cdot\boldsymbol{e}_3\right] \\ &= \tilde{T}(\boldsymbol{R}_b)\tilde{T}(\boldsymbol{R}_a)\exp\left(-2\pi\mathrm{i}\frac{\Phi}{\Phi_0}\right)\,. \end{aligned} \tag{1.13}$$

The commutator is zero only if the magnetic flux $\Phi := B(\boldsymbol{R}_a \times \boldsymbol{R}_b)\cdot\boldsymbol{e}_3$ is an integer multiple of Φ_0. Furthermore, one may express translation vectors in units of $l := \sqrt{hc/(eB)}$, the magnetic length. Translations by $(l + R_1)\boldsymbol{e}_1$ and $(l + R_2)\boldsymbol{e}_2$ are then equivalent to translations $R_1\boldsymbol{e}_1$ and $R_2\boldsymbol{e}_2$. Consequently, the magnetic field generates a Bravais lattice with lattice constant l.

Due to the fact that they commute, the operators $T_{\boldsymbol{R}}$ and the Hamiltonian have common eigenfunctions, in analogy to Bloch electrons. The eigenvalue equations for the eigenfunctions $\psi^\beta_{\boldsymbol{\kappa}}$ for the magnetic translation operators are, in full analogy to Bloch theory,

$$\tilde{T}(a\boldsymbol{e}_1)\psi^\beta_{\boldsymbol{\kappa}} = e^{\mathrm{i}\kappa_1 a}\psi^\beta_{\boldsymbol{\kappa}} \tag{1.14a}$$

$$\tilde{T}(b\boldsymbol{e}_2)\psi^\beta_{\boldsymbol{\kappa}} = e^{\mathrm{i}\kappa_2 b}\psi^\beta_{\boldsymbol{\kappa}}\,, \tag{1.14b}$$

where κ_i for $i = 1, 2$ are the components of the magnetic crystal momentum $\boldsymbol{\kappa}$, defined in the magnetic Brillouin zone $[0, 2\pi/L_1) \times [0, 2\pi/L_2)$, and $\beta \geq 0$ is a band index. The eigenfunctions can be written in Bloch form as

$$\psi^\beta_{\boldsymbol{\kappa}}(\boldsymbol{r}) = e^{\mathrm{i}\boldsymbol{\kappa}\cdot\boldsymbol{r}}u^\beta_{\boldsymbol{\kappa}}(\boldsymbol{r})\,, \tag{1.15}$$

where $u_{\boldsymbol{\kappa}}(\boldsymbol{r})$ obey the generalized Bloch conditions

$$u^\beta_{\boldsymbol{\kappa}}(r_1 + al, r_2) = e^{-\mathrm{i}\pi r_2/l}u^\beta_{\boldsymbol{\kappa}}(\boldsymbol{r}) \tag{1.16a}$$

$$u^\beta_{\boldsymbol{\kappa}}(r_1, r_2 + bl) = e^{\mathrm{i}\pi r_1/l}u^\beta_{\boldsymbol{\kappa}}(\boldsymbol{r})\,. \tag{1.16b}$$

The eigenfunctions $\psi^{\beta}_{\boldsymbol{\kappa}}$ form the Hilbert space of Landau orbitals on the torus, with each β corresponding to a Landau level. The degeneracy of each level is $N_\Phi := L_1 L_2/l^2$, which is the total flux piercing the surface of the torus, in units of Φ_0.

It is now assumed that the number of electrons N is equal to N_Φ, so that only the lowest Landau level is full. The many-body Hamiltonian is written as

$$\mathcal{H}_{\mathrm{LL}} = \frac{1}{2m}\sum_i^N \left[\boldsymbol{p}_i - \frac{e}{c}\boldsymbol{A}(\boldsymbol{r}_i)\right]^2 = \sum_i^N \frac{\boldsymbol{\pi}_i^2}{2m}\,, \tag{1.17}$$

where $\boldsymbol{r}_i$, $\boldsymbol{p}_i$ and $\boldsymbol{\pi}_i$ are the position, momentum and dynamical momentum operators, respectively, corresponding to the ith particle. At zero temperature, the electronic system will be in a single many-body ground state $|\Psi_0\rangle$ with eigenvalue E_0. For the calculation of the Hall conductivity, one may use the Kubo formula [16, 17]

$$\sigma = \frac{ie^2\hbar}{L_1 L_2}\sum_{j>0}\frac{\langle\Psi_0|U_1|\Psi_j\rangle\langle\Psi_j|U_2|\Psi_0\rangle - \langle\Psi_0|U_2|\Psi_j\rangle\langle\Psi_j|U_1|\Psi_0\rangle}{(E_j-E_0)^2}\,, \tag{1.18}$$

where $|\Psi_j\rangle$ represent many-body excited states with eigenvalues E_j. The components U_1 and U_2 of the velocity operator are given by $\boldsymbol{U} = \sum_i^N \boldsymbol{\pi}_i/m$. After the unitary transformation

$$W_j(\boldsymbol{r}_1,\ldots,\boldsymbol{r}_N) = e^{-\mathrm{i}\boldsymbol{\kappa}\cdot(\boldsymbol{r}_1+\cdots+\boldsymbol{r}_N)}\Psi_j(\boldsymbol{r}_1,\ldots,\boldsymbol{r}_N)\,, \tag{1.19}$$

the Hall conductivity can be written as

$$\sigma = \frac{2e^2}{L_1 L_2\hbar}\mathrm{Im}\sum_{j>0}\frac{\langle W_0|\partial_{\kappa_1}\tilde{\mathcal{H}}_{\mathrm{LL}}|W_j\rangle\langle W_j|\partial_{\kappa_2}\tilde{\mathcal{H}}_{\mathrm{LL}}|W_0\rangle}{(E_j-E_0)^2}\,, \tag{1.20}$$

where $\tilde{\mathcal{H}}_{\mathrm{LL}}$ is obtained from $\mathcal{H}_{\mathrm{LL}}$ by performing the shift $\boldsymbol{p}_i \to \boldsymbol{p}_i + \hbar\boldsymbol{\kappa}$ with $i = 1,\ldots,N$, and state $|W_j\rangle$ corresponds to wavefunction W_j. Using the identity

$$\left\langle W_j\left|\partial_{\kappa_i}\tilde{\mathcal{H}}_{\mathrm{LL}}\right|W_0\right\rangle = (E_0-E_j)\left\langle W_j\left|\partial_{\kappa_i}W_0\right.\right\rangle\,, \tag{1.21}$$

which holds for all the off-diagonal matrix elements encountered here, along with the completeness of the Hilbert space, one ends up with the following relation for the Hall conductivity:

$$\sigma = \frac{2e^2}{\hbar}\mathrm{Im}\,\langle\partial_{\varphi_1}W_0|\partial_{\varphi_2}W_0\rangle\,, \tag{1.22}$$

where $\varphi_i = \kappa_i L_i$ for $i = 1, 2$.

At this point, some physical arguments are useful in order to identify σ as a topological invariant. From Equation (1.20) it becomes clear that the ground state must be gapped, if the Hall conductivity is to remain finite. Experiments corroborate the bulk insulating nature of the ground state, as can be seen in the behavior of the longitudinal conductivity in Figure 1.1. Moreover, the Hall conductivity should not depend on the values of the angles φ_1 and φ_2. That is because one can equivalently view these angles as the definition of generalized

periodic boundary conditions. Since the boundaries cannot affect bulk properties in the thermodynamic limit, the Hall conductivity cannot depend on φ_1 or φ_2[2]. Finally, when the ground state is gapped and non-degenerate, changing the angles φ_1 or φ_2 by 2π necessarily leads to a state that differs from the ground state by at most a phase factor, as one can see by following the argumentation of Laughlin's Gedankenexperiment.

The above arguments can be cast into mathematical form. The latter implies that one can write

$$|W_0(2\pi, \varphi_2)\rangle = e^{\mathrm{i}\lambda(\varphi_2)} |W_0(0, \varphi_2)\rangle \tag{1.23a}$$

$$|W_0(\varphi_1, 2\pi)\rangle = e^{\mathrm{i}\xi(\varphi_1)} |W_0(\varphi_1, 0)\rangle \ . \tag{1.23b}$$

It is thus seen that

$$|W_0(2\pi, 2\pi)\rangle = e^{\mathrm{i}[\lambda(0)+\xi(2\pi)]} |W_0(0,0)\rangle = e^{\mathrm{i}[\lambda(2\pi)+\xi(0)]} |W_0(0,0)\rangle \tag{1.24}$$

and therefore

$$\lambda(2\pi) - \lambda(0) - \xi(2\pi) + \xi(0) = 2\pi p \,, \tag{1.25}$$

where p is an integer. Also, since the Hall conductivity has to be independent of φ_1 and φ_2, one can freely average over all values, obtaining

$$\sigma = \frac{e^2}{\pi h} \mathrm{Im} \iint_0^{2\pi} d\varphi_1 d\varphi_2 \ \langle \partial_{\varphi_1} W_0 | \partial_{\varphi_2} W_0 \rangle \ . \tag{1.26}$$

Calculation of the integrals in Equation (1.26) yields

$$\sigma = \frac{e^2}{2\pi h} [\lambda(2\pi) - \lambda(0) - \mu(2\pi) + \mu(0)] = \frac{e^2}{h} p \,, \tag{1.27}$$

where the relation

$$\left\langle \partial_{\varphi_1} W_0 \middle| \partial_{\varphi_2} W_0 \right\rangle = \partial_{\varphi_1} \left\langle W_0 \middle| \partial_{\varphi_2} \middle| W_0 \right\rangle - \left\langle W_0 \middle| \partial^2_{\varphi_1 \varphi_2} \middle| W_0 \right\rangle \tag{1.28}$$

has been used in the evaluation. The integer p, which is assigned to the ground state of the full lowest Landau level, is known in the field of topology as the first Chern number, and in condensed-matter physics as the Thouless-Kohmoto-Nightingale-den Nijs (TKNN) index. Experiments show, with remarkable precision, that, for a single completely filled Landau level, $p = 1$ (see Figure 1.1).

The above discussion may seem limited to a perfect system without impurities. Note, however, that the procedure that leads to the quantization of the Hall conductivity does not depend on translational invariance. In fact, the unitary transformation of Equation (1.19) and the generalized boundary conditions of Equations (1.23) are valid, even if translational symmetry is broken by a disorder potential. As long as the disorder does not close the energy gap over the ground state of the full Landau level, then the calculation proceeds in precisely the same way. It is actually this invariance under disorder that makes the observation of the Hall plateaus possible. At magnetic field values corresponding to a slightly doped lowest Landau level, the argumentation of this Section would normally break down. It can be seen, however, that the extra states that appear

[2] This qualitative argument can also be based on firmer mathematical ground; see Ref. [17].

due to doping are pinned by impurities and therefore do not conduct, whereas the remaining extended states contribute the entire Hall conductivity [18, 19].

The quantization of the Hall conductivity in the IQHE is therefore unaffected by disorder, interactions, finite-temperature effects, and generally any perturbation that does not close the gap above the lowest Landau level, and is also independent of the size and geometry of the studied system. It is clear, however, that the derivation of the quantization relies on the generalized boundary conditions of Equations (1.23). The latter are tied to the toroidal topology of the system and the proof of quantization that was illustrated here would not be possible if the manifold is changed to a non-compact one. Additionally, the integer p changes upon changing the genus of the torus [20]. It is precisely this property of σ that renders it a topological invariant.

The process highlighted in the preceding paragraphs establishes that the Hall conductivity of the 2DEG in a strong magnetic field is quantized. The implications of the above derivation are, however, more profound. The magnetic crystal momenta introduced above originated from an emergent Bravais lattice generated by the magnetic field. The entire quantization argument remains intact even if one replaces the magnetic crystal momenta with actual crystal momenta corresponding to the Bravais lattice of a real crystal structure [21]. This realization had an enormous repercussion on the understanding of the very nature of the solid state, as described by band theory (see Chapter 2).

The Hall conductivity can be recast into a form that will help establish a correspondence to quantum-Hall physics in Section 2.1. In a non-interacting system without impurities, W_0 will be a Slater determinant of the single-particle Bloch functions $u^0_{\boldsymbol{\kappa}}$. Equation (1.26) can hence be written equivalently [22]

$$\sigma = \frac{e^2}{\pi h}\mathrm{Im}\iint_0^{2\pi} d\kappa_1 d\kappa_2 \, \langle \partial_{\kappa_1} u^0_{\boldsymbol{\kappa}} | \partial_{\kappa_2} u^0_{\boldsymbol{\kappa}} \rangle \ . \tag{1.29}$$

This can be rewritten as

$$\sigma = \frac{e^2}{2\pi h}\iint_0^{2\pi} d\kappa_1 d\kappa_2 \, \boldsymbol{e}_3 \cdot \boldsymbol{\Omega}(\kappa_1, \kappa_2) \,, \tag{1.30a}$$

with

$$\boldsymbol{\Omega}(\kappa_1, \kappa_2) := \mathrm{i}\nabla_{\boldsymbol{\kappa}} \times \boldsymbol{A}_0 \tag{1.30b}$$

and

$$\boldsymbol{A}_0 := \langle u^0_{\boldsymbol{\kappa}} | \nabla_{\boldsymbol{\kappa}} | u^0_{\boldsymbol{\kappa}} \rangle \ , \tag{1.30c}$$

where $\nabla_{\boldsymbol{\kappa}}$ denotes the nabla operator in the $\boldsymbol{\kappa}$-plane. Is is seen that $\boldsymbol{A}_0$ has the form of a vector potential in $\boldsymbol{\kappa}$-space and, consequently, $\boldsymbol{\Omega}$ corresponds to a fictitious magnetic field. The quantities $\boldsymbol{A}_0$ and $\boldsymbol{\Omega}$, called Berry connection and Berry curvature, respectively, will be encountered again in Section 2.1.

1.2 Fractional quantum Hall effect

1.2.1 Ground-state degeneracy & Hall conductivity

Despite the fact that the treatment of a fractionally filled Landau level in the presence of interactions is considerably more complicated than what was presented in Section 1.1, important conclusions can be reached by general physical

considerations. As already mentioned above, the Laughlin argument can be generalized to include interactions between particles [23]. According to this argument, whenever the ground state in a gapped quantum Hall system is unique, insertion of one flux quantum leads necessarily to back to the same state and induces an integer quantized Hall conductivity. A Landau level that is partially filled by non-interacting particles will have a massive degeneracy in the ground state and many zero-energy excitations. To conform with the experimental finding of vanishing longitudinal conductivity, shown in Figure 1.4, this degeneracy must be lifted by interactions and a gapped ground state should emerge. If, however, this ground state is unique, then Laughlin's argument guarantees that the Hall conductivity will be integer-quantized, contrary to what is observed in experiments.

The only way to reconcile a fractional value for the Hall conductivity with Laughlin's argument is to assume that the ground state is degenerate [23]. This would mean that insertion of one flux quantum would not lead back to exactly the same state, but to a different one within the degenerate ground-state manifold. The insertion of more than one flux quanta will then be required in order to return to the same state, with one particle transfered from one edge of the sample to the other. The Hall conductivity after one adiabatic cycle will assume an integer value, divided by the number of cycles required to pump one particle from edge to edge. At a fractional filling $\nu = 1/q$ with q an odd integer, the number of cycles will be q on average, since only 1 out q Landau orbitals will be occupied. Furthermore, individual states in the ground-state manifold will only be perfectly degenerate in a thermodynamically large system. In finite systems, the degeneracy will be approximate and there will be gaps between the energy levels corresponding to quasi-degenerate ground states. The values of these energy levels will change as a function of flux, and they are expected to exchange places at integer multiples of Φ_0. This is an important characteristic of FQH energy spectra and it will be utilized in Part II.

The above somewhat hand-waving arguments can be solidified by a symmetry analysis. Considering the same geometry as in Section 1.1.2, the Hamiltonian for N interacting electrons reads

$$\mathcal{H}_N = \frac{1}{2m}\sum_{j=1}^{N}\left[\boldsymbol{p}_j - \frac{e}{c}\boldsymbol{A}(\boldsymbol{r}_j)\right]^2 + \frac{1}{2}\sum_{i\neq j} V(\boldsymbol{r}_i - \boldsymbol{r}_j)\,, \tag{1.31}$$

where V represents the potential energy arising due to the Coulomb repulsion between particles i and j at positions $\boldsymbol{r}_i$ and $\boldsymbol{r}_j$, respectively. The eigenfunctions $\psi(\boldsymbol{r}_1, \boldsymbol{r}_2, \ldots, \boldsymbol{r}_N)$ of this Hamiltonian are generally unknown. However, the single-particle magnetic translation operators defined in Eq. (1.14) can be used to define the many-body translation operators

$$\mathcal{T}(\boldsymbol{R}) := \prod_{j=1}^{N} T_j(\boldsymbol{R})\,. \tag{1.32}$$

These operators translate the many-body wavefunction Ψ by a vector $\mathbf{R}$.

In the previous section, it was shown that the number of single-particle states N_Φ in a Landau level is given by the total magnetic flux penetrating the system, which is equal to $L_1 L_2 eB/(hc)$. In the FQHE regime, the number of

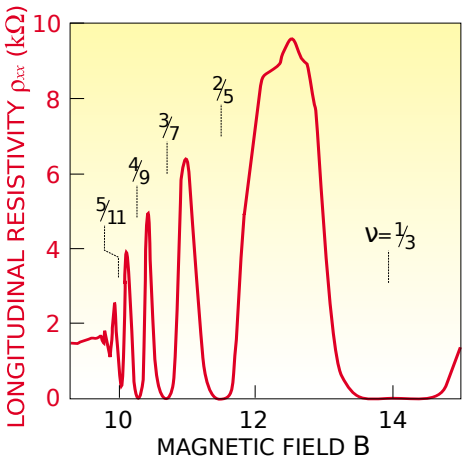

Figure 1.4: Experimental observation of vanishing longitudinal resistivity, and, equivalently, longitudinal conductivity, in the fractional quantum Hall effect. Reproduced with permission from: J. Jain, *"The Composite Fermion: A Quantum Particle and its Quantum Fluids"*, Physics Today, volume **53** (April 2000), page 39 [11]; Copyright © 2000, American Institute of Physics.

electrons is a rational fraction of the available states, defined as $N = (p/q)N_\Phi$. The boundary conditions

$$T_j(L_1\boldsymbol{e}_1)\Psi = \Psi\,, \tag{1.33a}$$
$$T_j(L_2\boldsymbol{e}_2)\Psi = \Psi\,, \tag{1.33b}$$

which are the same as Equations (1.14) for $a = L_1$ and $b = L_2$, are satisfied by the operators $\mathcal{T}(L_1\boldsymbol{e}_1/N_\Phi)$ and $\mathcal{T}(L_2\boldsymbol{e}_2/N_\Phi)$. These operators commute with the Hamiltonian. Suppose that $|\Psi_{0,0}\rangle$ is a ground state of the Hamiltonian and, simultaneously, an eigenfunction of the operator $\mathcal{T}(L_2\boldsymbol{e}_2/N_\Phi)$. The operators $\mathcal{T}(L_1\boldsymbol{e}_2/N_\Phi)$ and $\mathcal{T}(L_2\boldsymbol{e}_2/N_\Phi)$ do not commute with each other:

$$\mathcal{T}(L_1\boldsymbol{e}_1/N_\Phi)\mathcal{T}(L_2\boldsymbol{e}_2/N_\Phi) = \mathcal{T}(L_2\boldsymbol{e}_2/N_\Phi)\mathcal{T}(L_1\boldsymbol{e}_1/N_\Phi)e^{-2\pi ip/q}\,. \tag{1.34}$$

The ground state must therefore be q-fold degenerate, since the eigenfunctions

$$|\Psi_{0,n}\rangle := [\mathcal{T}(L_1\boldsymbol{e}_1/N_\Phi)]^n\,|\Psi_{0,0}\rangle\,, \tag{1.35}$$

with $n = 1, \ldots, q-1$, are also ground states. This degeneracy depends on the boundary conditions and the genus (i.e., the topology) of the two-dimensional manifold the particles move in, but not on its size or aspect ratio (i.e., the geometry). For this reason, it is called topological degeneracy [20].

The necessity for degeneracy in the ground state can also be deduced from the Hall conductivity. The discussion in Section 1.1.2 implies that the Hall conductivity can only be an integer multiple of e^2/h whenever there is a single gapped ground state. This immediately suggests that, in order to have a fractionally quantized Hall conductivity, the ground state must be degenerate. The Hall conductivity should hence be the average of the values obtained by

applying the Kubo formula to each of the states in the ground-state manifold, i.e., [17]

$$\sigma = \frac{e^2}{2\pi i\hbar q}\sum_{i=1}^{q}\iint_0^{2\pi} d\varphi_1 d\varphi_2 \left[\left\langle \partial_{\varphi_1}\Psi_{0,i}\middle|\partial_{\varphi_2}\Psi_{0,i}\right\rangle - \left\langle \partial_{\varphi_2}\Psi_{0,i}\middle|\partial_{\varphi_1}\Psi_{0,i}\right\rangle\right], \tag{1.36}$$

where q is the degeneracy and the summation is over degenerate ground states $|\Psi_{0,j}\rangle$. Another useful form for the Hall conductivity can be obtained by similarly generalizing the form given in Equation (1.20) to the many-body case, by writing

$$\sigma = \frac{2e^2 L_1 L_2}{\hbar q}\sum_{i=1}^{q}\iint_0^{2\pi} d\varphi_1 d\varphi_2 \,\mathrm{Im}\sum_{j>0}\frac{\langle\Psi_{0,i}|\partial_{\varphi_1}\tilde{\mathcal{H}}_N|\Psi_j\rangle\langle\Psi_j|\partial_{\varphi_2}\tilde{\mathcal{H}}_N|\Psi_{0,i}\rangle}{(E_j - E_0)^2}, \tag{1.37}$$

where $|\Psi_j\rangle$ denotes the jth excited state and $\tilde{\mathcal{H}}_N$ is $\mathcal{H}_N$ after the insertion of fluxes κ_1 and κ_2, in full analogy with the procedure outlined in Section 1.1.2. In a definition parallel to the one in Equations (1.30), the integrand in Equation (1.37) for each of the degenerate ground states is the many-body Berry curvature and will be used extensively to identify correlated topological states in Part II.

1.2.2 Fractional quasiparticle statistics

One of the most impressive predictions in the theory of the FQHE is the emergence of quasiparticles with fractional charge e/q, where q is the odd integer denominator of the FQH state at filling $\nu = 1/q$ of the lowest Landau level [3]. The fractional charge of FQH quasiparticles, or, more accurately, FQH quasiholes, was later unambiguously observed experimentally [24–26], thus confirming that fractionalization indeed occurs in the FQHE. Moreover, the quasiparticles obey fractional exchange statistics [27–30], meaning that upon the exchange of two such quasiparticles, the total wavefunction picks up a phase factor $e^{i\alpha\pi}$ with α different than 1 or -1, the latter two cases corresponding to Bose-Einstein and Fermi-Dirac statistics, respectively. Due to the fact that the wavefunctions of such quasiparticles can acquire any phase upon exchange, the quasiparticles themselves are called anyons [27]. The fractional exchange phase is the sought-after signature of anyons in quantum-interference experiments [31–33].

Since anyons can be thought of as being between fermions and bosons, it is reasonable to expect that they also obey intermediate exclusion principles [34]. To visualize this property, consider a system of $\mathcal{N}$ identical particles in a finite region of space. Define the dimension of the system's single-particle Hilbert space, whenever the states of $\mathcal{N}-1$ particles are kept fixed, as $d_{\mathcal{N}}$. This number depends on the total number $\mathcal{N}$ of the particles, in a way compatible with the statistics of the latter. This can be easily related to the dimension $D_{\mathcal{N}}$ of the Fock space for $\mathcal{N}$ fermionic or bosonic particles as

$$D_{\mathcal{N}} = \binom{d_{\mathcal{N}} + \mathcal{N} - 1}{\mathcal{N}}. \tag{1.38}$$

If d_1 is the dimension of the Hilbert space for a single particle in the system volume, then it is easy to see that, for $d_{\mathcal{N}} = d_1$ and $d_{\mathcal{N}} = d_1 - (\mathcal{N}-1)$, one

obtains the counting rules for the number of states in the Fock space of bosonic and fermionic particles, respectively. It is tempting to generalize this counting rule by interpolating between fermions and bosons. To this end, one may define the quantity

$$\beta := -\frac{d_{\mathcal{N}+\Delta\mathcal{N}} - d_{\mathcal{N}}}{\Delta\mathcal{N}}\,, \tag{1.39}$$

which describes the change in the single-particle Hilbert space, with $\mathcal{N}$ particles fixed in a fixed state, upon a variation $\Delta\mathcal{N}$ of the total number of particles. The parameter β, which must be a rational number for Equation (1.39) to make sense, is a characteristic assigned to the constituting particles and is called statistical interaction or exclusion coefficient. Equation (1.39) can be equivalently written as $d_{\mathcal{N}} - d_1 = -\beta(\mathcal{N}-1)$. The expression of Equation (1.38) then contains the counting rules for the size of both bosonic and fermionic Fock spaces, with $\beta = 0, 1$ respectively. The statistical interaction β thus allows for a dense interpolation between fermion and boson statistics.

Exact numerical calculations [35, 36], as well as analytical considerations of ansatz FQH wavefunctions [37], support the conclusion that, for FQH quasiholes, $\beta \neq 0, 1$. Generally, quasiholes in FQH states at $\nu = 1/q$ have $\alpha = \beta = 1/q$. In Section 5.2 we shall see that this is also the case for topological states generalizing FQH states to lattice systems. Another remark relevant to Section 5.2 is that FQH quasiholes are emergent particles that live in the FQH regime. Quasiholes can therefore condense into holes if an energy penalty is paid. Consequently, the states of the Fock space counted by the generalized exclusion principle of Equation (1.38) will form a low-energy manifold, separated by a gap from the rest of the energy spectrum.

Equation (1.38) yields $D_0 = 1$ for undoped FQH states. However, this is contrary to what was deduced in the preceding section. The reason for the discrepancy is the topological degeneracy in compact manifolds with genus higher than zero, which is a consequence of the freedom in selecting the center-of-mass coordinate of the many-body wavefunction [38]. Taking this into account, the counting rule for quasiholes in $\nu = 1/q$ FQH states becomes [39]

$$D_{\mathcal{N}}^{\text{torus}} := D_{\mathcal{N}} \times D'_{\mathcal{N}}\,, \tag{1.40}$$

where $D'_{\mathcal{N}} := d_{\mathcal{N}}(qd_{\mathcal{N}} + \mathcal{N})$ is the correction factor due to the topological degeneracy. Using the notation of the previous section, $D_{\mathcal{N}}^{\text{torus}}$ can be rewritten in a more convenient form as

$$D_N^{\text{torus}} = L_1 L_2 \frac{[L_1 L_2 - (q-1)N - 1]!}{N!(L_1 L_2 - qN)!}\,, \tag{1.41}$$

where the number of quasiholes has been expressed in terms of the number of electrons N as $\mathcal{N} \equiv L_1 L_2 - qN$. It is easily verified that, for $\mathcal{N} = 0$, the above expression yields the expected degeneracy for FQH states on the torus. This counting rule will be used to identify quasihole excitations in Chapter 5.

Quasiparticle fractionalization and topological degeneracy are the hallmarks of topological order. A quantum state is said to be topologically ordered whenever there is no local order parameter to characterize it[3], yet its presence shows

[3]Note that the Hall conductivity is not eligible for the role of an order parameter, as it also takes non-zero values between quantum-Hall plateaus and its magnitude is not indicative of how well a quantum-Hall phase is established.

up in a non-local quantity. In fact, in the context of the lowest Landau level, a finite density of fractionally charged quasiparticles can be used as the definition of a characteristic, albeit not measurable, quantity [40, 41]. More general signatures of topological order can be extracted from entanglement-related quantities, such as the topological entropy [42] or the entanglement spectrum [43].

Chapter 2

Topological states in lattices

Quantum Hall effects require cryogenic temperatures and strong magnetic fields to be observed. These limitations motivated a series of ideas on how to access the quantum-Hall regime more easily. To this end, physical settings other than the two-dimensional electron gas (2DEG) have to be sought. Given the abundance of crystalline solids, it is natural to investigate the possibility of a quantum Hall effect arising in a lattice system.

The Hofstadter model [44], which actually predates the discovery of both quantum Hall effects, is historically the first system, other than the 2DEG, that was theoretically predicted to exhibit both the integer and the fractional quantum Hall effects [45, 46], and its fractal energy spectrum has also been realized experimentally [47]. In the regime of the integer quantum Hall effect (IQHE), it amounts to applying a magnetic field perpendicular to a square lattice of non-interacting, tightly bound electrons. Thouless and co-workers unified the topological description of this problem and that of a Landau level by introducing the lattice as a periodic potential on top of the degenerate manifold of the 2DEG and then using a treatment along the lines of Section 1.1.2 [21].

In this Chapter, the discussion will revolve around lattice states that are beyond a "Landau level plus periodic potential" treatment. It will be shown below that the requirement of a strong external magnetic field for the emergence of quantum Hall states can be overcome by requiring a suitable arrangement of magnetic flux within the unit cell of a lattice with more than one sublattices. This idea, which was dubbed quantum anomalous Hall effect and is the subject of Section 2.2, was ingeniously encapsulated in the Haldane model [48], to be discussed in Section 2.2.1. The Haldane model is also the cornerstone of the field of topological insulators, which will be briefly introduced in Section 2.3. The most minimalistic systems that are adequate to introduce the quantum anomalous Hall effect, as well as its time-reversal symmetric generalizations, comprises of a single species of particles hopping on lattice with two sublattices. The essential elements of the tight-binding formalism are hence introduced in Section 2.1, along with some recurring nomenclature.

Part of this Chapter (in particular Section 2.2.2) has been previously published in Ref. [49] with J. Venderbos and M. Daghofer.

2.1 Tight-binding formalism

Consider a single species of particles that hop freely on a two-dimensional lattice Λ with two inequivalent sites A and B per unit cell belonging to sublattices Λ_A and Λ_B, respectively. Distances between nearest-neighboring sites of Λ are set to unity for convenience. Periodic boundary conditions are assumed in both spatial directions. In the tight-binding approximation, the general form of the kinetic energy is

$$\hat{\mathcal{H}}_{\text{kin}} := \sum_{\boldsymbol{k}\in\text{BZ}} \hat{\psi}^\dagger_{\boldsymbol{k}}\, H_{\boldsymbol{k}}\, \hat{\psi}_{\boldsymbol{k}}\,, \tag{2.1a}$$

where $\hat{\psi}^\dagger_{\boldsymbol{k}} \equiv \left(\hat{c}^\dagger_{\boldsymbol{k},A}\,, \hat{c}^\dagger_{\boldsymbol{k},B}\right)$ denotes an operator-valued spinor, whose upper and lower components create a particle with wavenumber $\boldsymbol{k}$ from the Brillouin zone (BZ) on the inequivalent sites A and B, respectively. The 2×2 matrix $H_{\boldsymbol{k}}$ can be expressed as

$$H_{\boldsymbol{k}} := g_{0,\boldsymbol{k}}\,\tau_0 + \boldsymbol{g}_{\boldsymbol{k}}\cdot\boldsymbol{\tau} + \mu_{\text{s}}\,\tau_3\,, \tag{2.1b}$$

where the 2×2 unit matrix τ_0 and the three Pauli matrices $\boldsymbol{\tau} = (\tau_1, \tau_2, \tau_3)$ are used to compactly represent terms acting on sublattices with indices A and B. The functions $g_{0,\boldsymbol{k}}$, $g_{1,\boldsymbol{k}}$, $g_{2,\boldsymbol{k}}$, and $g_{3,\boldsymbol{k}}$ are smooth real-valued functions of the wave-number $\boldsymbol{k}$ in the thermodynamic limit and the dependence on a staggered chemical potential $\mu_{\text{s}} \in \mathbb{R}$, assuming opposite values on each sublattice, has been included. In matrix form,

$$H_{\boldsymbol{k}} = \begin{pmatrix} g_{3,\boldsymbol{k}} + \mu_{\text{s}} & g_{1,\boldsymbol{k}} - \mathrm{i}g_{2,\boldsymbol{k}} \\ g_{1,\boldsymbol{k}} + \mathrm{i}g_{2,\boldsymbol{k}} & -g_{3,\boldsymbol{k}} - \mu_{\text{s}} \end{pmatrix} + g_{0,\boldsymbol{k}}\tau_0 = \begin{pmatrix} g_{3,\boldsymbol{k}} + \mu_{\text{s}} & w_{\boldsymbol{k}} e^{-\mathrm{i}\theta_{\boldsymbol{k}}} \\ w_{\boldsymbol{k}} e^{\mathrm{i}\theta_{\boldsymbol{k}}} & -g_{3,\boldsymbol{k}} - \mu_{\text{s}} \end{pmatrix} + g_{0,\boldsymbol{k}}\tau_0\,, \tag{2.2}$$

where $w_{\boldsymbol{k}} = \sqrt{g^2_{1,\boldsymbol{k}} + g^2_{2,\boldsymbol{k}}}$ and $\theta_{\boldsymbol{k}} = \arctan(g_{2,\boldsymbol{k}}/g_{1,\boldsymbol{k}})$. The eigenenergies are

$$\varepsilon_\pm = g_{0,\boldsymbol{k}} \pm g_{\boldsymbol{k}}\,, \tag{2.3}$$

with $g_{\boldsymbol{k}} := |\boldsymbol{g}_{\boldsymbol{k}}|$, and the corresponding eigenvectors are

$$\psi_\pm(\boldsymbol{k}) = (u_\pm e^{-\mathrm{i}\theta_{\boldsymbol{k}}/2},\ v_\pm e^{\mathrm{i}\theta_{\boldsymbol{k}}/2})^{\mathsf{T}}\,, \tag{2.4}$$

with

$$u_\pm = \pm\frac{1}{\sqrt{2}}\frac{g_{3,\boldsymbol{k}} \pm g_{\boldsymbol{k}}}{\sqrt{g^2_{\boldsymbol{k}} \pm g_{3,\boldsymbol{k}} g_{\boldsymbol{k}}}} \tag{2.5a}$$

$$v_\pm = \frac{1}{\sqrt{2}}\frac{\sqrt{g^2_{1,\boldsymbol{k}} + g^2_{2,\boldsymbol{k}}}}{\sqrt{g^2_{\boldsymbol{k}} \pm g_{3,\boldsymbol{k}} g_{\boldsymbol{k}}}}. \tag{2.5b}$$

When the two bands $\varepsilon_\pm$ are separated by an energy gap, each of them can be characterized by a topological invariant called the Chern number, which is essentially the quantized Hall conductivity of the full band. Instead of following the same strategy as in Section 1.1, an alternative proof will be presented here, in order to shed some more light on the topological aspect of the theory. In Section 1.1, a pseudomomentum vector with periodic components was introduced

via a unitary transformation and was used to derive the quantization of the Hall conductivity. In the present case, instead of the pseudomomentum, one can use the wavevector in the first Brilouin zone. Following the definitions of Equations (1.30), we have

$$\boldsymbol{A}_{\pm}(\boldsymbol{k}) := \langle \psi_{\pm}(\boldsymbol{k}) | \nabla_{\boldsymbol{k}} | \psi_{\pm}(\boldsymbol{k}) \rangle \ . \tag{2.6}$$

This quantity is called Berry connection. Taking its curl yields the Berry curvature

$$\boldsymbol{\Omega}_{\pm} = \mathrm{i} \nabla_{\boldsymbol{k}} \times \boldsymbol{A}_{\pm}(\boldsymbol{k}) \, . \tag{2.7}$$

The Berry connection is

$$\boldsymbol{A}_{\pm}(\boldsymbol{k}) = \frac{1}{2} \nabla_{\boldsymbol{k}} (u_{\pm}^2 + v_{\pm}^2) - \frac{i}{2} \nabla_{\boldsymbol{k}} \theta_{\boldsymbol{k}} \left(u_{\pm}^2 - v_{\pm}^2 \right) \ . \tag{2.8}$$

The only non-zero component of the Berry curvature is the one along $\boldsymbol{e}_3$ and will be denoted by $\Omega_{\pm}$ from now on. It becomes

$$\begin{aligned} \Omega_{\pm}(\boldsymbol{k}) = & \ \frac{i}{2} \boldsymbol{e}_3 \cdot \nabla_{\boldsymbol{k}} \times \nabla_{\boldsymbol{k}} (u_{\pm}^2 + v_{\pm}^2) + \frac{1}{2} \boldsymbol{e}_3 \cdot \nabla_{\boldsymbol{k}} \times [\nabla_{\boldsymbol{k}} \theta_{\boldsymbol{k}} (u_{\pm}^2 - v_{\pm}^2)] \\ = & \ \frac{1}{2} \boldsymbol{e}_3 \cdot \nabla_{\boldsymbol{k}} (u_{\pm}^2 - v_{\pm}^2) \times \nabla_{\boldsymbol{k}} \theta_{\boldsymbol{k}} \, , \end{aligned} \tag{2.9}$$

where the identities $\nabla \times (\nabla f) = 0$ and $\nabla \times (f \boldsymbol{v}) = (\nabla f) \times \boldsymbol{v} + f(\nabla \times \boldsymbol{v})$ have been used. Using the general expression for the coefficients of the wavefunctions $\psi_{\pm}$, one finds

$$u_{\pm}^2 - v_{\pm}^2 = \frac{g_3^2 \pm g_3 g}{g^2 \pm g_3 g} \, . \tag{2.10}$$

The gradient can now be calculated. The first coordinate is

$$\begin{aligned} \partial_{k_1} (u_{\pm}^2 - v_{\pm}^2) = & \ \frac{(2g_3 \pm g)(g^2 \pm g_3 g) \mp g(g_3^2 \pm g_3 g)}{(g^2 \pm g_3 g)^2} \partial_{k_1} g_3 \\ & \pm \frac{g_3 \mp (2g \pm g_3)(g_3^2 \pm g_3 g)}{g(g^2 \pm g_3 g)} \boldsymbol{g} \cdot \partial_{k_1} \boldsymbol{g} \\ = & \ \pm \frac{1}{g} \partial_{k_1} g_3 \mp \frac{g_3}{g^3} \boldsymbol{g} \cdot \partial_{k_1} \boldsymbol{g} \, . \end{aligned} \tag{2.11}$$

Furthermore,

$$\nabla_{\boldsymbol{k}} \theta_{\boldsymbol{k}} = \frac{g_1^2}{g_1^2 + g_2^2} \nabla_{\boldsymbol{k}} \left(\frac{g_2}{g_1} \right) = \frac{1}{g_1^2 + g_2^2} \begin{pmatrix} g_1 \partial_{k_1} g_2 - g_2 \partial_{k_1} g_1 \\ g_1 \partial_{k_2} g_2 - g_2 \partial_{k_2} g_1 \\ 0 \end{pmatrix} \ . \tag{2.12}$$

The Berry curvature then becomes consecutively

$$\begin{aligned} \Omega_{\pm}(\boldsymbol{k}) = & \ \pm \frac{1}{2gw^2} \left[\left(\partial_{k_1} g_3 - \frac{g_3}{g^2} \boldsymbol{g} \cdot \partial_{k_1} \boldsymbol{g} \right) \left(g_1 \partial_{k_2} g_2 - g_2 \partial_{k_2} g_1 \right) \right. \\ & \left. - \left(\partial_{k_2} g_3 - \frac{g_3}{g^2} \boldsymbol{g} \cdot \partial_{k_2} \boldsymbol{g} \right) \left(g_1 \partial_{k_1} g_2 - g_2 \partial_{k_1} g_1 \right) \right] \\ = & \ \mp \frac{1}{2g^3} \left[g_1 \left(\partial_{k_2} g_2 \partial_{k_1} g_3 - \partial_{k_1} g_2 \partial_{k_2} g_3 \right) \right. \\ & + g_2 \left(\partial_{k_1} g_3 \partial_{k_2} g_1 - \partial_{k_1} g_1 \partial_{k_2} g_3 \right) \\ & \left. + g_3 \left(\partial_{k_1} g_1 \partial_{k_2} g_2 - \partial_{k_1} g_2 \partial_{k_2} g_1 \right) \right] \, . \end{aligned} \tag{2.13}$$

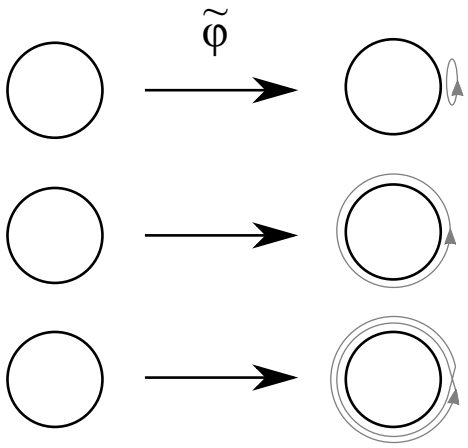

Figure 2.1: Illustration of possible mappings $\tilde{\phi} : S^1 \to S^1$ with winding numbers equal to 0, 1 and 2 (top, middle and bottom, respectively).

On the other hand, it is

$$\begin{aligned} \boldsymbol{g} \cdot \left(\partial_{k_1} \boldsymbol{g} \times \partial_{k_2} \boldsymbol{g} \right) = g_1 \left(\partial_{k_2} g_2 \partial_{k_1} g_3 - \partial_{k_1} g_2 \partial_{k_2} g_3 \right) \\ + g_2 \left(\partial_{k_1} g_3 \partial_{k_2} g_1 - \partial_{k_1} g_1 \partial_{k_2} g_3 \right) \\ + g_3 \left(\partial_{k_1} g_1 \partial_{k_2} g_2 - \partial_{k_1} g_2 \partial_{k_2} g_1 \right) , \end{aligned} \tag{2.14}$$

and therefore the Berry curvature becomes finally

$$\Omega_{\pm}(\boldsymbol{k}) = \mp \frac{1}{2g^3} \boldsymbol{g} \cdot \left(\partial_{k_1} \boldsymbol{g} \times \partial_{k_2} \boldsymbol{g} \right) = \mp \frac{1}{2} \boldsymbol{e_g} \cdot \left(\partial_{k_1} \boldsymbol{e_g} \times \partial_{k_2} \boldsymbol{e_g} \right) , \tag{2.15}$$

where $\boldsymbol{e_g}$ is the unitary vector in the direction of $\boldsymbol{g}$. The first Chern number, which is identical to the Hall conductivity of Equation (1.30), is defined as

$$C_{\pm} := \mp \frac{1}{4\pi} \iint_{\boldsymbol{k} \in \mathrm{BZ}} d\boldsymbol{k} \; \boldsymbol{e_g} \cdot \left(\partial_{k_1} \boldsymbol{e_g} \times \partial_{k_2} \boldsymbol{e_g} \right) . \tag{2.16}$$

Since the components of $\boldsymbol{e_g}$ are smooth functions of $\boldsymbol{k} \in T^2$, where T^2 is the unit 2-torus (in units of 2π), and since $\boldsymbol{e_g}$ is a unit vector in $\mathbb{R}^2$, it can be viewed as a mapping $\boldsymbol{e_g} : T^2 \to S^2$, where S^2 is the unit 2-sphere. These mappings fall into equivalence classes. Consider, for example, the mapping $\tilde{\phi} : S^1 \to S^1$. This is characterized by a winding number, i.e., the number of times the target manifold is traversed by $\tilde{\phi}$ upon traversing the base manifold once. If the S^1 manifold is embedded in a two-dimensional world, then mappings with different winding number cannot be continuously deformed into one another, as can be seen in the cartoon of Figure 2.1. Mappings with the same winding number, on the other hand, fall into the same equivalence class. The set of all equivalence classes of mappings $\phi : S^d \to X$ (the homotopy classes) is called the dth homotopy group $\pi_d(X)$. In the present case, the inverse mapping $\boldsymbol{e_g}^{-1}$ belongs to $\pi_2(T^2)$.

This rather unattractive exercise leads into the mathematical core of topological insulation. The first Chern number, as defined in Equation (2.15), is the winding number of $\boldsymbol{e_g}$ and represents the homotopy class of $\boldsymbol{e_g}^{-1}$. Since any continuous deformation of $\boldsymbol{e_g}$ necessarily leads to the same homotopy class, as exemplified by the circle mapping, the Chern number, i.e., the Hall conductivity, can change only if $\boldsymbol{e_g}$ goes through a singularity. From Eq. (2.3), it is seen that this happens when $g = \varepsilon_+ - g_0 = g_0 - \varepsilon_- = 0$, which is equivalent to saying that the gap between the two Chern bands closes at some point in the Brillouin zone. This illustrates the notion of topological invariance of a physical quantity. The parameters for which the gap becomes zero mark a topological quantum phase transition. This line of thought is only valid as-is for non-interacting systems. It can also be used, with appropriate approximations, whenever interactions are weak, but has to be abandoned altogether in the case of strongly correlated states.

2.2 Quantum anomalous Hall effect

2.2.1 Haldane model

Consider the following Hamiltonian, describing a single species of electrons on the honeycomb lattice:

$$\hat{\mathcal{H}}_{\text{graphene}} = t \sum_{\langle \boldsymbol{i},\boldsymbol{j} \rangle} (\hat{c}_{\boldsymbol{i}}^\dagger \hat{c}_{\boldsymbol{j}} + \text{H.c.}) + \mu_{\text{s}} \sum_{\boldsymbol{i} \in \Lambda_A} \hat{c}_{\boldsymbol{i}}^\dagger \hat{c}_{\boldsymbol{i}} - \mu_{\text{s}} \sum_{\boldsymbol{i} \in \Lambda_B} \hat{c}_{\boldsymbol{i}}^\dagger \hat{c}_{\boldsymbol{i}} \,, \tag{2.17}$$

where t is the matrix element for hopping between nearest-neighboring sites at positions $\boldsymbol{i}$ and $\boldsymbol{j}$, denoted by $\langle \boldsymbol{i}, \boldsymbol{j} \rangle$, $\mu_{\text{s}} \geq 0$ is a chemical potential (or "mass") with opposite sign on sublattices Λ_A and Λ_B, and $\hat{c}_{\boldsymbol{i}}^\dagger$ and $\hat{c}_{\boldsymbol{i}}$ create and annihilate electrons at the site in position $\boldsymbol{i}$, respectively. The honeycomb lattice is triangular with primitive vectors $\boldsymbol{a}_1 = (\sqrt{3}, 0)$ and $\boldsymbol{a}_2 = (\sqrt{3}/2, 3/2)$, where the lattice constant has been set to unity. The positions of the two sites A and B in the unit cell are offset from lattice vectors by $(0, 0)$ and $(0, 1)$, respectively. The nearest neighbors of any given site on sublattice Λ_A are located at

$$\begin{aligned} \boldsymbol{\delta}_1 &= \frac{2\boldsymbol{a}_1 - \boldsymbol{a}_2}{3} = (\sqrt{3}/2, -1/2) \\ \boldsymbol{\delta}_2 &= \frac{2\boldsymbol{a}_2 - \boldsymbol{a}_1}{3} = (0, 1) \\ \boldsymbol{\delta}_3 &= -\frac{\boldsymbol{a}_1 + \boldsymbol{a}_2}{3} = (-\sqrt{3}/2, -1/2) \,, \end{aligned} \tag{2.18}$$

whereas the nearest neighbors of sites belonging to sublattice Λ_B are at $-\boldsymbol{\delta}_1$, $-\boldsymbol{\delta}_2$ and $-\boldsymbol{\delta}_3$ with respect to any B site. The lattice geometry is shown in Figure 2.2(a). The Brillouin zone is spanned by the reciprocal-lattice vectors

$$\begin{aligned} \boldsymbol{b}_1 &= 2\pi \frac{\boldsymbol{a}_2 \times \boldsymbol{e}_3}{\boldsymbol{a}_1 \cdot \boldsymbol{a}_2 \times \boldsymbol{e}_3} = \frac{4\pi}{3\sqrt{3}} \left(\frac{3}{2}, -\frac{\sqrt{3}}{2} \right) \\ \boldsymbol{b}_2 &= 2\pi \frac{\boldsymbol{e}_3 \times \boldsymbol{a}_1}{\boldsymbol{a}_1 \cdot \boldsymbol{a}_2 \times \boldsymbol{e}_3} = \frac{4\pi}{3\sqrt{3}} \left(0, \sqrt{3} \right) . \end{aligned} \tag{2.19}$$

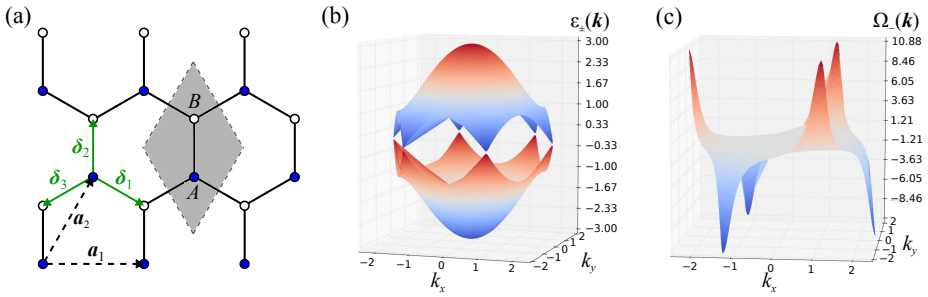

Figure 2.2: (a) The graphene lattice. (b) Energy spectrum of nearest-neighbor tight-binding model of graphene for $m \to 0$. (c) Berry curvature in units of 2π of the lower band of graphene for $m/t = 0.5$; the integral of the Berry curvature over the Brillouin zone is precisely $C = 0$.

After a Fourier transform, the Hamiltonian can be written compactly, using the formalism of the previous section, as

$$\hat{\mathcal{H}}_{\text{graphene}} := \sum_{\boldsymbol{k}\in \text{BZ}} \hat{\psi}^\dagger_{\boldsymbol{k}} H_{\boldsymbol{k}} \hat{\psi}_{\boldsymbol{k}} \,, \tag{2.20}$$

with

$$H_{\boldsymbol{k}} = \begin{pmatrix} \mu_{\text{s}} & tf(\boldsymbol{k}) \\ tf^*(\boldsymbol{k}) & -\mu_{\text{s}} \end{pmatrix} \,, \tag{2.21}$$

where $f(\boldsymbol{k}) = \sum_{j=1}^{3} e^{\text{i}\boldsymbol{k}\cdot\boldsymbol{\delta}_j}$. The eigenenergies are

$$E_\pm(\boldsymbol{k}) = \pm\sqrt{t^2 f^2(\boldsymbol{k}) + \mu_{\text{s}}^2} \,. \tag{2.22}$$

The two energy branches are shown in Figure 2.2(b).

For $\mu_{\text{s}} \to 0$, two inequivalent Dirac nodes develop in the Brillouin zone at the Fermi points $\boldsymbol{K} = (4\pi/3\sqrt{3}, 0)$ and $\boldsymbol{K}' = -\boldsymbol{K}$, which are inversion-symmetry related. The dispersion is approximately linear around $\boldsymbol{K}$ and $\boldsymbol{K}'$. The tight-binding matrix elements can hence be expanded in a Taylor series around $\boldsymbol{K}$ as

$$f(\boldsymbol{k}) \simeq f(\boldsymbol{K}) + \nabla_{\boldsymbol{k}} f(\boldsymbol{k})|_{\boldsymbol{k}=\boldsymbol{K}} \cdot (\boldsymbol{k} - \boldsymbol{K}) \,. \tag{2.23}$$

The gradient term is

$$\nabla_{\boldsymbol{k}} f(\boldsymbol{k})|_{\boldsymbol{k}=\boldsymbol{K}} = \text{i} \sum_{j=1}^{3} e^{\text{i}\boldsymbol{K}\cdot\boldsymbol{\delta}_j} \boldsymbol{\delta}_j \,, \tag{2.24}$$

so that

$$f(\boldsymbol{K} + \boldsymbol{k}) \simeq \text{i} \sum_{j=1}^{3} e^{\text{i}\boldsymbol{K}\cdot\boldsymbol{\delta}_j} \boldsymbol{\delta}_j \cdot \boldsymbol{k} \,. \tag{2.25}$$

Substituting into $H_{\boldsymbol{k}}$ gives

$$H^{\boldsymbol{K}}_{\boldsymbol{k}} = v_F \boldsymbol{\tau}' \cdot \boldsymbol{k} + \tau_3 \mu_{\text{s}}, \tag{2.26}$$

where the origin of $\boldsymbol{k}$ is now $\boldsymbol{K}$, $\boldsymbol{\tau}' = (\tau_1, \tau_2)$ is a vector of the first two Pauli matrices and the Fermi velocity has been defined as $v_F := 3t/2$. Similarly, one gets for the $\boldsymbol{K}'$ point

$$H_{\boldsymbol{k}}^{\boldsymbol{K}'} = v_F \boldsymbol{\tau}'' \cdot \boldsymbol{k} + \sigma_3 \mu_{\mathrm{s}}, \tag{2.27}$$

where $\boldsymbol{\tau}'' = (-\tau_1, \tau_2)$. Writing $k_1 + \mathrm{i}k_2 = |\boldsymbol{k}| e^{\mathrm{i}\theta_{\boldsymbol{k}}}$, the effective Hamiltonian matrix at $\boldsymbol{K}$ becomes

$$H_{\boldsymbol{k}}^{\boldsymbol{K}} = \begin{pmatrix} \mu_{\mathrm{s}} & v_F |\boldsymbol{k}| e^{-\mathrm{i}\theta_{\boldsymbol{k}}} \\ v_F |\boldsymbol{k}| e^{\mathrm{i}\theta_{\boldsymbol{k}}} & -\mu_{\mathrm{s}} \end{pmatrix}. \tag{2.28}$$

This belongs to the general class of Bloch Hamiltonians introduced in the previous section and the expressions for the Berry curvature and Chern number are directly applicable. When $\mu_{\mathrm{s}} \to 0$, the only appreciable contributions to the Berry curvature come from points $\boldsymbol{K}$ and $\boldsymbol{K}'$. From the expressions for $H_{\boldsymbol{k}}^{\boldsymbol{K}}$ and $H_{\boldsymbol{k}}^{\boldsymbol{K}'}$, one obtains respectively

$$\Omega_{\boldsymbol{K},\pm}(\boldsymbol{k}) = \pm \frac{\mu_{\mathrm{s}}/v_F}{2(k^2 + \mu_{\mathrm{s}}^2/v_F^2)^{3/2}} \tag{2.29a}$$

$$\Omega_{\boldsymbol{K}',\pm}(\boldsymbol{k}) = \mp \frac{\mu_{\mathrm{s}}/v_F}{2(k^2 + \mu_{\mathrm{s}}^2/v_F^2)^{3/2}}\,. \tag{2.29b}$$

This sign difference in the Berry curvature at points $\boldsymbol{K}$ and $\boldsymbol{K}'$ can also be seen in Figure 2.2. The integration over momenta is

$$\begin{aligned} \int d\boldsymbol{k}\, k \frac{\mu_{\mathrm{s}}/v_F}{2(k^2 + \mu_{\mathrm{s}}^2/v_F^2)^{3/2}} &= \int_0^{2\pi} d\phi \int_0^{\infty} dk\, k \frac{\mu_{\mathrm{s}}/v_F}{2(k^2 + \mu_{\mathrm{s}}^2/v_F^2)^{3/2}} \\ &= -\frac{2\pi\mu_{\mathrm{s}}}{2v_F} \left[\frac{1}{\sqrt{k^2 + \mu_{\mathrm{s}}^2/v_F^2}} \right]_0^{\infty} = \pi\,. \end{aligned} \tag{2.30}$$

One therefore finds

$$C_{\pm} = \frac{1}{2\pi} \int d\boldsymbol{k}\, (\Omega_{\boldsymbol{K},\pm} + \Omega_{\boldsymbol{K}',\pm}) = \pm\frac{1}{2} \mp \frac{1}{2} = 0\,. \tag{2.31}$$

The Chern number evidently does not depend on the precise value of μ_{s}, as long as the bands remain gapped.

Now, consider the case where, instead of the constant μ_{s}, one has a momentum-dependent mass $g_{3,\boldsymbol{k}}$ with the property $g_{3,\boldsymbol{K}} = -g_{3,\boldsymbol{K}'}$. In this case, it is

$$\Omega_{\boldsymbol{K},\pm}(\boldsymbol{k}) = \pm \frac{g_{3,\boldsymbol{k}}/v_F}{2(k^2 + g_{3,\boldsymbol{k}}^2/v_F^2)^{3/2}} = \Omega_{\boldsymbol{K}',\pm}(\boldsymbol{k}) \tag{2.32}$$

and therefore

$$C_{\pm} = \frac{1}{2\pi} \int d\boldsymbol{k}\, (\Omega_{\boldsymbol{K},\pm} + \Omega_{\boldsymbol{K}',\pm}) = \pm \left(\frac{1}{2} + \frac{1}{2} \right) = \pm 1. \tag{2.33}$$

This is precisely the idea behind the Haldane model [50]. The mass $g_{3,\boldsymbol{k}}$ that induces the topological non-triviality, called the Haldane mass, comes from complex second-nearest neighbor hoppings. In the formalism of the previous section,

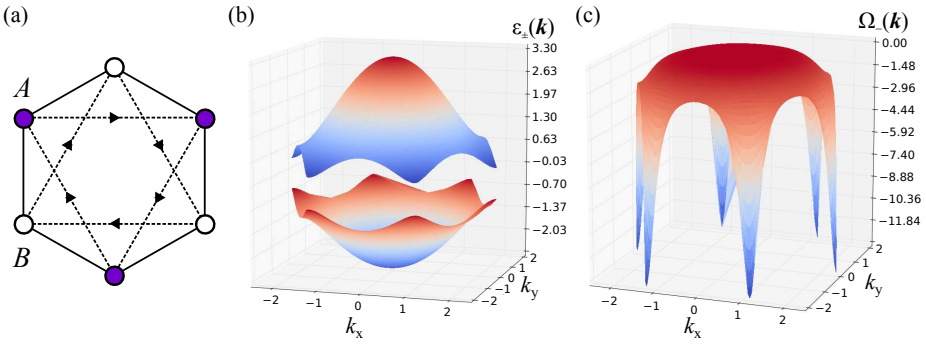

Figure 2.3: (a) The Haldane model; solid lines denote nearest-neighbor hoppings; hopping in the direction an arrow points to adds φ to the phase of the electron wave function, hopping in the opposite direction subtracts φ. (b) Energy spectrum of the Haldane model for $t_2/t = 0.1$ and $\varphi = \pi/3$. (c) Berry curvature in units of 2π of the lower Chern band of the Haldane model for $t_2/t = 0.1$ and $\varphi = \pi/3$; the integral of the Berry curvature over the Brillouin zone is precisely $C = -1$.

the Haldane model can be written as

$$g_{0,\boldsymbol{k}} = 2t_2 \cos\varphi \sum_{i=1}^{3} \cos \boldsymbol{k} \cdot \boldsymbol{a}_i \,, \tag{2.34a}$$

$$g_{1,\boldsymbol{k}} = t \sum_{i=1}^{3} \cos \boldsymbol{k} \cdot \boldsymbol{\delta}_i \,, \tag{2.34b}$$

$$g_{2,\boldsymbol{k}} = t \sum_{i=1}^{3} \sin \boldsymbol{k} \cdot \boldsymbol{\delta}_i \,, \tag{2.34c}$$

$$g_{3,\boldsymbol{k}} = -2t_2 \sin\varphi \sum_{i=1}^{3} \sin \boldsymbol{k} \cdot \boldsymbol{a}_i \,, \tag{2.34d}$$

where $\boldsymbol{a}_3 = \boldsymbol{a}_2 - \boldsymbol{a}_1$ and t_2 is the amplitude for hoppings between second-nearest neighboring sites. A phase $\pm\varphi$ is added to the phase of the electron wavefunction whenever an electron hops within the same sublattice, as illustrated in Figure 2.3(a). This phase corresponds to a magnetic-flux pattern penetrating the unit cell. Note, however, that an electron that hops via nearest-neighbor hoppings around the elementary hexagon does not feel the flux. This is because the net flux passing through the unit cell averages out to zero, while closed hopping paths that only partially encircle the unit cell are the only ones that lead to phase factors. Since the full lattice is comprised of an integer multiple of unit cells, the total flux that permeates the system is zero. Second-neighbor hoppings open a gap in the graphene spectrum, as can be seen in Figure 2.3(b). The Berry curvature of each of the two bands now sums up to a non-zero integer value, as shown in Figure 2.3(c) for the lower band of the Haldane model.

For any $\varphi \neq 0, \pi$, the bands of the Haldane model are characterized by non-zero Chern numbers and are hence called Chern bands. The insulating state of matter that corresponds to half-filling the Haldane model, or any of its

equivalents, is called a Chern insulator. Taking once again the analogy to the quantum Hall effects into account, one sees that single-particle states in a Chern band are enumerated by the values of $\boldsymbol{k}$, and their number is equal to the number of unit cells in the lattice. These "orbitals" are not perfectly degenerate, unlike the ones in the lowest Landau level (compare to the discussion in Section 1.1.2). One may therefore wonder whether fractional quantum anomalous Hall states are tenable in this setting. This is one of the topics discussed in Part II.

At this point, in order to fully appreciate the virtues of Haldane's model, it is useful to briefly compare it to another lattice model yielding topologically non-trivial bands, namely, the Hofstadter model [44]. Consider free spinless fermions hopping on a square lattice subject to a strong uniform magnetic field applied perpendicularly with respect to the lattice plane. The Hamiltonian describing this system can be written as

$$\mathcal{H}_{\text{Hofstadter}} := \sum_{m,n} (\hat{c}^\dagger_{m+1,n}\hat{c}_{m,n} + e^{\mathrm{i}\tilde{\varphi}m}\hat{c}^\dagger_{m,n+1}\hat{c}_{m,n} + \text{H.c.}) \,, \tag{2.35}$$

where sites are now indexed by two integers, which represent position as multiples of the lattice constant in $\hat{x}$ and $\hat{y}$ directions respectively, and $\tilde{\varphi} := 2\pi p/q$ with p, q integers is the flux passing through each elementary square plaquette. In analogy to the discussion of the Hall conductivity in Section 1.1.2, the magnetic unit cell contains q square plaquettes. Even though they both describe tightly bound electrons hopping on a lattice penetrated by magnetic flux, the Hofstadter and Haldane models are quite distinct. The following characteristics illustrate why:

1. For $q \gg 1$, the energy spectrum of the Hofstadter model comprises of many bands, most of which are perfectly flat. The flat bands in this regime, which is known as the weak-lattice limit, are fully equivalent to Landau levels and can be treated accordingly [21]. There is no straightforward way to do the same for the Haldane model. Furthermore, the Haldane model always has only two (dispersive) bands, for any $\varphi \neq 0, \pi$.

2. In the Hofstadter model, the phase picked up by the wavefunction whenever a particle hops around a closed path is proportional to the area the path bounds. This is not the case in the Haldane model.

3. Both models are gapless when $\varphi = \tilde{\varphi} = \pi$. However, for the Hofstadter model, this means that there is no way to have a gapped spectrum with only two bands[1]. This is readily achieved in the Haldane model for any $\varphi \neq 0, \pi$.

Even though the Hofstadter model may look more natural, the magnetic fields required in order to have a reasonably gapped spectrum are quite large. Consequently, a realization of this model has only been feasible in the weak-lattice limit, which is reached by adding a superlattice on top of a two-dimensional electron gas system [47]. In this incarnation, the resulting system is described more closely by the Landau-level physics of Chapter 1 than by a true lattice model. The Haldane model is more relevant in the physical settings that follow, partly because there the lattice plays an instrumental role.

[1] This is most evident in recent attempts at interpolating between the Hofstadter and a Haldane-like model, in which additional sites are adiabatically introduced in the unit cell, leading to a different number of bands in the Hofstadter limit [51].

2.2.2 Itinerant magnets

The Haldane model, even though appearing quite artificial to be actually realized, paved the way towards relaxing the experimental requirements for the observation of the IQHE, by removing the caveat of an externally applied magnetic field. An idea that has the potential to make the artificial-looking flux arrangements of Figure 2.3 more realistic is to interpret the flux as Berry phases, arising due to the precession of the spins of itinerant electrons moving in a non-uniform magnetic background. This idea finds its natural setting in itinerant magnets, in which itinerant electrons are coupled to localized magnetic moments. An appealing advantage of considering particles interacting with spins is that topological states may develop spontaneously, in conjunction with Landau-ordered magnetic states, due to a symmetry-breaking mechanism. One therefore hopes that the benefits of introducing magnetic interactions will outweigh the additional complications arising from correlations. A further motivation for considering interacting systems as potential hosts for quantum-Hall physics is that they could facilitate the observation of a quantum Hall effect at higher temperatures, if a favorable setting is generated by condensed phases of characteristic energy scales larger than that of thermal fluctuations. Strongly correlated systems hence come intuitively to mind as plausible candidates.

To elucidate this possibility, consider the Kondo-lattice model

$$\hat{\mathcal{H}}_{\text{Kondo}} = \sum_{\langle \boldsymbol{i},\boldsymbol{j}\rangle,\sigma} t_{\boldsymbol{ij}} \left(\hat{c}^{\dagger}_{\boldsymbol{i},\sigma} \hat{c}_{\boldsymbol{j},\sigma} + \text{H.c.} \right) - J_{\text{Kondo}} \sum_{\boldsymbol{i}} \hat{\boldsymbol{S}}_{\boldsymbol{i}} \cdot \hat{\boldsymbol{s}}_{\boldsymbol{i}} \,, \tag{2.36}$$

where $t_{\boldsymbol{ij}}$ is the amplitude for the hopping from lattice position $\boldsymbol{i}$ to $\boldsymbol{j}$, $\langle \boldsymbol{i},\boldsymbol{j}\rangle$ denotes nearest-neighbor bonds, $\hat{c}_{\boldsymbol{i},\sigma}$ ($\hat{c}^{\dagger}_{\boldsymbol{i},\sigma}$) annihilates (creates) an electron with spin σ at position $\boldsymbol{i}$, and $\hat{\boldsymbol{s}}_{\boldsymbol{i}}$ is the corresponding vector of electronic spin operators. J_{Kondo} couples the itinerant electrons to a localized spin $\hat{\boldsymbol{S}}_{\boldsymbol{i}}$. In the following, the localized spin will be considered classical, i.e., $\hat{\boldsymbol{S}}_{\boldsymbol{i}} \equiv \boldsymbol{S}_{\boldsymbol{i}}$ is a vector in three-dimensional space.

In this regime, it is convenient to go over to a local spin-quantization axis, where "↑" ("↓") refers to parallel (antiparallel) orientation of the electron's spin to the local axis. This simplifies the exchange term to

$$-J_{\text{Kondo}} \sum_{\boldsymbol{i}} \boldsymbol{S}_{\boldsymbol{i}} \cdot \hat{\boldsymbol{s}}_{\boldsymbol{i}} = -J_{\text{Kondo}} \sum_{\boldsymbol{i}} (\hat{n}^{\uparrow}_{\boldsymbol{i}} - \hat{n}^{\downarrow}_{\boldsymbol{i}})/2 \,, \tag{2.37}$$

where $\hat{n}^{\uparrow}_{\boldsymbol{i}}$ ($\hat{n}^{\downarrow}_{\boldsymbol{i}}$) is the electron density at site $\boldsymbol{i}$ with spin (anti-) parallel to the localized spin. This local spin definition is particularly convenient in the limit $J_{\text{Kondo}} \to \infty$, where electron spins are forced to be perfectly aligned to the local moment at each site, therefore freezing the spin degree of freedom. In this case, one only keeps the "↑" states with electron spins parallel to the local spin-quantization axis and electrons effectively become spinless fermions. This can be described by transforming the hoppings as [52, 53]

$$t_{\boldsymbol{ij}} \to t_{\boldsymbol{ij}} \cos\frac{\theta_{\boldsymbol{i}}}{2} \cos\frac{\theta_{\boldsymbol{j}}}{2} + \sin\frac{\theta_{\boldsymbol{i}}}{2} \sin\frac{\theta_{\boldsymbol{j}}}{2} e^{-\mathrm{i}(\phi_{\boldsymbol{i}} - \phi_{\boldsymbol{j}})} \,, \tag{2.38}$$

where the set of angles $\theta_{\boldsymbol{i}}$ and $\phi_{\boldsymbol{i}}$ are the polar and azimuthal angles corresponding to $\boldsymbol{S}_i$, respectively. After some trigonometry, it can be seen that the

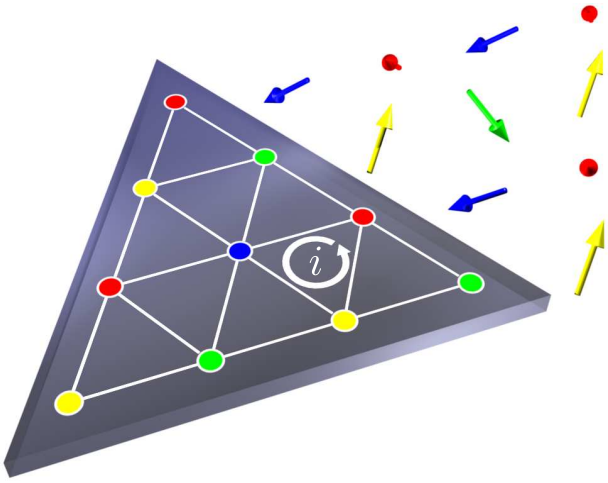

Figure 2.4: Illustration of chiral spin pattern and Berry phase introduced to the hoppings of itinerant electrons due to the presence of the magnetic texture.

magnitude of the transformed hoppings $\tilde{t}_{\boldsymbol{ij}}$ is

$$|\tilde{t}_{\boldsymbol{ij}}| = |t_{\boldsymbol{ij}}| \cos \frac{\theta_{\boldsymbol{ij}}}{2} , \tag{2.39}$$

where $\theta_{\boldsymbol{ij}}$ is the relative angle between spins at positions $\boldsymbol{i}$ and $\boldsymbol{j}$. Being generally complex numbers, the transformed hoppings can be written as

$$\tilde{t}_{\boldsymbol{ij}} = t_{\boldsymbol{ij}} e^{\mathrm{i}\alpha_{\boldsymbol{ij}}} \cos \frac{\theta_{\boldsymbol{ij}}}{2} . \tag{2.40}$$

The magnetic structure of the localized spins therefore modulates the magnitudes of the hoppings and also introduces a gauge-like contribution to them. The phase $\alpha_{\boldsymbol{ij}}$, which represents the vector-potential difference between lattice positions $\boldsymbol{i}$ and $\boldsymbol{j}$, is called geometric or Berry phase [54] and pervades a large part of condensed matter and physics in general [55].

Itinerant electrons mediate an interaction between the localized spins, which typically competes with antiferromagnetic spin-spin interactions; on frustrated lattices, this competition can resolve itself in non-coplanar phases [56–59]. In these cases, the complex factor introduced in $\tilde{t}_{\boldsymbol{ij}}$ cannot be gauged away, and it has been shown that non-coplanar spin configurations can endow the electronic bands with a nontrivial topology [56, 60, 61]. This effect has manifested itself in the observation of the anomalous Hall effect in materials with a geometrically frustrated lattice structure, such as the pyrochlore compound $Nd_2Mo_2O_7$ [61], the frustrated highly correlated compound UCu_5 [62] and the triangular-lattice antiferromagnet $PdCrO_2$ [63]. The quantum anomalous Hall effect, however, has not been observed in itinerant magnets yet and attempts to realize it have only recently become fruitful, albeit in a different setting involving a magnetic topological insulator [64]. Other notable candidates for the realization of the quantum anomalous Hall effect, to which the above modeling can be applied, include the triangular lattices formed by Mn monolayers on Cu(111) surfaces [65] and by the nuclear-spin ground state of a two-dimensional ^{3}He system [66].

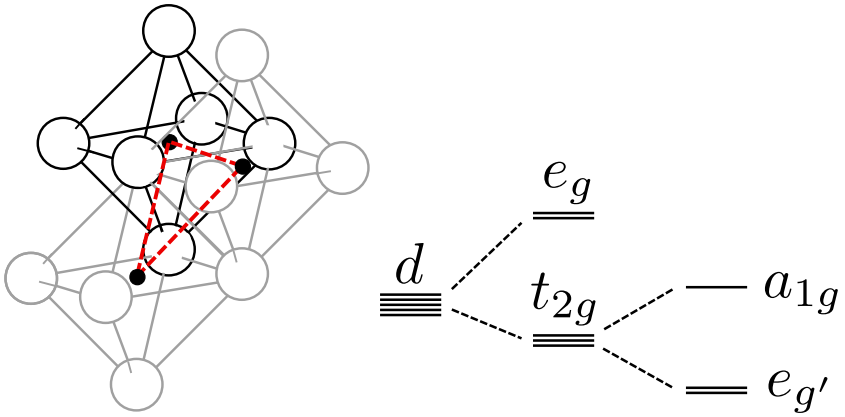

(a) (b)

Figure 2.5: (a) Illustration of a triangular-lattice plane built of edge-sharing oxygen octahedra. (b) The five d orbitals of the transition-metal ion in the center are split into an e_g doublet and a t_{2g} triplet due to the local cubic symmetry; the latter is further split into one a_{1g} state and an e'_g doublet; the latter splitting is exaggerated for visibility.

Another potential setting for a triangular Kondo-lattice model and the aforementioned non-triviality arises in layered perovskite structures of transition-metal oxides of the form ABO_2 [67, 68]. When the local symmetry around a transition-metal ion is cubic, with ligand oxygens forming an octahedron as depicted in Figure 2.5(a), the degeneracy between d levels is split, because the two e_g orbitals, i.e. $x^2 - y^2$ and $3z^2 - r^2$, point toward the negatively charged oxygens, while the three t_{2g} levels have their lobes in between. Consequently, the energy of e_g levels is higher. If the width of a triangular layer made of octahedra is compressed (extended) via a Jahn-Teller distortion, the energy of the highly symmetric orbital state $|a_{1g}\rangle = (|xz\rangle + |yz\rangle + |xy\rangle)/\sqrt{3}$ is raised (lowered) with respect to the remaining e'_g doublet. The presence of a strong on-site Coulomb interaction of strength U means that, when the d shell is less than half-filled, all electrons will be forced to have the same orientation locally to avoid an energetic penalty, and will fill up the available levels obeying Hund's rules. However, electrons on different sites need not be aligned. Whenever two electrons fill the e'_g levels, they can be effectively treated as a localized spin-1 object, since any excitations are gapped due to the Jahn-Teller distortion. Any additional electron density will have predominantly a_{1g} character and will be coupled to the effective e'_g moment via Hund's rule coupling. This coupling, along with the hopping of a_{1g} electrons motivates an effective Kondo-lattice description, thus mapping the system back to the itinerant-magnet scenario presented above. For exactly 2.5 electrons in the d shell of each transition-metal ion, the localized moments will accordingly form a chiral pattern. It can be shown [49, 68] that the wavefunction of an electron hopping in the fixed magnetic background of the chiral spin pattern acquires Berry phases that give rise to an effective Haldane-like model [see Equations (3.4)], which will be comprehensively studied in Part II.

2.3 Time-reversal invariant topological states

All quantum Hall effects discussed so far – integer, fractional or anomalous – occur in systems where time-reversal symmetry is broken, either by an externally applied magnetic field, or by the effective local field that corresponds to Berry phases in the hoppings. Even though this dissertation deals exclusively with the archetypal case of broken time-reversal symmetry, the next conceptual step, which is to realize a topological state while keeping time-reversal symmetry intact, will be briefly outlined in this Section. Time-reversal symmetry, which is present in most solid-state systems, has allowed for the recent observation of topological states.

The most straightforward – albeit unrealistic – way to visualize this setting is to consider two decoupled spin species hopping in the honeycomb lattice with a Haldane mass. The tight-binding formulation of this system, called the Kane-Mele model [69], is equivalent to considering two copies of the Haldane model simultaneously. The band structure of such a model is identical to the one shown in Figure 2.3, but the bands will be doubly degenerate. "Up" and "down" electrons will contribute to the Hall conductivity equally in magnitude, but the two contributions $\sigma^{\uparrow}$ and $\sigma^{\downarrow}$ will have opposite signs, totaling to $\sigma = \sigma^{\uparrow} + \sigma^{\downarrow} = 0$.

This, however, does not mean that there is no topological invariant characterizing this system. Define the spin Hall conductivity as

$$\sigma_{\text{spin}} = \frac{\hbar}{2e}(\sigma^{\uparrow} - \sigma^{\downarrow})\,. \tag{2.41}$$

In the Kane-Mele model, this quantity is quantized whenever the chemical potential lies within the energy gap between the two degenerate pairs of bands and can only take the values $\nu e/2\pi$ with $\nu = 0, 1$, depending on whether the mass term is topologically trivial or not. The quantization of σ_{spin} is termed the quantum spin Hall effect [69, 70]. It was furthermore realized that ν is a topological invariant, protected by the time-reversal symmetry of the underlying physical system, even in the case where the two spin species are coupled via a spin-orbit coupling term [71, 72]. In fact, it is possible that spin-orbit coupling alone, if suitably engineered, can induce the associated topological non-triviality, i.e., can play the same role as the Haldane mass in the quantum anomalous Hall effect. A state with a finite quantized spin Hall conductivity – named a Z_2 topological insulator due to the binary character of ν – was predicted to arise in quantum wells of HgTe sandwiched between CdTe [73] and was later experimentally observed [74]. Topological insulators were also envisioned in three-dimensional structures [72], a prediction that was verified experimentally [75]. All topological states of non-interacting particles were subsequently exhaustively classified into symmetry classes in any number of dimensions [76, 77].

The existence of the Z_2 topological invariant ν has repercussions on the band theory of solids. The fact that topological insulators are symmetry-protected states allows for an efficient evaluation of ν directly from the form of the Hamiltonian [72], much like the winding-number interpretation of the Chern number. A two-band tight-binding Hamiltonian for two spin species can be expressed generally in the matrix form $\mathcal{H}(\boldsymbol{k}) = d_0(\boldsymbol{k})I + \boldsymbol{d}(\boldsymbol{k}) \cdot \boldsymbol{\Gamma}$, where $\boldsymbol{d}$ is a five-component vector in the space spanned by the Dirac matrices $\boldsymbol{\Gamma} = (\sigma^1 \otimes I, \sigma^2 \otimes I, \sigma^3 \otimes \tau^1, \sigma^3 \otimes \tau^2, \sigma^3 \otimes \tau^3)$, with σ^i and τ^i Pauli matrices representing sublattice and spin species respectively, I is the 2×2 unity matrix

in spin space and $\otimes$ denotes the Kronecker product. Provided that there is an energy gap throughout the Brillouin zone, the Z_2 topological invariant ν is given by the relation $(-1)^\nu = \prod_{i=1}^{4} \delta_i$, where $\delta_i = -\mathrm{sgn}[d_1(\boldsymbol{k}_i)]$ and $\boldsymbol{k}_i$ are the time-reversal invariant points in the first Brillouin zone. The time-reversal invariant points are those with the property $-\boldsymbol{k}_i = \boldsymbol{k}_i + \boldsymbol{G}$, where $\mathbf{G}$ is a reciprocal-lattice vector. A simple application to the spinful generalizations of graphene ($\nu = 0$) and the Haldane model ($\nu = 1$) exemplify the Z_2 classification.

A final comment concerning edge states in time-reversal invariant topological states is in order. Since topological insulators, in their simplest incarnation are two copies of an integer quantum Hall effect, simple symmetry considerations suggest that edge channels in topological insulators should come in pairs, with each one corresponding to a single spin species [73]. The two edge currents are counter-propagating, meaning that there is no net current flowing around a topological-insulator sample. There is, however, a dissipationless spin current, which is ideally suited for spintronics, i.e., device design based on spin instead of electronic currents. The detection of edge states with angle-resolved photoemission spectroscopy has been the most celebrated experimental signature of topological insulators.

Part II

Correlations & topology in 2D lattices

Introduction

The preceding chapters introduced the prototypical classes of topological matter. With this necessary background in place, the central theme of this work – the behavior of correlated particles in two-dimensional lattices with topologically non-trivial content – will now be elaborated upon. The focus will be on addressing fundamental proof-of-principle questions regarding the emergence of topological states. Examples of such questions, which will be answered to a certain degree in the following chapters, are:

- Are weak or strong interactions more favorable to correlated topological states?
- Are insulators or semiconductors more suitable hosts?
- Are dispersive or flat bands more susceptible to topological order?
- Are correlated topological phases beyond the fractional quantum Hall paradigm possible in single-species many-particle systems?

Several general conclusions related to these questions can be drawn from the treatment of basic lattice models, stripped down to the bare essentials.

The discussion will proceed in order of increasing deviation from what is by now "textbook" knowledge. After introducing the relevant single-particle models and potential experimental settings in Chapter 3, the correlated states arising with the inclusion of interactions will be presented. In Chapter 4, conventional charge ordering will be reviewed, as, firstly, it naturally comes into context whenever particles repel each other strongly, and secondly, it will later be shown to either compete with or induce topological order (Chapters 5 and 7). The first instance of the latter – a phase resembling a lattice version of the FQH effect in zero net magnetic field – will be encountered in Chapter 5. Since this phase, dubbed fractional Chern insulator (FCI), is both conceptually important in its own right, as well as a building block for more complex states (like the ones that will be encountered in Chapter 7), a thorough exploration of its properties will ensue. Of particular interest will be characteristics that render FQH and FCI states distinct entities. This line of thought will be further pursued in Chapter 6, which will mark the complete departure from physics resembling that of the partially filled lowest Landau level. Finally, this departure will be most manifestly demonstrated in Chapter 7, where a paradigm of quantum states exhibiting combined topological and conventional charge order will be introduced.

The majority of the intuition necessary to understand the correlated states about to be encountered has been gained from exact diagonalization. Until

today, the only methods that can access both the energetics and the ground-state observables necessary for a conclusive characterization of the topologically ordered states studied here are exact numerical simulations. The use of such methods is favored by the fact that the states that will be encountered contain only short-range, albeit strong, correlations, and therefore finite-size effects are controllable. An implementation of exact diagonalization based on the Lanczos algorithm [78, 79] has been used to obtain all the numerical results presented in this Part. As an alternative to exact diagonalization, the density-matrix renormalization group method is recently becoming more commonly used in similar studies. However, exact diagonalization allows for the evaluation of dynamical observables in systems with periodic boundary conditions, such as the topological invariant of Section 5.3 – a task that is formidable with any other numerical method for correlated quantum many-body systems. Quantum field theory and trial wavefunctions have also been instrumental in the understanding several aspects of the fractional quantum Hall effect and there are currently attempts to repeat this success in the study of novel topologically ordered states. Even though there are noteworthy developments in these directions, most of them are only marginally related to the topics that follow and, for this reason, will not be reviewed here.

Chapter 3

Haldane-like models & Chern bands

The beauty of topological insulators lies, arguably, in the simplicity of the theory that describes their characteristic properties. It is, however, not only aesthetically pleasing, but also helpful in practice to mimic this simplicity when attempting to understand the more complicated aspects of correlated topological order. Due to its conceptual significance, its relevance to graphene, as well as the convenience afforded by the "built-in" breaking of time-reversal symmetry without an externally applied magnetic field, the Haldane model introduced in Section 2.2.1 is a common launchpad for theories of topological states. Instead of the Haldane model, however, two models with equivalent properties will be introduced below and will form the basis of the following Chapters. This choice has been made for several reasons. Firstly, the models to be introduced below are, in a sense, more elegant than the Haldane model, as they need fewer parameters and less tuning thereof, in order to exhibit the sought-after correlated topological states presented in Chapters 5, 6 and 7. They are thus the simplest framework that captures all the physics advertised in the introduction to this Part. Secondly, the existence of alternatives hints at the generality of the concepts introduced, despite geometric differences. Finally, despite the apparent minimalism, they can approximate physical systems in certain interesting settings, as will be discussed for each model individually.

Consider interacting spinless fermions that hop on a lattice Λ with two inequivalent sites per unit cell. The general form of the Hamiltonian describing such a system is

$$\hat{\mathcal{H}} := \hat{\mathcal{H}}_{\text{kin}} + \hat{\mathcal{H}}_{\text{int}} \,. \tag{3.1a}$$

For $\hat{\mathcal{H}}_{\text{kin}}$ we will use the formalism developed in Section 2.1. Two specific models shall be studied below, by specifying the functions $g_{\mu,\boldsymbol{k}}$ with $\mu = 0, 1, 2, 3$. In both cases, $\boldsymbol{g}_{\boldsymbol{k}}$ has a non-zero winding number and the upper and lower bands have Chern numbers $C = \pm 1$, respectively, for $\mu_{\text{s}} = 0$. For the models that will be presented below, a topological phase transition occurs at a finite μ_{s}, at which value the bands touch linearly, forming Dirac cones at two Fermi points in the Brillouin zone. This is in close analogy to the Haldane model. The interaction

term $\hat{\mathcal{H}}_{\text{int}}$ is the truncated Coulomb repulsion

$$\hat{\mathcal{H}}_{\text{int}} := V \sum_{\langle \boldsymbol{i},\boldsymbol{j} \rangle} \hat{n}_{\boldsymbol{i}}\, \hat{n}_{\boldsymbol{j}} + V_2 \sum_{\langle\langle \boldsymbol{i},\boldsymbol{j} \rangle\rangle} \hat{n}_{\boldsymbol{i}}\, \hat{n}_{\boldsymbol{j}} + V_3 \sum_{\langle\langle\langle \boldsymbol{i},\boldsymbol{j} \rangle\rangle\rangle} \hat{n}_{\boldsymbol{i}}\, \hat{n}_{\boldsymbol{j}}, \tag{3.1b}$$

where $V, V_2, V_3 \geq 0$ are the strengths of first, second and third nearest-neighbor repulsion, $\langle \boldsymbol{i},\boldsymbol{j} \rangle$, $\langle\langle \boldsymbol{i},\boldsymbol{j} \rangle\rangle$ and $\langle\langle\langle \boldsymbol{i},\boldsymbol{j} \rangle\rangle\rangle$ are directed first, second and third nearest-neighbor bonds, and $\hat{n}_{\boldsymbol{i}}$ is the number operator that counts how many spinless fermions occupy the lattice site at position $\boldsymbol{i}$. The second and third nearest-neighbor interactions will only be included in Chapter 7 and, until then, $V_2 = V_3 = 0$.

Of interest at several points in the following chapters will be the dependence of the properties of the encountered topological states on the amount of dispersion of the band the particles reside in. To this end, the quantity

$$M := \frac{\Delta_{\text{min}}}{W}, \tag{3.2}$$

where Δ_{min} is the minimum of the gap between the two Chern bands and W the bandwidth of the lowest band, will be used as a representative parametrization. A band characterized by a large M resembles a Landau level, in the sense that non-interacting particles live in an energy manifold that is closer to being perfectly degenerate. Interactions are then expected to lift this degeneracy in a non-trivial fashion.

In analogy to the fractional quantum Hall effect (FQHE), the minimal requirements for topological ordering in lattice models are expected to be interactions and partial filling of the topologically non-trivial manifold, i.e., the Chern band. Considering interactions, it was discovered early on in the days of the FQHE that the entire range of the Coulomb interaction is not necessary to theoretically account for the properties of FQH states. In particular, it was found that the ansatz wavefunction most successful in explaining FQHE characteristics – the Laughlin wavefunction [3] – is the exact ground state of a truncated Coulomb repulsion in the lowest Landau level [48]. Furthermore, in itinerant systems, screening effects lead to the truncation of the long-range part of the Coulomb repulsion. The use of interactions terms such as those of Equation (3.1b) is consequently justified. When searching for topological order, the simplest choice for the filling of a Chern band again follows the FQHE paradigm, even though more exotic choices may yield novel states, as will be shown in Chapter 7.

3.1 Checkerboard-lattice model

The checkerboard-lattice model of Refs. [80, 81] can be written as

$$g_{0,\boldsymbol{k}} = 4t_3 \cos k_x \cos k_y\,, \tag{3.3a}$$

$$g_{1,\boldsymbol{k}} = 4t \cos\varphi \cos\frac{k_x}{2} \cos\frac{k_y}{2}\,, \tag{3.3b}$$

$$g_{2,\boldsymbol{k}} = 4t \sin\varphi \sin\frac{k_x}{2} \sin\frac{k_y}{2}\,, \tag{3.3c}$$

$$g_{3,\boldsymbol{k}} = 2t_2(\cos k_x - \cos k_y)\,, \tag{3.3d}$$

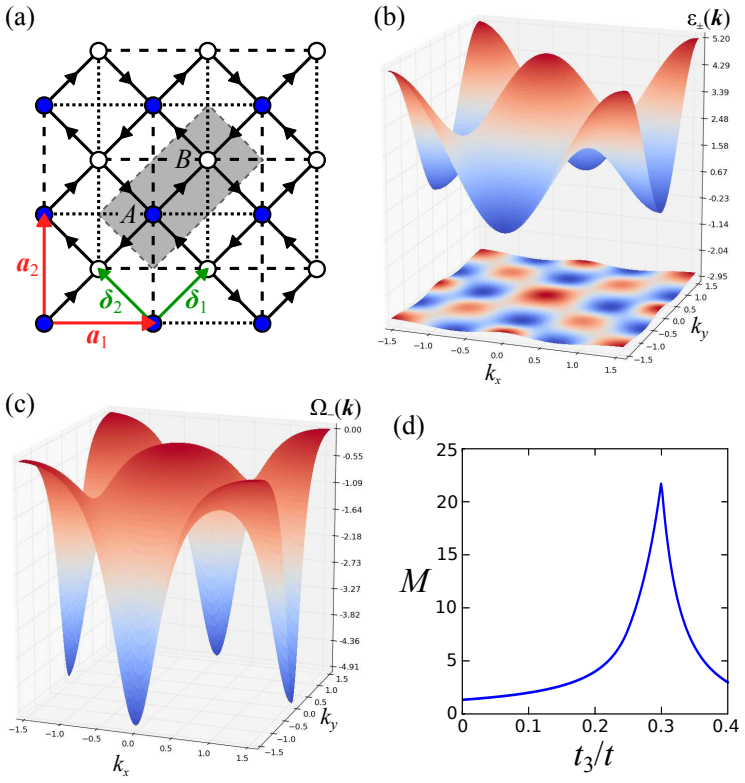

Figure 3.1: (a) Section of the checkerboard-lattice model of Equations 3.3; hopping in the direction of an arrow adds φ to the phase of the electron wave function, hopping in the opposite direction subtracts φ; dashed (dotted) lines denote second-neighbor hoppings with a negative (positive) sign; third-neighbor hoppings are uniform and are omitted for clarity. (b) Energy dispersion in the first Brillouin zone for $t_2/t = 0.4$, $\varphi = \pi/4$ and $t_3/t = 0.3$. (c) Berry curvature of the lower band in units of 2π. (d) Ratio of band gap to lower-band width as a function of t_3/t.

where t, t_2, and t_3 are first nearest-, second nearest-, and third nearest-neighbor hopping amplitudes, respectively, and $k_x := \boldsymbol{k} \cdot \boldsymbol{e}_x$ and $k_y := \boldsymbol{k} \cdot \boldsymbol{e}_y$, with $\boldsymbol{e}_x = (1, 0)$ and $\boldsymbol{e}_y = (0, 1)$ the unit vectors in x and y directions. This definition implies a square Bravais lattice with primitive lattice vectors $\boldsymbol{a}_1 = (2, 0)$ and $\boldsymbol{a}_2 = (0, 2)$ and a two-site base, with the sites of sublattices Λ_A and Λ_B offset by $(0, 0)$ and $(1, 1)$ from lattice vectors, respectively. The lattice and hoppings are depicted in Figure 3.1(a). In the following, we will fix $t_2/t = 0.4$ and $\varphi = \pi/4$. The flatness of the lower Chern band can be tuned by t_3 and is maximized at $t_3/t \approx 0.3$, as shown in Figure 3.1(c). The energy dispersion in the limit of flat lower band is shown in Figure 3.1(b). It should be noted that t_3, or, more generally, $g_{0,\boldsymbol{k}}$, does not affect the Berry curvature. The latter is shown in Figure 3.1(c). A topological phase transition occurs at $\mu_s/t = 2$ between a Chern insulator ($\mu_s/t < 2$) and a trivial insulator ($\mu_s/t > 2$). At the critical point, two inequivalent Dirac cones appear at two Fermi points, in full analogy with the Haldane model.

The checkerboard-lattice model defined above was first devised, in a different gauge, to yield chiral spin-liquid states, which arise due to the inherent frustration caused by competing nearest- and second nearest-neighbor hoppings, and to investigate the connection between chiral spin textures and superconductivity [82]. It was in this context that the name "π-flux model" arose, which is nowadays often used to designate Equations (3.3). It was subsequently employed in theories of unconventional charge ordering, which are thought to be related to the pseudogap observed in cuprate superconductors [83, 84]. Indeed, some of the usually proposed order parameters for this regime are topologically non-trivial and bond currents such as those in Figure 3.1(a) are thought to account for the unusually large Nernst signals in these materials [85–87]. Similar anomalous thermoelectric response has been encountered in heavy-fermion materials with a layered structure similar to that of the cuprates [88, 89], suggesting that a similar modeling may be applicable. Finally, the compound $TbMnO_3$ has been recently proposed as a candidate for the realization of a quantum anomalous Hall effect, based on the effective formation of the checkerboard flux pattern of Figure 3.1 [90].

3.2 Triangular-lattice model

The triangular-lattice model of Refs. [49, 68] can be written as

$$g_{0,\boldsymbol{k}} = 2t_3 \sum_{j=1}^{3} \cos(2\boldsymbol{k}\cdot\boldsymbol{\delta}_j)\,, \tag{3.4a}$$

$$g_{i,\boldsymbol{k}} = 2t\cos(\boldsymbol{k}\cdot\boldsymbol{\delta}_i), \qquad i=1,2,3, \tag{3.4b}$$

where $\boldsymbol{\delta}_1 = (1/2, \sqrt{3}/2)$, $\boldsymbol{\delta}_2 = (1/2, -\sqrt{3}/2)$, and $\boldsymbol{\delta}_3 = -(\boldsymbol{\delta}_1 + \boldsymbol{\delta}_2)$ are the primitive translation vectors of the regular triangular lattice. In this definition, the actual translation vectors of the model can be chosen as $\boldsymbol{a}_1 = \boldsymbol{\delta}_1 + \boldsymbol{\delta}_2$ and $\boldsymbol{a}_2 = \boldsymbol{\delta}_1 - \boldsymbol{\delta}_2$, meaning that the corresponding Bravais lattice is actually rectangular. The sites of sublattices A and B are offset from lattice vectors by $(0,0)$ and $(1/2, \sqrt{3}/2)$, respectively. The first nearest-neighbor and third nearest-neighbor hopping amplitudes are t and t_3, respectively. The lattice and hoppings are depicted in Figure 3.2(a). One may notice the absence of a second nearest-neighbor hopping in this model. The reason for this omission is the cancellation of such hopping processes in the three-orbital model discussed in Section 2.2.2, which is the main motivation behind the model discussed here [49, 67, 68]. Furthermore, third nearest-neighbor hopping preserves sublattice indices and is therefore included in $g_{0,\boldsymbol{k}}$, thus making the triangular-lattice model fully analogous to Haldane and π-flux models. The third nearest-neighbor hopping amplitude t_3 can be used to tune the dispersion of the lower Chern band, with the flattest bands achieved for $t_3/t \approx 0.2$, as can be seen in Figure 3.2(d). The energy branches are depicted in Figure 3.1(b) for $t_3/t = 0.2$. A topological quantum phase transition from the Chern insulator to a trivial insulator occurs again at $\mu_s/t = 2$. The Berry curvature of the lower band in the non-trivial regime is plotted in Figure 3.2(c).

The triangular-lattice model of Equations (3.4) is relevant in the context of the anomalous quantum Hall effect in itinerant magnets, as discussed in

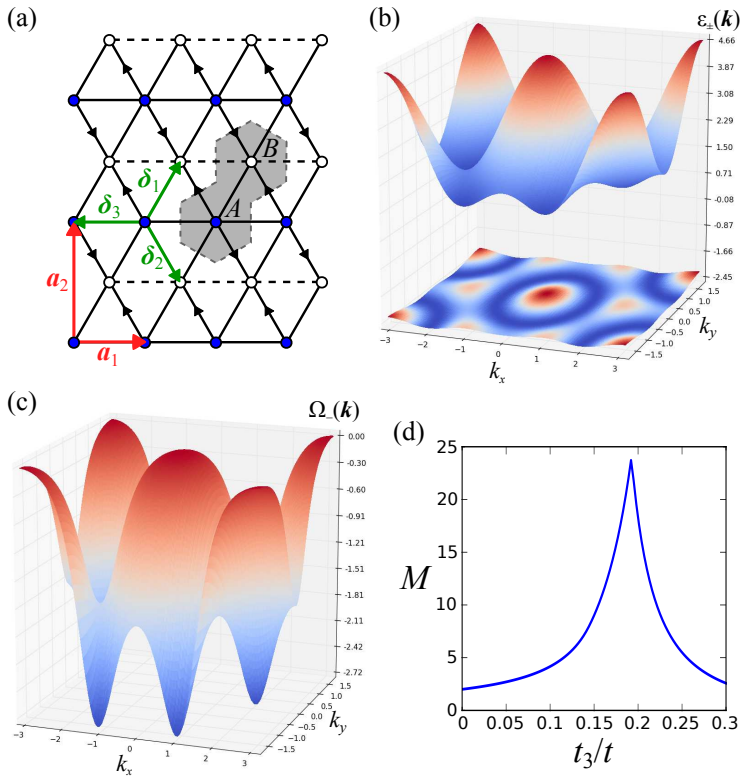

Figure 3.2: (a) Section of the triangular-lattice model of Equations 3.4; hopping in the direction of the arrows adds $\pi/2$ to the phase electron wave function, hopping in the opposite direction subtracts $\pi/2$, while dashed lines denote nearest-neighbor hoppings with a negative sign; third-neighbor hoppings are uniform and are omitted for clarity. (b) Energy dispersion in the first Brillouin zone for $t_3/t = 0.2$. (c) Berry curvature of the lower band in units of 2π. (d) Ratio of band gap to lower-band width as a function of t_3/t.

Section 2.2.1. There, the fluxes in the hoppings arise due to Berry phases acquired by itinerant electrons moving in a magnetic background with finite scalar spin chirality [56]. Potentially relevant physical systems are Mn monolayers on Cu(111) surfaces [65], the nuclear spin ground state of a two-dimensional ^{3}He system [66], $Na_{0.5}CoO_2$ [91], $PdCrO_2$ [63], as well as the scenario of transition-metal oxides of the form ABO_2 [49, 67, 68], which was discussed in Section 2.2.2.

It should be noted at this point that several other noteworthy – yet more complicated – models can be found in the literature [51, 92, 93]. Of particular interest are those associated with proposals for realization. Optical lattices [94], strained or irradiated graphene [95, 96], oxide heterostructures [97] and magnonics [98] have been suggested as potential platforms for the realization of Chern bands. Even though some of these proposals are close to experimental realization, the regime of fractionally filled Chern bands has not yet been explored.

Chapter 4

Interaction-driven charge order in flux models

Charge ordering is a phenomenon of great theoretical and experimental interest [99]. Evidence of charge-density wave (CDW) order has been reported for several quasi two-dimensional materials of significant technological applicability, such as the high critical-temperature superconductors $La_{2-x}Ba_xCuO_4$ [100] and (Y,Nd)$Ba_2Cu_3O_{6+x}$ [101, 102], as well as for several molecular organosulphuric compounds [103] and metal dichalcogenides [104]. A particularly tantalizing feature of CDW states is that they can arise at room temperature [104]. In most quasi one-dimensional and many quasi two-dimensional materials, charge ordering is driven by electron-phonon coupling and nesting of the Fermi surface that arises if one considers only the single-particle kinetics. In quasi two-dimensional molecular systems, on the other hand, charge-density waves form mostly due to electron-electron interaction, while electron-phonon coupling plays only a secondary role [103]. Anisotropy effects are often also the origin of observable properties of CDWs in functional materials [105]. The driving force behind the CDWs discussed in this chapter, however, will be a moderate to strong isotropic repulsion between particles.

The competition between CDW states and topological ordering in lattice models of spinless fermions will be investigated in the following Chapter. Whenever charge-density modulations come into play in the formation of a quantum state, observable properties depend crucially on whether the charge patterning is commensurate with the underlying lattice. In Section 4.1, the commensuration conditions for the emergence of charge patterns will be discussed. The discussion here will be focused on the triangular-lattice model of Section 3.2, as its phase diagram as a function of filling and interaction strength has so far proven to be quite rich. Having thus obtained the main qualitative characteristics from general symmetry arguments, we will verify them by comparison to numerical calculations, which will be presented in Section 4.2. These observations will be useful in identifying commensurate and incommensurate charge-density modulations in Section 5.5 and composite ordering in Chapter 7.

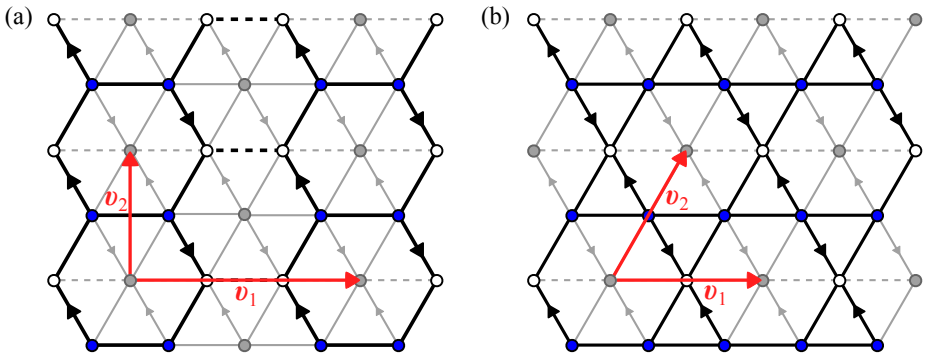

Figure 4.1: Charge-density patterns (a) for large V at $\rho = 1/3$, and (b) for large V and V_2 at $\rho = 1/4$. Grey sites denote high particle density.

4.1 Repulsion and commensurability

The emergence of repulsion-driven charge order depends crucially on the geometry of the system under consideration. This is easily illustrated through an example. Consider the triangular-lattice model of Equations (3.1) and (3.4) on a finite cluster, populated by an average particle density $\rho = 1/3$ particles per site. All kinetic parameters are set to zero and the nearest-neighbor repulsion strength V has a finite value. The states that do not pay an energy penalty proportional to V are configurations where particles occupy only next-nearest neighboring sites, such as the one shown in Figure 4.1(a). Whenever the number of sites in the cluster is a multiple of 3, then the patterns of particles sitting at next-nearest neighboring sites is commensurate with the lattice, i.e., the charge pattern can form a regular Bravais superlattice. It is readily seen that, if commensurability is respected, there can only be three such configurations, regardless of the size of the cluster. In contrast, it can be seen that, for the same density and interaction range, the number of compatible low-energy configurations on the square lattice increases with the size of the cluster. Similar arguments show that, apart from the lattice coordination, particle density and interaction range need to be matching, in order to obtain a commensurate charge-density wave. Cluster geometry also plays a significant role in finite clusters, as will be seen in Section 5.5. In this Section, however, two examples, for which all commensurability conditions are met, will be demonstrated.

The formation of the charge pattern shown in Figure 4.1(a) implies an enlarged unit cell and new translation vectors $\boldsymbol{v}_1$ and $\boldsymbol{v}_2$. Since $\boldsymbol{v}_1 = 3\boldsymbol{a}_1$ and $\boldsymbol{v}_1 = \boldsymbol{a}_2$, where $\boldsymbol{a}_1$ and $\boldsymbol{a}_2$ are the translation vectors of the original lattice, the area of the unit cell is tripled. This means that one gets three copies of the reduced Brillouin zone within the original Brillouin zone. The basis configurations of the charge pattern shall be denoted by $|100\rangle$, $|010\rangle$ and $|001\rangle$. The general CDW state can therefore be defined, up to a phase factor, as

$$|\psi_{\mathrm{CDW}}\rangle := |100\rangle + e^{i\beta}\,|010\rangle + e^{i\gamma}\,|100\rangle\ . \tag{4.1}$$

The phases β and γ can be obtained by exploiting particle indistinguishability and translational symmetry. To this end, one may define the many-body

translation operator

$$\hat{\mathcal{T}}_{\boldsymbol{R}} := \prod_{i=1}^{N} \hat{c}^{\dagger}_{\boldsymbol{i}+\boldsymbol{R}} \hat{c}_{\boldsymbol{i}} \,, \tag{4.2}$$

which translates a many body state by a lattice vector $\boldsymbol{R}$. Imposing periodic boundary conditions, it can be seen that the action of $\hat{\mathcal{T}}_{\boldsymbol{a}_1}$ on the basis configurations yields

$$\hat{\mathcal{T}}_{\boldsymbol{a}_1} |100\rangle = |010\rangle \tag{4.3}$$

$$\hat{\mathcal{T}}_{\boldsymbol{a}_1} |010\rangle = |001\rangle \tag{4.4}$$

$$\hat{\mathcal{T}}_{\boldsymbol{a}_1} |001\rangle = |100\rangle \ . \tag{4.5}$$

On the other hand, since the system under consideration is translation symmetric,

$$|100\rangle = e^{-i\boldsymbol{K}\cdot\boldsymbol{a}_1} |010\rangle \tag{4.6}$$

$$|010\rangle = e^{-i\boldsymbol{K}\cdot\boldsymbol{a}_1} |001\rangle \tag{4.7}$$

$$|001\rangle = e^{-i\boldsymbol{K}\cdot\boldsymbol{a}_1} |100\rangle \ , \tag{4.8}$$

where $\boldsymbol{K}$ is the total crystal momentum. Replacing above, one obtains $\beta = -\gamma = \boldsymbol{K}\cdot\boldsymbol{a}_1$. Translations by $\boldsymbol{a}_2$ lead to the same configurations and do not offer any extra information.

Periodic boundary conditions imply that not all values of $\boldsymbol{K}$ are allowed. A translation by $\boldsymbol{v}_1$ or $\boldsymbol{v}_2$ leads back to the same state. This can be written as $\hat{\mathcal{T}}_{\boldsymbol{v}_i} |\psi_{\mathrm{CDW}}\rangle = |\psi_{\mathrm{CDW}}\rangle$ for $i = 1, 2$. However, the Bloch theorem implies that the translated state should acquire a momentum-dependent phase factor $e^{i\boldsymbol{K}\cdot\boldsymbol{v}_i}$. To reconcile this, the relation $\boldsymbol{K}\cdot\boldsymbol{v}_i = 2\pi n_i$, with n_i integers and $i = 1, 2$, must hold. For the specific case of Figure 4.1(a), the solutions within unit cell of the dual lattice $[0, 2\pi) \times [0, 2\pi/\sqrt{3})$ are $(2\pi n/3, 0)$ for $n = 0, 1, 2$. The equivalent points in the first Brillouin zone $(-\pi, \pi] \times (-\pi/\sqrt{3}, \pi/\sqrt{3}]$ are $\boldsymbol{K}_n = (2\pi n/3, 0)$ for $n = -1, 0, 1$. The wavevectors $\boldsymbol{K}_n$ are called ordering vectors. Gapless systems are particularly prone to the development of CDW states when the ordering vectors of the charge pattern nest large parts of the Fermi surface. This is the weak-coupling scenario, pertinent to several CDW materials. In what follows, the driving force for the development of CDW order will be a strong particle-particle repulsion. The CDW will emerge as a strong-coupling instability, which is affected only mildly by kinetics (more on this in Section 5.5).

The procedure outlined above can be followed to obtain the ordering vectors for the charge pattern of Figure 4.1(b), which occurs at $\rho = 1/4$. It is seen that, in the classical limit, a nearest-neighbor repulsion allows for a macroscopic degeneracy at this filling. The charge-ordered state of Figure 4.1(b) is obtained if a second-neighbor repulsion is included. Formation of this CDW means that the unit cell doubles in area and therefore the reduced Brillouin zone will fit twice in the original Brillouin zone. The ordering vectors are two: $\boldsymbol{K}_1 = (0, 0)$ and $\boldsymbol{K}_2 = (\pi, \pi/\sqrt{3})$. The low-energy configurations are now four and can be denoted as

$$\begin{pmatrix} 1 & 0 \\ 0 & 0 \end{pmatrix}, \begin{pmatrix} 0 & 1 \\ 0 & 0 \end{pmatrix}, \begin{pmatrix} 0 & 0 \\ 1 & 0 \end{pmatrix} \text{ and } \begin{pmatrix} 0 & 0 \\ 0 & 1 \end{pmatrix} .$$

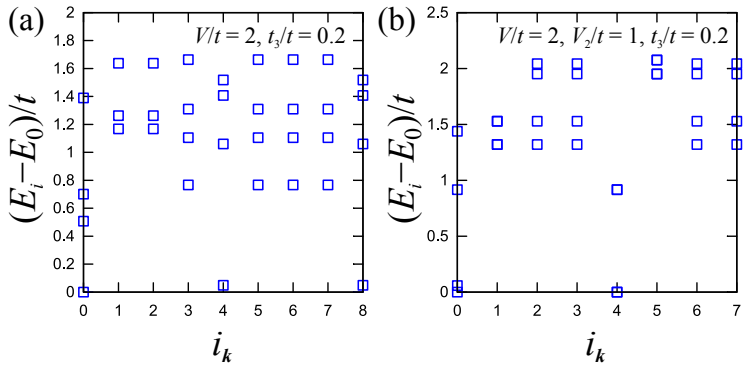

Figure 4.2: Eigenvalue spectra of the triangular-lattice model (a) for a 3×3 unit-cell cluster at $\rho = 1/3$ with $V/t = 2$ and $t_3/t = 0.2$, and (b) for a 4×2 unit-cell cluster at $\rho = 1/4$ with $V/t = 2$, $V_2/t = 1$ and $t_3/t = 0.2$. In (b), the ground state at $i_{\boldsymbol{k}} = 4$ is doubly degenerate.

Acting with the translation operators of the original lattice vectors yields

$$\hat{\mathcal{T}}_{\boldsymbol{a}_1} \begin{pmatrix} 1 & 0 \\ 0 & 0 \end{pmatrix} = \hat{\mathcal{T}}_{\boldsymbol{a}_2} \begin{pmatrix} 1 & 0 \\ 0 & 0 \end{pmatrix} = \begin{pmatrix} 0 & 1 \\ 0 & 0 \end{pmatrix} \tag{4.9}$$

$$\hat{\mathcal{T}}_{\boldsymbol{a}_1} \begin{pmatrix} 0 & 0 \\ 1 & 0 \end{pmatrix} = \hat{\mathcal{T}}_{\boldsymbol{a}_2} \begin{pmatrix} 0 & 0 \\ 1 & 0 \end{pmatrix} = \begin{pmatrix} 0 & 0 \\ 0 & 1 \end{pmatrix} . \tag{4.10}$$

In this case, translations by lattice vectors are not enough to cycle through all the configurations[1]. This implies that the momentum quantum number will not be enough to uniquely resolve all CDW states. This will lead, as will be seen in the next section, to additional degeneracies in the many-body energy spectrum.

4.2 Signatures of charge ordering

For the general problem of itinerant and interacting particles, CDW order can be detected with numerics. Even though finite hopping amplitudes introduce quantum fluctuations around the configurations of Figure 4.1, the general conclusions reached in the previous Section are still expected to hold, whenever interaction strengths are large enough to induce a CDW state. The folding of the Brillouin zone caused by the formation of the CDW and the multiplicity of ordering vectors suggest that the ground state of a CDW on a finite system should be quasi degenerate in the unfolded Brillouin zone. If translation symmetry is used in the numerical evaluation of the many-body energy spectrum, then the ground states are found in the momentum sectors corresponding to the ordering vectors. This degeneracy should not be confused with the degeneracy of topological origin, which was discussed in Section 1.2. An intuitive way to see this is to notice that the expected degeneracies for CDW patterns do not depend on the boundary conditions. In fact, the degeneracy would be exactly the same, even if the boundaries of the lattice were opened in either one or two

[1]One can reach all the configurations by acting on one of them with the translation operators corresponding to one of the lattice vectors $\boldsymbol{a}_i$ and to one of the nearest-neighbors $\boldsymbol{\delta}_j$ with $\boldsymbol{a}_i \neq \pm\boldsymbol{\delta}_j$.

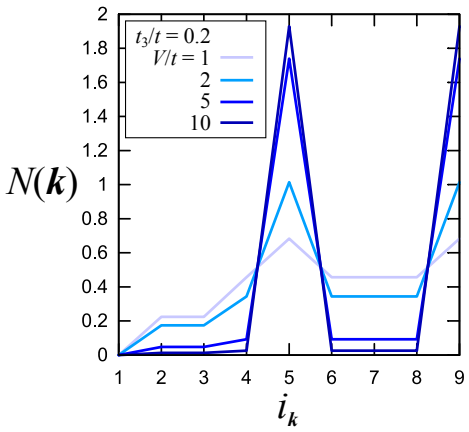

Figure 4.3: Static charge-structure factor $N(\boldsymbol{k})$ for the triangular-lattice model on a 3×3 unit-cell cluster at $\rho = 1/3$ with $t_3/t = 0.2$.

directions, as can be seen for the patterns in Figure 4.1. On the other hand, changes in the geometry of the system may destroy the CDW order, and therefore the ground-state degeneracy. The implication of these simple observations is that the degeneracy of CDW states is not of topological origin.

Before proceeding, the formating of the energy spectra obtained via exact diagonalization shall be explained, as such spectra will be frequently encountered in the following chapters. For a finite real-space lattice, the Brillouin zone of the dual lattice will contain a finite number of discrete momenta. A convenient single-index parametrization of these momenta is the following: for a real-space lattice with $L = L_1 \times L_2$ sites, where L_1 and L_2 are the numbers of sites along the lattice primitive vectors $\boldsymbol{a}_1$ and $\boldsymbol{a}_2$, respectively, there will be L sites in the unit cell of the dual lattice, with L_1 and L_2 sites along the directions of dual-lattice primitive vectors $\boldsymbol{b}_1$ and $\boldsymbol{b}_2$, respectively. The dual-lattice vectors then form the set

$$\Xi := \left\{ \frac{i_{k_1}}{L_1}\boldsymbol{b}_1 + \frac{i_{k_2}}{L_2}\boldsymbol{b}_2 \,:\, i_{k_1} = 0, \ldots, L_1 - 1\,,\, i_{k_2} = 0, \ldots, L_2 - 1 \right\}. \tag{4.11a}$$

The momentum-sector index $i_{\boldsymbol{k}}$ is defined as

$$i_{\boldsymbol{k}} := i_{k_1} L_2 + i_{k_2}. \tag{4.11b}$$

This corresponds to spanning the dual lattice along $\boldsymbol{b}_2$ once for each lattice site along $\boldsymbol{b}_1$.

Returning to the CDWs, the degeneracy of the ground state is shown in Figure 4.2 for the two CDWs of Figure 4.1, where the indexing scheme of Equations (4.11) has been employed. The degeneracy in the ground state is the one expected from the symmetry arguments of the previous section. Note that the momentum quantum number is not sufficient to distinguish between all states in the CDW manifold in the case of the pattern seen in Figure 4.1(b), as was already expected from the symmetry arguments of the preceding section.

The formation of charge patterns can also be visualized experimentally using electron microscopy or x-ray diffraction. In these measurements, electrons or

photons scatter elastically off the sample and are subsequently detected. The elastic scattering amplitudes are proportional to the static charge-structure factor, which is a direct measure of the concentration of charges in the sample. A momentum-resolved measurement will yield an intensity peaked at the ordering wavevectors. Theoretically, the static charge-structure factor is defined as

$$N(\boldsymbol{k}) = \left| \sum_{\boldsymbol{i} \in \Lambda} \mathrm{e}^{\mathrm{i}\boldsymbol{k}\cdot\boldsymbol{i}} (\hat{n}_{\boldsymbol{i}} - \rho) |n\rangle \right|^2 , \tag{4.12}$$

where $|n\rangle$ is a vector of the ground-state manifold and $\hat{n}_{\boldsymbol{i}}$ is the particle-density operator acting at lattice site $\boldsymbol{i}$. In the presence of charge order, the static charge-structure factor is sharply peaked in the momentum sectors corresponding to the ordering vectors of the CDW. This is precisely what is seen in Figure 4.3 for the case of the charge pattern shown in Figure 4.1. The indices $i_{\boldsymbol{k}}$ correspond to the ordering vectors worked out in the preceding section.

Even though, as mentioned in the beginning of this Section, kinetic terms do not alter the type or the signs of commensurate interaction-driven ordering, their inclusion leads to a competition between two energy scales. When interactions are significantly stronger than kinetic terms, this competition does not affect the properties of the ground state. If, however, the energy scales are comparable, a gain in kinetic energy may overcome a repulsion penalty. This interplay may shift phase boundaries between competing states, as will be shown in the next Chapter for the case of the commensurate $\rho = 1/3$ CDW state. The situation becomes even more interesting whenever the charge order is incommensurate or frustrated. In these cases, it is not a priori known how severely the ground state may be affected by the inclusion of kinetics. One intriguing possibility for the resolution of the frustration by kinetics, which leads to a novel correlated topological state, will be explored in Chapter 7.

Chapter 5

Fractional Chern Insulators

As discussed in Chapter 1, the interpretation of the Hall conductivity as a topological invariant associated to an energy band provided the first in a series of indications, which suggested that solids may actually host states with topologically non-trivial content. This realization afforded an alternative route to quantum Hall liquids, namely, via tightly bound electrons moving in a magnetic texture. The simplest such magnetic texture is a uniform magnetic field perpendicular to the plane of the system. For non-interacting, tightly bound electrons, this gives rise to an integer quantum-Hall (IQH) state and leads to Hofstadter's fractal energy spectrum [44]. As shown in Section 2.2.1, one can obtain IQH states even without an applied magnetic field. The half-filled Haldane model, with complex hoppings that break time-reversal invariance, constitutes the first Chern insulator (CI), in which the total magnetic field through the unit cell averages to zero. Furthermore, the discourse in Section 2.2 indicated physical mechanisms that can lead to complex hoppings with the necessary properties. One possibility arises through the coupling of itinerant electrons to localized magnetic moments [60]. For example, the Kondo-lattice model on the triangular lattice supports a non-trivial magnetic texture, which induces an integer-quantized Hall conductivity of the itinerant electrons [56].

A considerable body of recent research revolves around the question whether a lattice counterpart of the FQHE can be observed when topologically non-trivial bands, called Chern bands, are fractionally filled and electrons are interacting. Initially, Chern bands were commonly assumed to be perfectly flat and isolated, in order to emulate the prototypical FQH setting, where interactions are added to a massively degenerate manifold of single-particle states. Several numerical studies using exact diagonalization techniques have convincingly established the existence of Laughlin-series states in an number of different models on various lattices [80, 81, 106–110]. These systems have since been called fractional Chern insulators (FCI). Very recent work has reported FCI states beyond Laughlin fractions [68, 111, 112]. In addition to reproducing the known FQHE on a lattice and potentially at higher temperatures, CIs also offer the intriguing possibility of a Chern number higher than one, a departure from the analogy with LLs. Recent studies have explored this direction by constructing models that have higher Chern numbers and studying possible FCI states [113–118]. From the analytical side the problem of FCI states has been approached by a careful study of emergent translational symmetries [119] and many-body trial

wave functions [120–122]. Others have examined the algebraic properties of the density operators projected onto one Chern band and made a comparison with the Girvin-MacDonald-Platzman algebra that is satisfied by the lowest LL density operators in the continuum FQHE [119, 123–125].

The states studied in this Chapter are inspired by the multi-orbital scenario presented in Section 2.2.2. Previous work has established on a mean-field level that a magnetically ordered CI with a very flat single-particle band emerges, which can be effectively modeled by the triangular-lattice model of Section 3.2 [49, 68]. This effective picture has been proven to be robust when the single-particle band is half filled, but is also expected to hold for finite doping. It is therefore reasonable to also explore fractional fillings, as well as interactions beyond on-site repulsion, in this regime.

The following Sections will provide extensive numerical evidence, based on both spectral features, to be presented in Sections 5.1 and 5.2, and eigenstate properties, i.e., the many-body Berry curvature and Hall conductivity discussed in Section 1.1.2, for the existence of FCI states in the effective model of Section 3.2. The robustness of FCI states against disorder originating from single-bond defects in the magnetic ordering, which will always occur in realistic situations, is also investigated in Section 5.4. Another very relevant issue in the context of FCI states is their competition with other phases [112, 118], e.g. symmetry-broken states such as a charge-density wave (CDW). The model considered in this work allows for a careful study of the competition between FCI and CDW states in the presence of finite dispersion and interactions, which will be presented in Section 5.5. Even though the discussion is tailored to the triangular-lattice model of Section 3.2, this Chapter contains an overview of the most important numerical signatures of FCI states in general. For similar results on other models, such as the checkerboard-lattice model of Section 3.1, the reader will be referred to the respective works in the literature.

A large part of this Chapter has been previously published in Ref. [49] with J. Venderbos and M. Daghofer.

5.1 Eigenvalues and flux insertion

The universal spectral properties of Hamiltonians with FCI groundstates are analogous to those of FQH states [20, 23]. FCI ground states on the torus are gapped, with a topological degeneracy equal to the denominator of the filling fraction ν of the partially filled Chern band. In finite systems, the ground-state degeneracy of FCI states is not exact. Due to this splitting, FCI ground-state eigenvalues exhibit spectral flow, meaning that they exchange values upon insertion of one flux quantum through one of the handles of the torus, in full analogy to FQH states, as discussed in Section 1.2. Flux insertion is defined as the transformation

$$t_{\boldsymbol{ij}} \to t_{\boldsymbol{ij}}\, e^{\mathrm{i}\left(\varphi_1 \frac{j_1-i_1}{L_1}+\varphi_2 \frac{j_2-i_2}{L_2}\right)} \tag{5.1}$$

for the hopping from the site at position $\boldsymbol{i} \equiv (i_1, i_2)$ to the site at position $\boldsymbol{j} \equiv (j_1, j_2)$, where the components of the position vectors, as well as those of the flux vector $\boldsymbol{\varphi} \equiv (\varphi_1, \varphi_2)$, are along the directions of the corresponding primitive lattice vectors, and i is the imaginary unit. Note that the flux phase

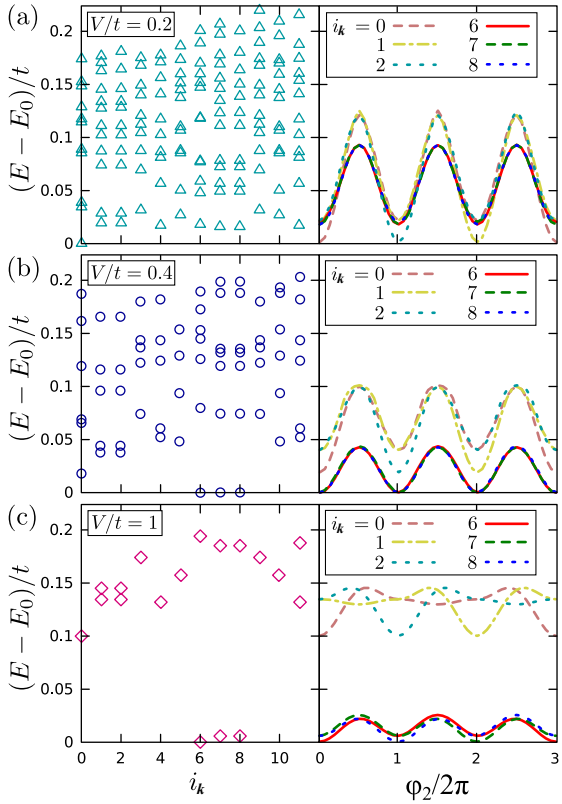

Figure 5.1: Eigenvalue spectrum and evolution of selected levels under flux insertion for different values of V/t. In all panels $t_3/t = 0.2$.

has been distributed equally to all hoppings, therefore dividing the fluxes φ_1 and φ_2 by the corresponding lattice extents L_1 and L_2, in order to maintain the translational invariance of the lattice. As this redistribution can be achieved via a local gauge transformation, which leaves the physics unchanged, this choice is equivalent to twisting the boundary conditions.

The features described above are illustrated, as a function of V/t, in Figure 5.1 for $\nu = 1/3$, where $\nu \equiv \rho/2$ designates the filling of the lower Chern band. Unless explicitly designated otherwise, all numerical results presented in this Chapter are obtained from a 4×6-site cluster with periodic boundary conditions. The three quasi-degenerate ground states emerge from the continuum as the interaction strength is increased. The transition to the FCI phase is determined by the condition that ground states remain gapped upon flux insertion, not only in their own momentum sector, but also across momentum sectors. The reason is that the presence of impurities would mix the momentum sectors and therefore close the gap if the quasi-degenerate FCI-state levels cross excited-state levels. At the same time, ground-state levels that remain gapped upon flux insertion along one direction may cross excited-state levels upon flux insertion along another direction. Despite these stringent conditions, FCI states remain gapped for a range of both V and M. Insertion of one flux quantum indeed leads from one ground-state eigenvalue to another. It can also

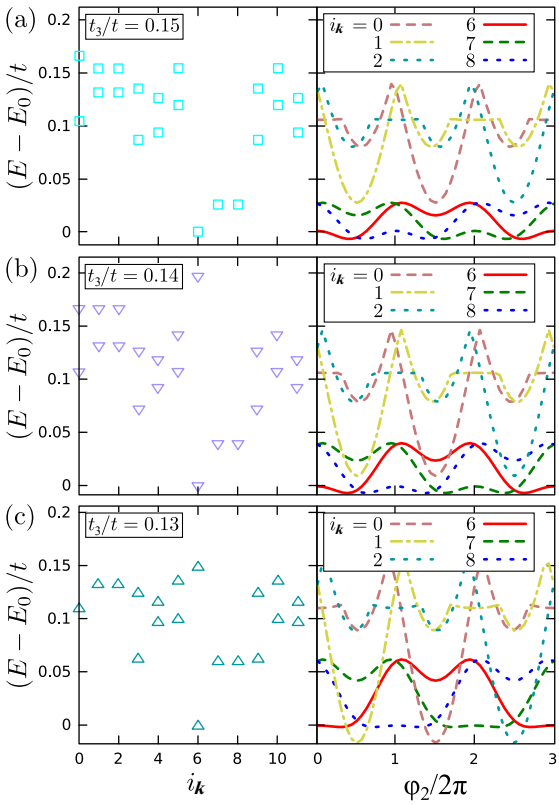

Figure 5.2: (Color online) Eigenvalue spectrum and evolution of selected levels under flux insertion for different values of t_3/t. In all panels $V/t = 1$.

be seen that spectral flow is a general property of the eigenvalue spectrum. The $\nu = 2/3$ ground states behave in a similar fashion. As seen in Figure 5.1, interaction mostly changes the energy differences between groups of three quasi-degenerate eigenstates, which flow into each other upon flux insertion, and has less impact on the energy splitting within each manifold.

When tuning the transition via increasing the band dispersion, the situation is somewhat different, see Figure 5.2. For $M \approx 10$, the FCI ground state is destroyed by increasing the split between quasi-degenerate levels, permitting a higher-energy states to mix with the FCI-state manifold for some flux values. The splitting between ground states in the traditional FQHE case is due to quasiparticle-quasihole excitations propagating around the torus and therefore depends mainly on system size, becoming zero in the thermodynamic limit [20]. In the finite tight-binding lattice systems discussed here, the splitting is affected significantly by the residual kinetic energy of the partially filled band, as can be seen in Figure 5.2.

Despite level rearrangements or increasing spread between eigenvalues, FCI states remain topologically conjugate upon varying the band flatness or the interaction strength. A factor that can split this conjugacy is disorder, as will be shown in Section 5.4. A more careful analysis, based both on eigenenergy as well as on eigenstate properties, is necessary to uniquely determine a gapped

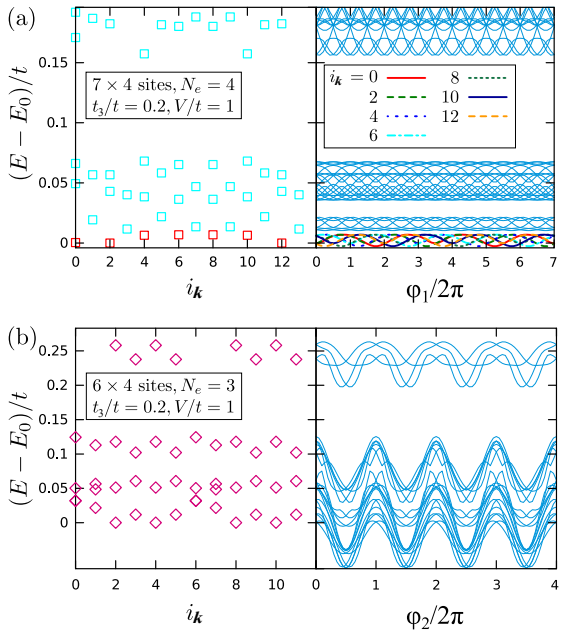

Figure 5.3: Eigenenergy spectrum and spectral flow for FCI state with quasi-holes introduced (a) by enlarging the system or (b) by removing particles. The numbers of levels below the legends are (a) 35 and (b) 40 respectively, in agreement with the counting rule of Equation (1.41). In the 7×2-unit cell system, the filling fraction is $\nu = 2/7$. There are seven quasi-degenerate ground states (marked in red), which are slightly separated from the rest of the states in the low-energy sector and exhibit spectral flow (shown in different colors). The Hall conductivity contributed by each state is $-2/7$ in units of e^2/h within the numerical error margin.

ground state for a given parameter set. This is the purpose of Section 5.3. Before investigating eigenstates, however, the next section is going to expose another aspect of eigenenergies, fractional statistics. It should be mentioned that similar spectral flow has been observed in the checkerboard-lattice model of Section 3.1 [80, 108, 109].

5.2 Fractional statistics

The concept of generalized Pauli principles introduced in Section 1.2, according to which states with clustered fractional-statistics quasiparticles are energetically penalized, has served as a tool to indicate fractional statistics in FQH states [35–37]. Numerical studies of the π-flux model first demonstrated heuristically [109] and later on substantiated theoretically [119] that same logic holds for FCI states. For the $\nu = 1/3$ FCI state, the number of quasihole-state levels in a well separated, low-energy Fock space is equal to the number of (1,3)-admissible partitions of the momentum sectors on the torus. The dimension of the low-energy quasihole Fock space is precisely D_N^{torus} of Equation (1.41) for $q = 3$. The individual states per momentum sector can also be accounted for,

due to an emergent translational symmetry (see Ref. [119] for details). In this section, it is demonstrated that quasihole states of the triangular-lattice model obey the same state-counting arguments.

Quasiholes can be introduced in a FCI by either removing electrons or increasing the system size. An example of both cases is presented in Figure 5.3. The counting rule is verified in both cases and has also been verified for $\nu = 1/5$ in this model. Apart from the agreement to the counting rule, one can also notice the emergence of a "daughter" FCI state within the gapped low-energy sector. Even though in the present context this is mainly a peculiarity of the small system sizes, it can nevertheless be viewed as an example of the formation of a FCI state among the quasihole states of a "parent" FCI state. FCI states thus seem to conform to the hierarchy picture of FQH states [29]. Taking this observation one step further, it can be seen that the spectrum looks qualitatively different under flux insertion in the two cases presented in Figure 5.3, namely, the eigenvalue spectrum in the case where the filling is $\nu = 1/4$ looks more like that of the non-interacting system with levels crossing upon flux insertion, whereas at $\nu = 2/7$ levels come in small groups, which remain separated under flux insertion (compare to Figure 5.1). This observation can be compared to the composite fermion theory of the FQHE [4], according to which the state of a FQH system at filling fractions with even denominators can be effectively described by free fermions with flux tubes attached to them. This composite-fermion view of the FCI hierarchy of states has also been supported by recent numerical calculations [112]. These two different facets of the same model can serve as an example of the compatibility between the hierarchy and composite-fermion pictures of the FQHE in an unconventional FQH system.

5.3 Topological invariant

The most unambiguous characteristic of a FCI state is its Hall conductivity, which serves as the relevant topological invariant. The ground-state Hall conductivity of a FCI at filling $\nu = p/q$ should be exactly ν, in units of e^2/h. The Hall conductivity σ of a gapped, degenerate state can be efficiently calculated using the Kubo formula of Equation (1.37), where L_1 and L_2 are now the extents of the lattice in unit cells along directions $\boldsymbol{a}_1$ and $\boldsymbol{a}_2$, respectively, and $\mathcal{H}_N$ is the interacting lattice Hamiltonian of Equations (3.1) and (3.4). This approach to the characterization of correlated states of spinless fermions is particularly powerful, especially when used in conjunction with the choice of not projecting the Hamiltonian to the partially filled band, as it can also be evaluated for states in which strong interactions mix the bands, or even cause charge ordering. This advantage will be fully exploited in Chapters 6 and 7.

In Figure 5.4, the many-body Berry curvature for a specific state of the triangular-lattice model, which develops into one of the FCI ground states, is shown. It is seen that its smoothness varies as this state emerges from the excited state continuum. Its period extends over q flux quanta in one direction and one flux quantum in the other, remains unchanged for all values of V and is the same for all states in the ground-state manifold. The Berry curvature of the other two ground states is the same function, but translated by one and two flux quanta in the φ_2 direction, respectively. Even when the many-body Berry curvature of a FCI state is strongly varying, the Hall conductivity obtained by

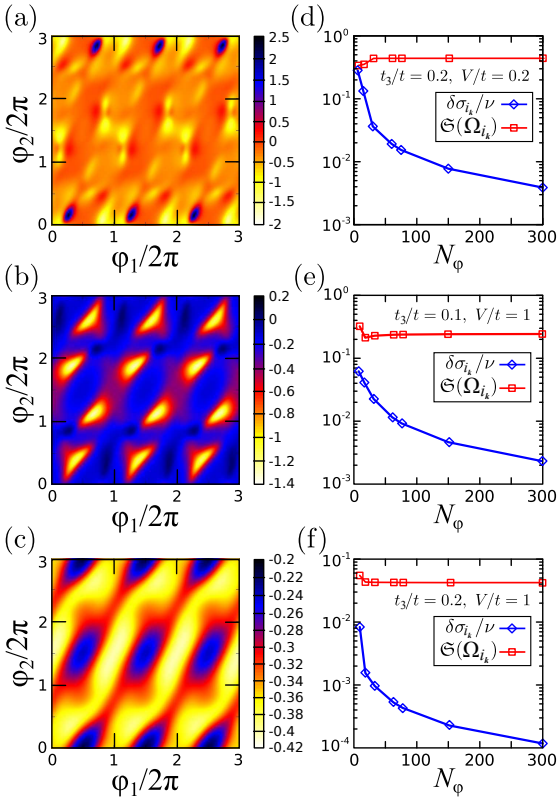

Figure 5.4: (a-c) Berry curvatures $\Omega_{i_{\boldsymbol{k}}}$, (d-f) their standard deviations $\mathfrak{S}(\Omega_{i_{\boldsymbol{k}}})$ from the exact average and relative deviations of Hall conductivities $\delta\sigma_{i_{\boldsymbol{k}}}/\nu$ as a function of grid size for the state $i_{\boldsymbol{k}} = 6$, when it is in the excited-state quasi-continuum (top) and in the ground-state manifold (middle and bottom). The integrations in Equation (1.37) have been approximated by simple Riemann sums. N_φ is the number of points taken in the range $[0, 6\pi)$ in each direction.

integration is very close to the quantized value. This occurs even if the FCI state is not a ground state. In the example presented in Figure 5.4, the Hall conductivity is in all three cases equal to $\nu \times C = -1/3$ within the numerical accuracy, which will be discussed now.

The Hall conductivities calculated are very close to the expected exact values in the FCI regime, despite the fact that the integrations involved are performed numerically. The relative deviation with respect to the exact value for the case of $\nu = 1/3$ is presented in Figure 5.4. This example illustrates that the error in the Hall conductivity due to the finite size of the system should be smaller than 1%, at least for the Kubo formula approach, even for small systems. In the case of clearly gapped FCI ground states, the accuracy is even better, due to the integrand being very smooth. In all cases, a simple Riemann summation has been used to evaluate integrals, in order to obtain upper bounds for the numerical errors. Other methods, like the Simpson rule, would converge for smaller grid sizes. It should be noted that when the Hall conductivity of an individual state within the degenerate ground state is evaluated, the integration

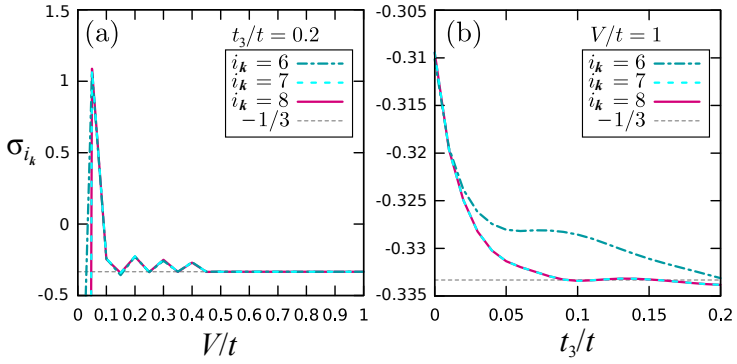

Figure 5.5: Hall conductivity, see Equation (1.37), for each of the three quasi-degenerate FCI states as a function of (a) the interaction strength V/t and (b) the third-neighbor hopping t_3/t (right). Note the different scales on the vertical axes.

should be extended over the whole period of the Berry curvature. This is no longer necessary when the Hall conductivity is averaged over all the states in the ground-state manifold. The integration range can then be restricted to $[0, 2\pi)^2$.

The effects of interaction and band dispersion can also be traced in the behavior of the Hall conductivity. This is shown in Figure 5.5. Outside the FCI regime, where low-energy levels cross upon flux insertion, the Hall conductivity oscillates. It converges to ν at about the value of V/t for which the FCI states separate from the excited-state spectrum, forming a three-fold degenerate ground state. On the other hand, the Hall conductivity of these states remains close to $-1/3$ with deviation from the flat-band limit, and only changes smoothly with t_3/t, converging to the expected value close to the phase boundary discussed in Section 5.5.

5.4 Disorder

The quantization of the Hall conductivity must be robust against disorder, if it is to be considered as a topological invariant, as long as the energy scale of the disorder is smaller than the gap [20]. The magnetic texture embedded in the hoppings of flux models will generally fluctuate, since, in several current approaches to Chern bands, the magnetic background is generated spontaneously by localized moments or itinerant electrons. An expected source of disorder are therefore local inhomogeneities in the flux pattern. A simplistic approach to simulate this effect is to vary the flux picked up by an electron hopping along one selected bond of the finite lattice. This is done by varying the phase φ' in the phase factor in front of the corresponding hopping. The effect of such a variation on Hall conductivities at $\nu = 1/3$ is shown in Figure 5.6.

As long as the energy scale of the disorder is small enough compared to the energy gap, the ground states remain separated from the rest of the spectrum and their average Hall conductivity remains constant. The Hall conductivities of the individual quasi-degenerate ground states are not smooth functions of magnetic disorder. In particular, as soon as the impurity is switched on, the

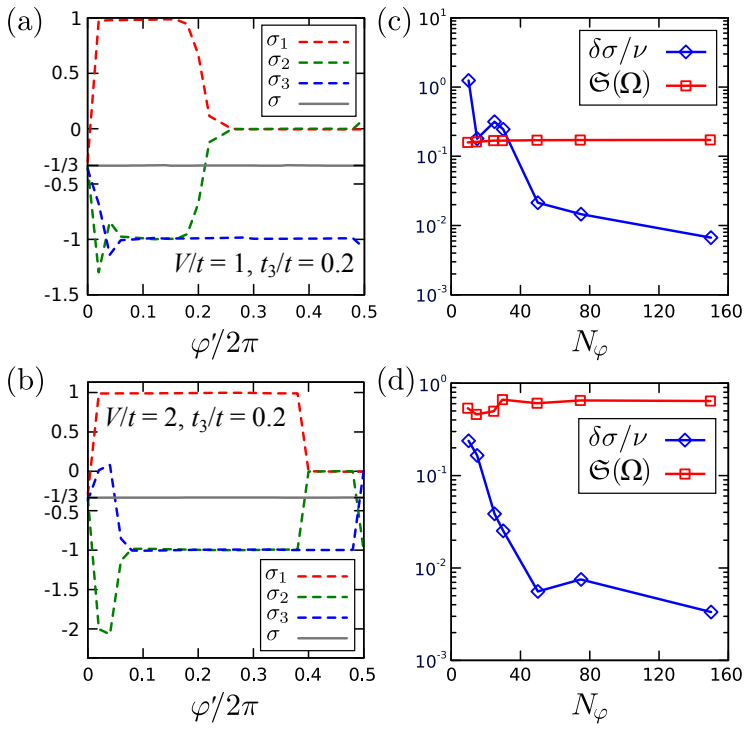

Figure 5.6: (a,b) Hall conductivities of the three lowest-energy states and their average as a function of disorder phase φ'. (c,d) Standard deviation $\mathfrak{S}(\Omega)$ of total Berry curvature Ω, defined by adding up the many-body Berry curvatures Ω_{i_k} of the three lowest-energy states for each value of φ, and relative deviation $\delta\sigma/\nu$ of Hall conductivity as a function of grid size. N_φ is the number of points taken in the range $[0, 2\pi)$ in each direction. The results shown in the right panels are for $\varphi' \simeq 2\pi/3$, but are qualitatively the same for all other values of φ'.

Hall conductivity of each individual state jumps to an integer value. Also, Berry curvatures are no longer smooth functions of φ_1 and φ_1. Nevertheless, the Hall conductivities are still numerically well-defined, as demonstrated in the right panels of Figure 5.6, and their average, which is the proper observable quantity in the thermodynamic limit, remains constant as the disorder is varied. This invariance of the Hall conductivity directly demonstrates the topological robustness of FCI states.

Again in analogy to FQH states [126], disorder introduces further splitting, apart from the one due to dispersion discussed in Section 5.1, between FCI ground-state eigenvalues, which no longer exchange places under flux insertion. This splitting is expected to be a finite-size effect and should disappear in the thermodynamic limit. Despite the similarities, the impact of disorder in general on the energy-scale balance necessary for FCI states is qualitatively different from the situation in traditional FQH states. For example, disorder may have a different effect depending on the interaction strength and range, and may lead to another, possibly topologically trivial, state, as has been shown in a recent

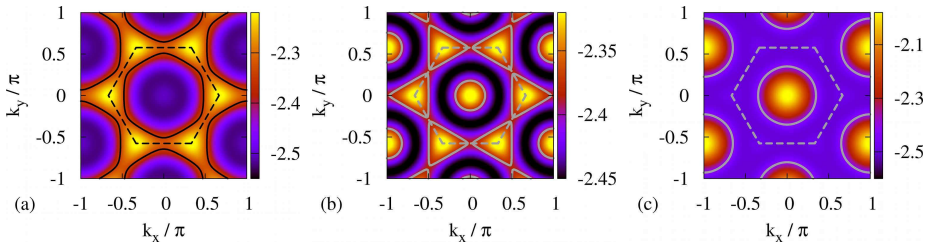

Figure 5.7: Dispersion and Fermi surface (FS) for $\nu = 2\rho = 2/3$ (thick solid line) for (a) $t_3/t = 0.16$ and $M = 11.16$, (b) $t_3/t = 0.19245$ and $M = 24$ (very close to maximal M) and (c) $t_3/t = 0.25$ and $M = 5.5$. Dashed lines indicate the first Brillouin zone.

study on the checkerboard lattice involving chemical-potential disorder [127].

5.5 Competition with charge order

Early on in the study of FCIs, it was pointed out that an important prerequisite for the emergence of a FCI state is the balance between three energy scales, namely the width of the topologically non-trivial band, the gap(s) separating it from other bands and the Coulomb interaction strength [80, 81, 106, 107]. If the ratio between the first two is large, then the interaction can become strong enough to induce FCI states, but remain small compared to the band gaps, so that different topological characters, i.e., Chern numbers, are not mixed in the interacting many-body wavefunction. Many investigations have hence been focused on models in the perfectly flat band limit, within which the only difference between Chern-bands and Landau-level descriptions is the variation of the single-particle Berry curvature. The corresponding models are then supplemented by various types of interactions. It was later reported that the band flatness alone is not in fact a reliable indicator for the stability of FCI states [118].

In this Section, the dependence of FCI states on band filling and FS nesting is examined. The first presents a rather obvious difference to LLs, namely, while a LL is expected to be particle-hole symmetric, the nearly-flat subband of a lattice model is not. The differences between filling fractions $\nu = 1/3$ and $\nu = 2/3$ clearly exemplify this difference. The latter case corresponds to $1/3$ filling of the normal triangular lattice, where NN Coulomb interaction can stabilize a CDW, while no such CDW is possible at $\nu = 1/3$. The competition between the FCI and the CDW is in turn affected by FS nesting. The $\nu = 2/3$ FCI state is more stable for more dispersive bands without nesting than for flatter bands with a nested Fermi surface. However, very flat bands allow for FCI states at the lowest interaction strengths, even though the corresponding FS is very well nested.

As mentioned in Section 3.2, varying t_3/t allows one to tune the flatness of the lower Chern band and to switch between regimes with and without FS nesting. Examples are shown in Figure 5.7, where the dispersion as well as the Fermi surface corresponding to $\nu = 2/3$ are shown for some values of t_3/t. Both for near-optimal $t_3/t = 0.19245$ ($M = 24$) and for smaller $t_3/t = 0.16$ ($M \approx 11$), the FS contains hexagons with almost perfectly nested segments. A difference

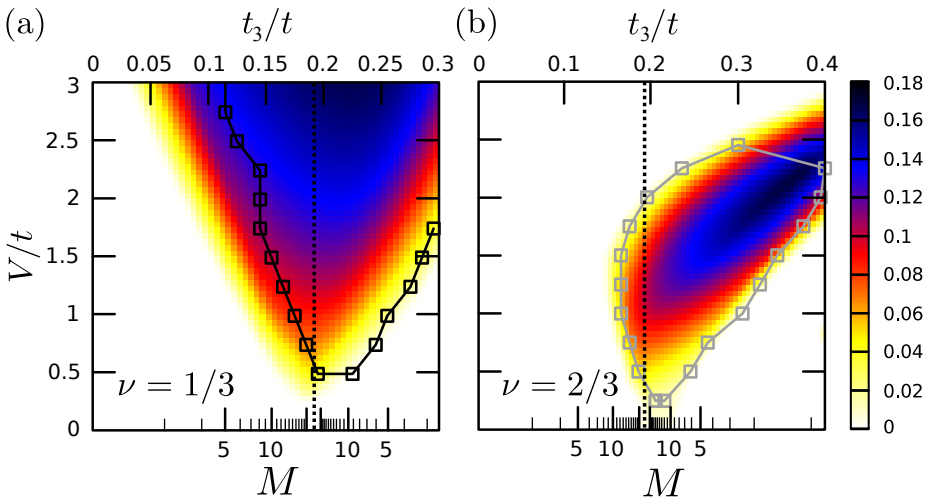

Figure 5.8: Gap of three-fold degenerate FCI ground state as a function of M and V/t, for (a) $\nu = 1/3$ and (b) $\nu = 2/3$, shown in colorcode. The dashed lines indicate the phase boundary, defined by the condition that the gap remains open for all values of inserted magnetic flux. The flatness ratio M of the lower Chern band (bottom scale) is adjusted by varying t_3/t (top scale). The maximum value of the flatness ratio ($M \simeq 24$) is marked by the dotted lines.

between the two cases is on one hand the flatness ratio, but on the other hand, the flatter bands also have an additional circular FS around the Γ point. For $t_3/t \gtrsim 0.23$, only the circular FS remains (see the example with $t_3/t = 0.25$ and $M = 5.5$) and there is thus no longer good nesting.

Figure 5.8 shows the region where FCI states are stable on a 24-site (4×3 unit-cell) system, as a function of Coulomb interaction strength V and the flatness ratio M, which is in turn controlled by third-neighbor hopping. The two panels are for fillings $\nu = 1/3$ and $\nu = 2/3$. In both cases, the ground-state manifold in the FCI state is expected to be three-fold degenerate. The color code indicates the gap between the three ground states and the fourth lowest eigenstate in the absence of applied magnetic flux. In order to define a physically meaningful phase boundary, however, one has to make sure that the ground states remain gapped upon flux insertion, not only in their own momentum sector, but also across momentum sectors, see Section 5.1. The solid lines in Figure 5.8 indicate the phase boundary determined by taking these considerations into account. The phase diagrams obtained from a 30-site torus are qualitatively the same as the ones shown here.

For both fillings, the system is in a metallic state at small V/t, while finite values of V/t can lead to FCI ground states for an extended range of the band flatness. In the case of $\nu = 1/3$, the FCI state can be induced for any band dispersion by making V large enough. The FCI persists even for V/t considerably larger than the band gap. This has also been observed for another FCI model on the checkerboard lattice [107] and appears to indicate that the fermions are dilute enough to occupy mostly one subband regardless of V/t, so that a mixing of the topological character of the two bands does not occur for intermediate

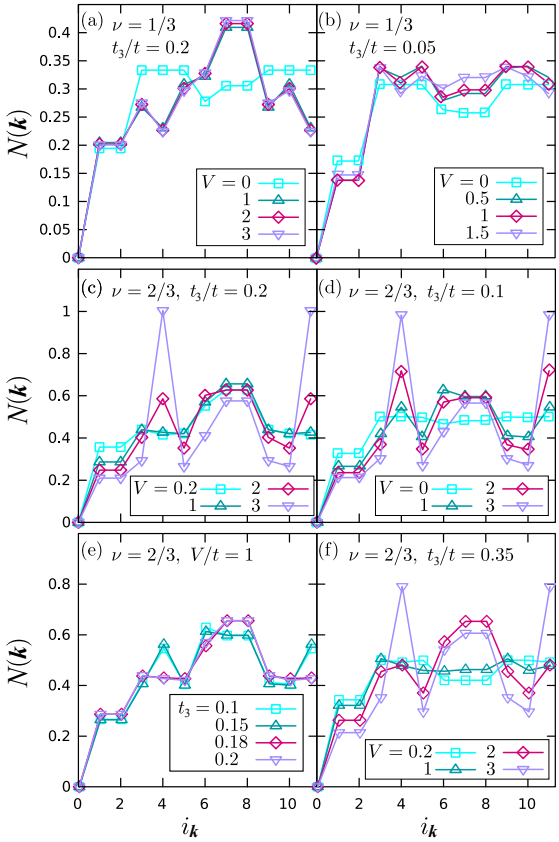

Figure 5.9: Static charge-structure factor for various values of t_3/t and V/t at filling fractions (a,b) $\nu = 1/3$ and (c-f) $\nu = 2/3$. The sharp peaks indicate the tendency towards charge ordering. In the FCI regime, the static structure factor of all three quasi-degenerate ground states is identical.

values of V. Stronger repulsion actually does mix the two Chern bands, but the $\nu = 1/3$ FCI state remains intact despite this mixing, as will be shown in Chapter 6. In contrast, the $\nu = 2/3$ FCI states survive only for moderate values of V/t. Larger interaction strengths lead to a different ground state, which is, as will be argued below, a CDW.

To determine the type of order in each of the regions in Figure 5.8, key observable quantities of the corresponding ground states can be calculated. FCI states, despite the hints from the energy spectrum, have to be identified by their topological invariant, see Section 5.3. To find out whether there is tendency towards charge order in the rest of the phase diagram, we calculate the static charge-structure factor $N(\boldsymbol{k})$, defined in Equation (4.12). Charge-density modulations are marked by sharp features in $N(\boldsymbol{k})$ at certain wavevectors. Liquid states, on the other hand, should be featureless in comparison to charge-modulated states.

Even though the accessible system sizes are not large enough to exemplify the featurelessness of liquid states, a qualitative difference between liquid and charge-modulated states can be seen. Examples are shown in Figure 5.9. At

$\nu = 1/3$ and within the FCI regime, $N(\boldsymbol{k})$ remains almost unchanged upon variation of model parameters. The same holds, although less markedly, for the metallic, Fermi-liquid-like state at small interaction strengths and small (or very large) t_3/t. Despite the fact that the shape of $N(\boldsymbol{k})$ is distinct for the two liquid states, see Figs. 5.9(a) and (b), the differences are subtle. In order to distinguish between the FCI and metallic states, one would thus rather use the topological invariant of their ground states, see Section 5.3, or the criterion that the quasi-degenerate groundstates remain separated from higher states for all fluxes, as used for Figure 5.8, see above.

However, the charge-structure factor is very valuable in distinguishing the weakly correlated Fermi liquid from a CDW driven by Coulomb repulsion. At $\nu = 2/3$ and $t_3/t = 0.1 < 0.18$, away from the FCI regime, two peaks appear in $N(\boldsymbol{k})$ and increase continuously upon increasing V/t, see Figure 5.9(d). When choosing $t_3/t = 0.2$ near the maximal flatness [Figure 5.9(c)] or $t_3/t = 0.35$ with bad FS nesting [Figure 5.9(f)], the peaks only begin to grow for large V, where ground-state behavior upon flux insertion changes: a full gap is only obtained for lattice sizes commensurate with the ordering pattern, like the 3×6 and 6×6 lattices, but not on more general lattices. This indicates that the FCI state breaks down and is replaced by a CDW. The peaks observed in $N(\boldsymbol{k})$ for $\nu = 2/3$ grow with V, supporting their relation to a CDW. Their wavevectors correspond to a state where particles sit at NNN sites on the triangular lattice, i.e., to the regular charge pattern compatible with a filling of $\rho = \nu/2 = 1/3$ of the triangular lattice. This pattern avoids any penalty due to NN Coulomb interaction V and large enough $V \gg t, t_3$ will thus eventually induce such a charge distribution.

The CDW at $\rho = 1/3$, which was examined in Chapter 4, is incommensurate on the clusters mentioned so far. This incommensurability becomes evident from the spectral flow of CDW eigenvalues upon inserting flux. This leads to level crossings, meaning that the incommensurate CDW ground states are not truly gapped. This is the reason for the absence of the CDW phase in the phase diagrams of Figure 5.8. Despite the incommensurability, density-density correlations are evidently present, as can be inferred from the sharply peaked $N(\boldsymbol{k})$, and are enough to destroy the FCI phase. One may therefore wonder about the fate of the FCI phase, when the latter competes with a commensurate CDW. Figure 5.10 shows precisely this competition. It is seen that FCI states survive the competition with the commensurate CDW, albeit in a limited range. The finiteness of the FCI area in the phase diagram has also been verified on a 6×6-site cluster.

The phase diagrams in Figures 5.8 and 5.10 clearly show that the band flatness parameterized by M is itself not a reliable indicator for the stability of FCI states, as has also been pointed out recently in for the case of the checkerboard-lattice model [118]. The energy gap for $\nu = 1/3$ is rather symmetric with respect to the highest figure of merit, but the phase boundary determined by requiring a full gap over all momentum sectors and for all fluxes shows that the FCI states are somewhat more stable for larger t_3/t. In the case of $\nu = 2/3$, the asymmetry is far more striking: as one can see in Figure 5.8(b), FCI states require rather flat bands with $M \approx 13$ for $t_3/t < 0.2$, but extend to a band with a width comparable to the gap separating it from its counterpart for $t_3/t > 0.2$. Having rather flat bands indeed makes it easier for small V/t to induce FCI states both at $\nu = 1/3$ and $\nu = 2/3$, even though the optimal M is still not quite

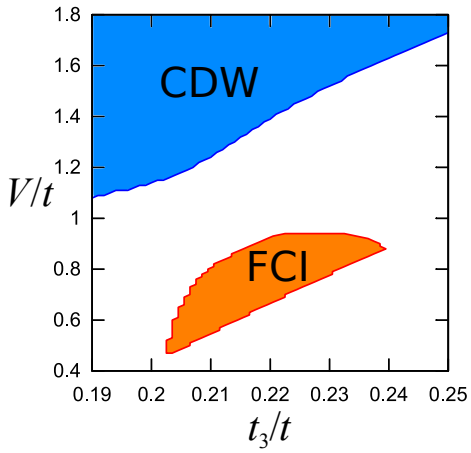

Figure 5.10: Phase diagram in the V-t_3 plane for a 6×3-site cluster, which is commensurate with the CDW pattern of Figure 4.1(a).

the largest, at least for our system sizes. As soon as the bands acquire some dispersion, however, features beyond band flatness, in our case FS nesting, can influence the stability of FCI states by favoring competing states, in our case a CDW. Another key feature, which extends previous results [118], is that in the case of competition between FCI and other phases, perfect band flatness is not necessarily the ideal condition for the stability of FCI ground states.

Before passing, a few more comments on the phase diagrams are due. Ideally, a ground-state property would be used to determine the phase boundaries. One such property, which is sensitive to phase transitions, is the ground-state fidelity, defined as a measure of the overlap $\langle\psi(\alpha)|\psi(\alpha+\delta\alpha)\rangle$, where ψ is the ground-state wavefunction and α is a control parameter varied in small steps $\delta\alpha$. Phase transitions are then marked by a divergence in the fidelity at the transition point. Having calculated the ground-state fidelity upon varying interaction strength and band flatness for the cases presented here, such divergences have been found to occur only at points where ground-state level crossings also occur, so the fidelity does not provide any extra information compared to the eigenvalue spectra. Furthermore, it has recently been shown that the fidelity on finite systems can fail to register topological phase transitions, e.g., between a FQH-like state and a Fermi liquid [127].

Chapter 6

Beyond isolated topological bands

Following the discussion in Section 1.2, one sees that the theoretical machinery developed to study partially filled Landau levels has been very useful in explaining and predicting observables of semiconductor devices in the fractional quantum Hall (FQH) regime. The essential physics can be accessed even if edge, contact and electron spin effects are neglected. Despite the fact that the lowest Landau level is considerably dispersive close to sample edges, one can restrict the description of FQH physics in the bulk, where energy is perfectly flat, without introducing any significant error. A further assumption usually made is that the influence of higher Landau levels is negligible. This assumption is perfectly valid for FQH states at $\nu = 1/q$, where the cyclotron gap is $\mathcal{O}(10)$ meV and the effects of disorder and interactions are weak[1].

The situation in lattice systems can be quite different. It was already shown in the preceding Chapter that FCI states are considerably affected by the dispersion of the underlying Chern band. Moreover, whereas Landau-level mixing by Coulomb interactions and disorder can be made small in the laboratory by appropriately preparing the FQH microdevices, it is not possible to drastically tune the ratio of interaction strength to band gap (the latter plays the role of the cyclotron gap for an FCI) to arbitrarily small numbers. Both energy scales are of the same order of magnitude in several relevant materials. However, most model Hamiltonians supporting FCI states have been engineered to have an infinite band gap. This is typically done so that Chern bands resemble isolated Landau levels as much as possible. To accomplish this, the energy scales inherent in an FCI should obey a particular hierarchy. The bandwidth W of the partially filled Chern band should be much smaller than the smallest band gap Δ to any other band. Furthermore, the interaction strength V should also be much smaller than the band gap, in order to avoid band mixing, but also much larger than the bandwidth, in order to affect particles in the partially filled Chern band as uniformly as possible, so as to mimic the situation in a partially filled Landau level. The energy-scale hierarchy is therefore $W \ll V \ll \Delta$. The

[1] Appropriate generalizations exist for FQH states at higher filling fractions. At some of these higher fillings, Landau-level mixing is essential to the physics and has to be taken *de facto* into account.

results presented in Section 5.5, however, already hinted at the fact that the inequality $V \ll \Delta$ is not essential for the emergence of FCI states. Chern bands and Landau levels are therefore expected to have distinct properties, whenever interactions are moderate to strong compared to the band gap, since strong interactions are generically expected to mix band characters in the ground state of a solid. Band mixing becomes even more crucial, when one wishes to realize FQH physics beyond the mK range.

In this chapter, it will be established that FCI states can arise even if interaction strengths are arbitrarily larger than the noninteracting band gap, going beyond the limits in which FCI states have been previously studied. The strong-coupling FCI states depart from the usual isolated-band picture that parallels the fractional quantum Hall effect in Landau levels and demonstrate how a topologically ordered state can arise in a truly multiband system. This result also implies that the search for such states can be extended to strongly correlated materials and that candidate systems need not have a very large gap to host them. It also proves that, in principle, mixing bands with opposite Chern numbers is not as detrimental to topological order as it is typically thought to be.

It should be stressed that, even though the results of this Chapter make FCI states more accessible to experiments, several material-science challenges remain. Changing the quantization value of the Hall conductivity depends on the ability to tune the filling fraction. For the conventional quantum Hall effect in semiconductors, one has, in addition to the ability to back gate the sample, the possibility to vary the magnetic field as a way to change filling fractions. For the known two-dimensional topological band insulators, it is much harder to change doping so as to approach a given commensurate filling fraction. Chemical doping could be used, but it may also introduce strong disorder. These are examples of complications that remain, but band mixing due to strong interactions, as will be now shown, is not one of the main obstacles to realizing a FCI phase of matter.

A large part of this Chapter has been previously published in Ref. [128] with T. Neupert, C. Chamon and C. Mudry.

6.1 Strong-coupling fractional Chern insulators

In this Chapter, the filling fraction is fixed to $\nu = 1/3$ of the lowest Chern band for each of the two models defined in Chapter 3. The question posed is whether or how the inclusion of $\hat{H}_{\text{int}}$ in $\hat{H}$ will mix the bands formed by the eigenvalues of $\hat{H}_{\text{kin}}$. To this end, one has to measure the contribution – if any – of the upper band to the FCI states, that is, the overlap

$$n_+ := \sum_{\boldsymbol{k}} \langle E_0 \left| \hat{n}_{\boldsymbol{k},+} \right| E_0 \rangle , \tag{6.1}$$

where $|E_0\rangle$ is any one of the states in the degenerate ground-state manifold and $\hat{n}_{\boldsymbol{k},+}$ is the operator measuring density of particles with upper-band character at wave-number $\boldsymbol{k}$. This is defined as follows: The eigendecomposition of Hamiltonian $\mathcal{H}$ can be written as $\mathcal{U}\,\mathcal{E}\,\mathcal{U}^\dagger$, where $\mathcal{E}$ is a diagonal 2×2 matrix containing the single-particle eigenvalues ε_+ and ε_- and $\mathcal{U}$ is a unitary 2×2

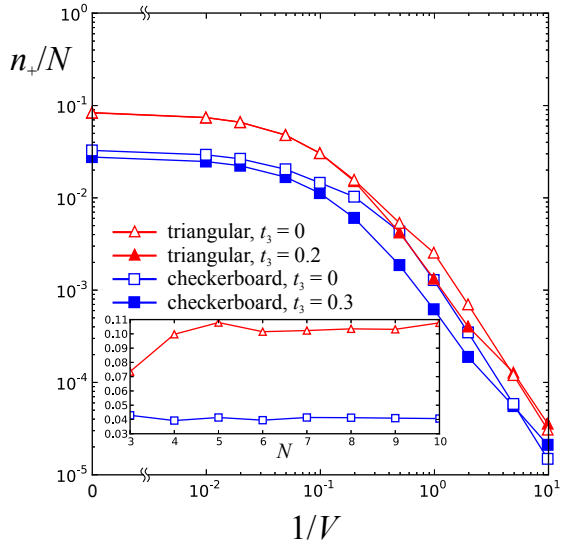

Figure 6.1: The density of upper-band character n_+ for one of the states in the FCI manifold in the checkerboard (squares) and triangular (triangles) lattice models on a 36-site cluster at $\nu = 1/3$, with a kinetic term yielding almost flat (full symbols) and non-flat (empty symbols) lower bands, as a function of $1/V$. Inset: the value of n_+ at $V = \infty$ as a function of system size, parametrized by the number of particles N.

matrix containing the eigenstates of $\mathcal{H}$ as columns. The transformation from the sublattice to the band basis can then be written as

$$\begin{pmatrix} \hat{c}_{\boldsymbol{k},+} \\ \hat{c}_{\boldsymbol{k},-} \end{pmatrix} = \mathcal{U}^\dagger \begin{pmatrix} \hat{c}_{\boldsymbol{k},A} \\ \hat{c}_{\boldsymbol{k},B} \end{pmatrix} = \begin{pmatrix} u^*_{A,+}\, \hat{c}_{\boldsymbol{k},A} + u^*_{B,+}\, \hat{c}_{\boldsymbol{k},B} \\ u^*_{A,-}\, \hat{c}_{\boldsymbol{k},A} + u^*_{B,-}\, \hat{c}_{\boldsymbol{k},B} \end{pmatrix} , \tag{6.2}$$

where u are the entries of $\mathcal{U}$. The density $\hat{n}_{\boldsymbol{k},+}$ is therefore

$$\begin{aligned} \hat{n}_{\boldsymbol{k},+} =& |u_{A,+}|^2\, \hat{n}_{\boldsymbol{k},A} + |u_{B,+}|^2\, \hat{n}_{\boldsymbol{k},B} \\ &+ u_{B,+}\, u^*_{A,+}\, \hat{c}^\dagger_{\boldsymbol{k},B}\, \hat{c}_{\boldsymbol{k},A} + u_{A,+}\, u^*_{B,+}\, \hat{c}^\dagger_{\boldsymbol{k},A}\, \hat{c}_{\boldsymbol{k},B} \,. \end{aligned} \tag{6.3}$$

The exact many-body ground-state expectation value of any one of $\hat{n}_{\boldsymbol{k},A}$, $\hat{n}_{\boldsymbol{k},B}$, $c^\dagger_{\boldsymbol{k},B}\, \hat{c}_{\boldsymbol{k},A}$ and $\hat{c}^\dagger_{\boldsymbol{k},A}\, \hat{c}_{\boldsymbol{k},B}$ can be evaluated numerically with exact diagonalization on finite clusters for any value of V.

Figure 6.1, shows the expectation value of n_+ for one of the states in the FCI manifold as a function of inverse interaction strength. In the weak-coupling limit, band mixing is very limited. However, as the interaction reaches its maximal value, the mixing increases and saturates at appreciable values for both models. The contributions to the occupation n_+ are almost uniformly distributed across the Brillouin zone in the finite clusters that have been studied here. Even though system sizes large enough for a finite-size extrapolation cannot be reached with exact diagonalization, n_+ shows no tendency of decreasing upon increasing system size, as can be seen in the inset of Figure 6.1. The dependence of n_+ on V is almost identical in the 48-site cluster with 8 particles and the 36-site cluster with 6 particles.

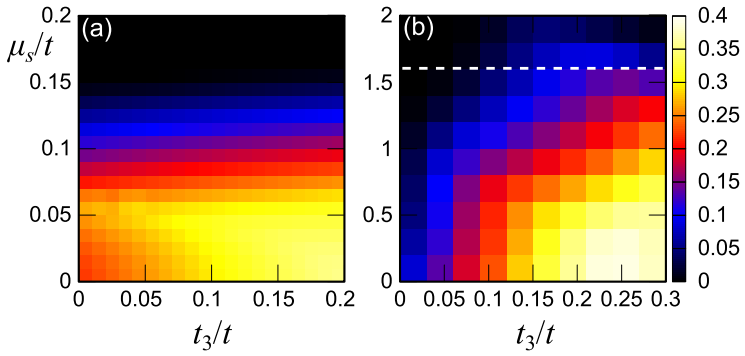

Figure 6.2: Phase diagrams of (a) the triangular and (b) the checkerboard lattice models on a 48-site cluster at $\nu = 1/3$, $V = \infty$ in the μ_s-t_3 plane. The color coding is the lowest value of the gap between FCI ground states and excited states upon flux insertion. The dashed white line in (b) denotes the phase boundary for the non-interacting model.

6.2 The limit of infinite V

Figure 6.1 has also introduced the limit in which the nearest-neighbor repulsive interaction strength V is taken to infinity. In this case, particles cannot occupy nearest-neighbor sites: any many-body state with two spinless fermions sitting on neighboring sites is projected out of the Hilbert space in this limit. Thus, for any site $\boldsymbol{i} \in \Lambda$ we define the projected operator $\tilde{c}_{\boldsymbol{i}}^\dagger$ by demanding that its action on any state in the occupation basis of the projected Hilbert space is to create a spinless fermion on $\boldsymbol{i}$ if and only if this site and all its nearest-neighbor sites are empty. Otherwise, $\tilde{c}_{\boldsymbol{i}}^\dagger$ annihilates any state from the projected Hilbert space. Formally,

$$\tilde{c}_{\boldsymbol{i}}^\dagger := \hat{c}_{\boldsymbol{i}}^\dagger \prod_{\boldsymbol{j} \in \langle \boldsymbol{i}\boldsymbol{j} \rangle} \left(1 - \hat{n}_{\boldsymbol{j}}\right), \tag{6.4a}$$

and

$$\begin{aligned} \hat{H} = & t \sum_{\langle \boldsymbol{i},\boldsymbol{j} \rangle} \left(e^{\mathrm{i}\phi_{\boldsymbol{i},\boldsymbol{j}}} \tilde{c}_{\boldsymbol{i}}^\dagger \tilde{c}_{\boldsymbol{j}} + \text{H.c.} \right) + t_2 \sum_{\langle\langle \boldsymbol{i},\boldsymbol{j} \rangle\rangle} (-1)^{|\boldsymbol{i}|} \left(\tilde{c}_{\boldsymbol{i}}^\dagger \tilde{c}_{\boldsymbol{j}} + \text{H.c.} \right) \\ & + t_3 \sum_{\langle\langle\langle \boldsymbol{i},\boldsymbol{j} \rangle\rangle\rangle} \left(\tilde{c}_{\boldsymbol{i}}^\dagger \tilde{c}_{\boldsymbol{j}} + \text{H.c.} \right) + \mu_{\text{s}} \sum_{\boldsymbol{i}} (-1)^{|\boldsymbol{i}|} \tilde{c}_{\boldsymbol{i}}^\dagger \tilde{c}_{\boldsymbol{i}} \,. \end{aligned} \tag{6.4b}$$

Here, $\phi_{\boldsymbol{i},\boldsymbol{j}}$ are the phase factors needed to represent each of the two models of Equations (3.3) and (3.4) and $|\boldsymbol{i}|$ has been set to be even (odd) on sublattice A (B). For the triangular-lattice model defined in Eq. (3.4) with $t_3 = 0$, this limit gives rise to the Hamiltonian

$$\hat{H}_\triangle := \sum_{\langle \boldsymbol{i},\boldsymbol{j} \rangle} \left(e^{\mathrm{i}\phi_{\boldsymbol{i},\boldsymbol{j}}} \tilde{c}_{\boldsymbol{i}}^\dagger \tilde{c}_{\boldsymbol{j}} + \text{H.c.} \right) . \tag{6.5}$$

Hamiltonian $\hat{H}_\triangle$ contains no free parameters. $\hat{H}_\triangle$ is similar to previously studied, topologically trivial, supersymmetric models [129], which yield exotic

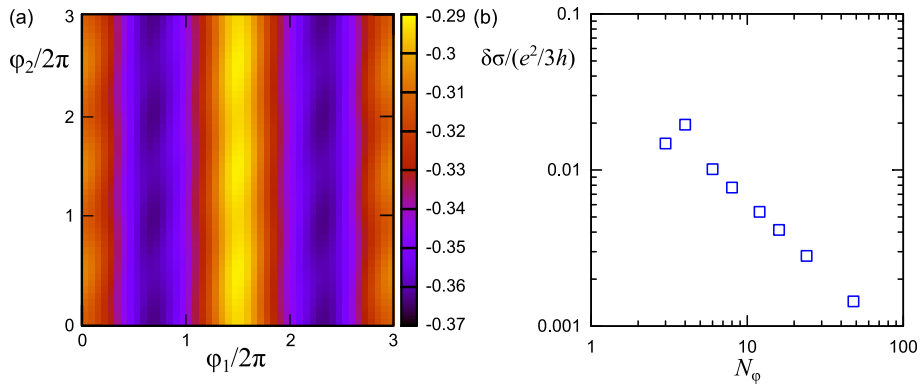

Figure 6.3: (a) Berry curvature and (b) relative error in the evaluated Hall conductivity as a function of the square root of the number of points in the flux-Brillouin zone partition for the triangular lattice model on a 48-site cluster at $\nu = 1/3$, $V = \infty$, $t_3 = 0$.

"superfrustrated" states with extensive groundstate degeneracy in many lattices [130]. It will be seen below that $\hat{H}_{\triangle}$ gives rise to FCI states at $\nu = 1/3$ of the lower band, i.e., 1/6 filling of the full lattice.

One can show that, despite the fact that at $V = \infty$ the bands are mixed, the FCI states remain robust for arbitrarily large interactions. To this end, the phase diagrams of the two models at $V = \infty$ in the μ_s-t_3 plane are presented in Figure 6.2. In both cases, the FCI phase is quite robust and does not depend crucially on the flatness of the original band. The FCI phase on the triangular lattice is quite sensitive to the introduction of the staggered chemical potential μ_s, presumably because this leads to an effective reduction in dimensionality at low energies. On the contrary, the FCI on the checkerboard lattice seems to be quite robust against μ_s. This phase seems to survive beyond the point where the bands of the non-interacting model would become topologically trivial, but this may be a finite-size artifact. Within the FCI regime (the colored part of the phase diagrams), the ground-state eigenvalues exhibit the empirical characteristic features of FCI states: 3-fold degeneracy and spectral flow.

In order to establish beyond doubt that the strong-coupling phases encountered here are indeed FCIs, the Hall conductivity has been calculated in this regime. It is found to be very precisely quantized to the value $-1/3 \times e^2/h$. The Berry curvature, as well as the accuracy of the quantization are shown in Figure 6.3. We notice that the Berry curvature is a very smooth function of φ_1, φ_2. This prediction has important consequences for experiments. Since the two bands with opposite Chern numbers are mixed by interactions, the edge-state picture of topological states becomes much less clear in this case. The quantized value of the Hall conductivity, however, is independent of details such as geometry and the microscopic termination of the sample, which would determine the detailed structure of the edge channels.

The infinite-V limit comes with a considerable reduction of the dimensionality of the Fock space [131, 132]. Technically, this may be crucial in the search for new topological states, especially in higher dimensions, where the lattice coordination and thus the reduction of the Hilbert space is typically higher. Evidently,

taking further-neighbor repulsive interactions V_2, V_3, ... to the hardcore limit $V_2 \to \infty$, $V_3 \to \infty$, ... allows for even more dramatic reductions of the Hilbert space. It should be mentioned that strong interactions may give rise to competing charge order [49] or more exotic compositely ordered states [133], whenever said competing orders are commensurate with the lattice. The results presented here are hence valid for short-range interactions at low enough densities, so that competing strong-coupling instabilities are ruled out.

Chapter 7

Combined topological & Landau order

Chapters 4 and 5 were devoted to two different scenarios that arise from the inclusion of short-range repulsion in flux models of spinless fermions. Depending on lattice geometry, filling fraction, and interaction strength and range, one can end up with either Landau-type charge order or a fractional Chern insulator, the lattice analogue of the fractional quantum Hall effect without the presence of applied magnetic fields. The triangular-lattice model introduced in Section 3.2 can host both states and allows for the study of their competition, which was presented in Section 5.5. The question posed here is whether there is a phase that exhibits the defining features of both a CDW and an FCI.

In this Chapter, compelling numerical evidence for a new class of quantum states, which exhibit both topological order and conventional breaking of translational symmetry due to strong interactions, is presented and discussed. These states can be viewed as composites of a CDW state and a FCI state formed by additional particles in the part of the lattice that remains unoccupied by the CDW, in some sense similar to the superfluid coexisting with a CDW in a supersolid. The eigenvalue spectra of the Hamiltonian defined in Equations (3.4) at filling fractions $\nu = 12/15 = 4/5$ and $13/15$, presented in Section 7.1, hint at ground states that are neither FCI nor CDW, but have features of both. The Landau order, commensurate charge modulation in the ground states, reveals itself in the interaction-dependent peaks of the static charge-structure factor. The topological order is established via the Hall conductivity, which is precisely quantized, but with a value $\sigma \neq \nu \times C$. Instead,the quantization is consistent with composite-state picture mentioned above. The phase diagram for a particular example of this novel class of exotic states is traced in Section 7.2.

Like the strong-coupling FCIs of Chapter 6, the composite states with coexisting Landau and topological order encountered here, which are dubbed topological pinball liquids (TPL) for reasons that will be discussed below, mix both bands of the model with Chern numbers $C = \pm 1$, and are made possible by the geometric frustration of the triangular lattice. The TPL is thus a state that arises out of lattice features that go beyond the single-band picture usually sufficient to describe FCIs and definitely defies any mapping to a Landau-level description. In contrast to FCIs arising in a magnetically ordered system [68, 134],

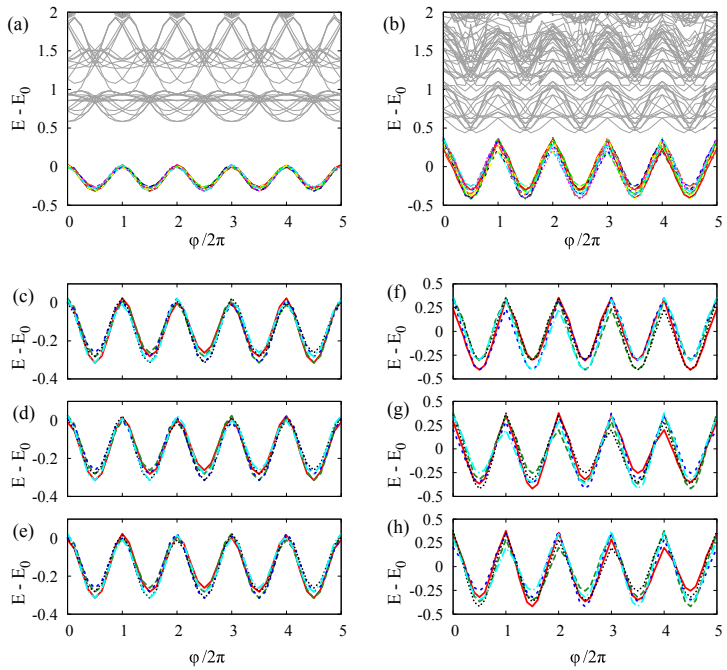

Figure 7.1: Spectral flow upon flux insertion for the triangular-lattice model of Equations (3.4) on a 15 unit-cell system at (a) $\nu = 12/15$ and (b) $\nu = 13/15$. In (c-e) and (f-h), the 15 low-energy states of (a) resp. (b) are divided into three groups of five; each group shows spectral flow consistent with a denominator-5 FCI. Fluxes are inserted as additional phases in the hoppings, totaling to φ for a loop around the cluster along direction $\boldsymbol{a}_3$. Parameters are $t_3/t = 0.2$, $V/t = 10$ and $V_2 = V_3 = 2t$.

where Landau order is found in a different degree of freedom, both types of order are here in the charge sector. In analogy to a supersolid on the triangular lattice, similar states might be found on other lattices supporting supersolids or pinball liquids, possibly also in multi-orbital settings [135].

A large part of this Chapter has been previously published in Ref. [133] with M. Daghofer.

7.1 Signatures of composite order

The starting point for the search of combined charge and topological order is to ask what will happen if the CDW of Figure 4.1(a) is doped with extra particles. One possibility is that charge order will collapse and that the system will transition into a metallic state or some incommensurate order. If, however, the charge order is robust, then it will remain intact and the extra particle density will move around the charge pattern. The resulting state can be intuitively understood as comprising of particles that play two roles simultaneously. Most of them form

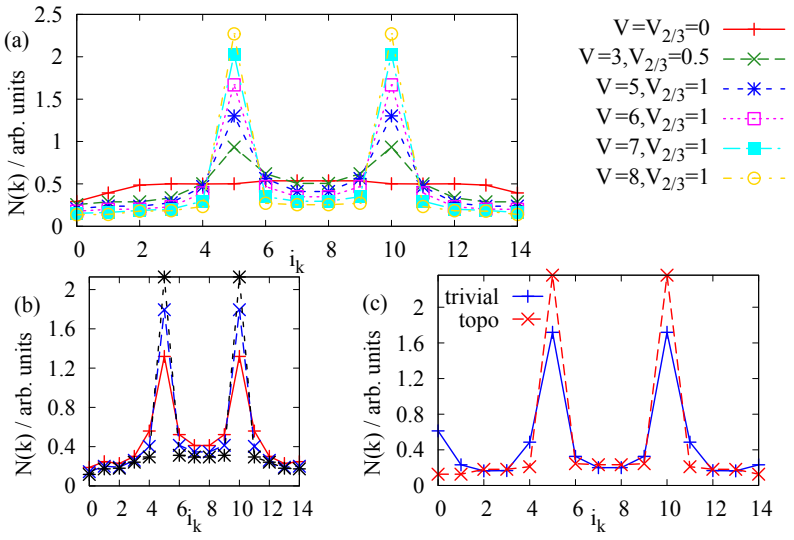

Figure 7.2: Charge-structure factor $N(\boldsymbol{k})$. (a) for $\rho = 12/30$ and (b) for $\rho = 13/30$, $V_2 = V_3 = 2t$, and $V = 8t$ (+), $V = 10t$ (×), and $V = 12t$ (∗). (c) Comparison of topologically trivial and nontrivial kinetic energy for $V/t = 10$, $V_2 = V_3 = 2t$. $t_3 = 0.2t$ and in the trivial case, $g_3 = m = 2t$. Of the 15 available momenta, numbers 5 and 10 correspond the ordering momenta of the CDW.

the CDW occupying 1/3 of the lattice sites. Additional particles can then move on the remaining sites, up to an additional density of $\rho = 2/3$. One can view the remaining sites as an effective honeycomb lattice with a 4-site unit cell, pictured in Figure 4.1(a). Due to the non-trivial flux arrangements present in the hoppings and the short-range repulsion, the residual particle density can form an FCI, whenever the effective lattice is filled up to an FQH filling fraction. The topologically trivial counterparts of these proposed states, called pinball liquids, have been extensively studied, as they are believed to form in two-dimensional molecular solids, and their presence in models similar to the one studied here (but without complex hoppings) has been thoroughly established [136–139].

Having drawn the cartoon picture of the sought-after state, one can start looking for its traces in numerical results. Figure 7.1 gives the eigenvalue spectrum for fillings $\rho = 12/30, 13/30$ and shows a 15-fold degenerate ground state as well as spectral flow. It will now be shown that these clues are inconsistent with simple FCI states. For the first case, the degeneracy expected for a straightforward FCI with $\nu = 12/15 = 4/5$ would be 5, instead of the observed 15. In the second case, the degeneracy is consistent with a $\nu = 13/15$ FCI, but levels return to their initial configuration already after insertion of only five flux quanta. Closer inspection shows that the 15 low-energy states can be separated into three groups of five states each, where each group shows the spectral flow expected for a denominator-five state, see Figs. 7.1(c-e) and 7.1(f-h). It is also known that additional interaction-generated dispersion tends to destabilize FCIs at such high fillings [112, 140].

The Hall conductivity establishes this similarity to $\nu = 2/5$ ($\nu = 3/5$) states

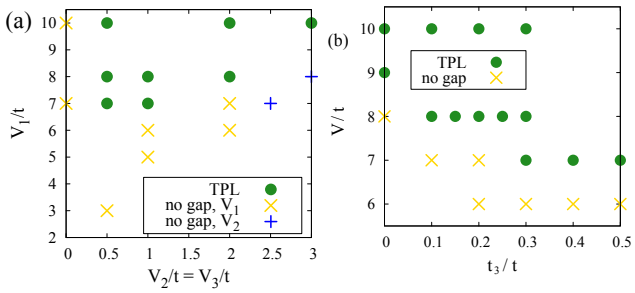

Figure 7.3: Phase diagram for $\rho = 12/30$ (a) depending on V and t_3 for $V_2 = V_3 = 2t$, and (b) depending on V and $V_2 = V_3$ for $t_3 = 0.2t$. Filled circles denote TPL states, $\times$ non-TPL states where $N(\mathbf{k})$ is peaked at the ordering vectors (i.e., charge modulations are driven by V), and $+$ states where V_2 destabilizes this charge pattern, see Fig. 7.2(c).

rather than 4/5 (13/15), as it is precisely quantized to $\sigma = -0.4$ ($\sigma = -0.6$), using everywhere units of e^2/h, for each of the ground states. As in some FCI states, e.g., the one at $\nu = 2/3$, the sum of contributions to the Hall conductivity does not add up to the Chern number of the non-interacting band. However, the present states are considerably more exotic as $\sigma = C \times m/n$ at $\nu = p/q$, with $n \neq q$. The Hall conductivity is thus not given by the usual heuristic $\sigma = \nu \times C$. Similar to earlier observations for the FQH effect in the presence of an external potential [141], this is a strong indication that the topological degeneracy differs from the number of ground states and is here in both cases $n = 5$ rather than $q = 15$. For a filling of 18 electrons on 30 sites, one likewise finds both charge order, a 15-fold near ground-state degeneracy and $\sigma = 0.4$ (with $V/t = 20$, $V_2/4 = V_3/4 = 4$, $t_3/t = 0.2$). This agrees with expectations based on a particle-hole transformed situation of the 12-electron case, where 10 holes form the CDW while the remaining 2 move between them.

The remaining, topologically trivial, three-fold degeneracy stems from the Landau-type charge order observed in Section 4.2, as revealed by the static charge-structure factor depicted in Figs. 7.2(a) and 7.2(b). For $V_1 > 0$, it peaks at the ordering vectors for the $\rho = 1/3$ CDW; the peaks grow when stronger V_1 enhances charge order. Therefore, five FCI states (corresponding to $\nu = 2/5$ or $\nu = 3/5$) arise for each of the three ground states of the CDW, totaling to the 15 observed ground states. Five FCI states per CDW state exhibit spectral flow, as seen in Figure 7.1, and return to the original point after insertion of 5 fluxes. The CDW itself does not rely on band topology: Going to a topologically trivial mass term $g_3 = 2t = \text{const.}$ [1] somewhat favors a competing sublattice ordering, but charge order nevertheless remains strong, see Figure 7.2(c). However, the state is then topologically trivial with $\sigma = 0$.

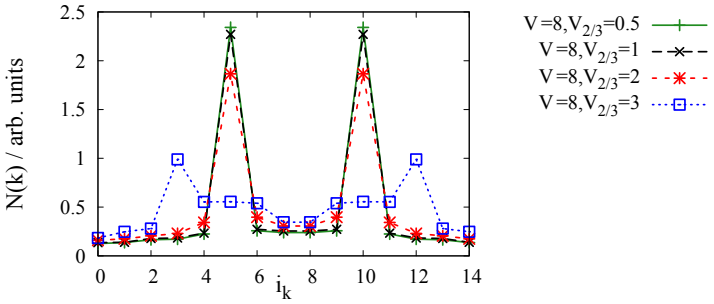

Figure 7.4: Static charge-structure factor $N(\boldsymbol{k})$ illustrating how longer-range coulomb repulsion $V_2 = V_3$ destabilizes the CDW pattern shown in Figure 1(b) of the main text. Momenta indices 5 and 10 correspond to the ordering vectors of the CDW, for $V_2 = V_3 = 3t$, $N(\boldsymbol{k})$ is no longer peaked there. $V = 8t$ and $t_3 = 0.2t$ in all cases, filling is 12 electrons on 30 sites/15 unit cells.

7.2 Phase diagrams

The phase diagrams of the $\rho = 12/30$ state in the V-t_3 and V-$V_2 = V_3$ planes are shown in Figure 7.3. Comparison to the phase diagram of the simple commensurate CDW at $\rho = 1/3$ (Figure 5.10) shows that the TPL needs stronger interactions, consistent with observations in supersolids [142]. In contrast to the pure FCI, the TPL is not induced more easily for the nearly flat bands at $t_3 \approx 0.2t$ than for more dispersive bands. Moreover, 18 electrons (i.e. 12 holes) also show a TPL with charge order, 15 ground states, and $\sigma = 0.4$, even though the "lower" band for holes is quite dispersive. This may be connected to an intrinsically reduced dispersion in the pinball state [139], or may be due to the rather strong interactions needed to stabilize a CDW, which can then overcome substantial dispersion [49]. Interactions, together with band topology and a partial frustration of the CDW, dominate here over the details of the lower Chern band that were important at weaker interactions. Note, also, that the simple cartoon "CDW + FCI" picture of the previous section does not fully capture the correlated quantum character of the TPL: for perfect charge order and $t_3 = 0$, the lowest subband of the effective system is not a Chern band. Nevertheless, charge fluctuations at finite V allow a TPL.

Figure 7.4 shows that $V_2 = V_3 \gtrsim 3t$ destroys the $\rho = 12/30$ CDW for $V = 8t$. Generally, the critical value is $V_2 \approx V/3$. As can be seen in the phase diagram for $t_3 = 0.2t$ in Figure 7.3(b), finite V_2 and V_3 is helpful, and may even be necessary, in inducing the TPL. When longer-range interactions are strong enough to weaken the CDW, however, first the TPL disappears and $N(\boldsymbol{k})$ finally is no longer peaked at the momenta corresponding to the ordering vectors.

While a finite-size scaling involving several cluster sizes at the same filling is not possible in our case, we were able to address somewhat larger clusters for the limit of strong nearest-neighbor Coulomb repulsion. In this limit, the Hilbert space can be reduced by discarding high-energy states with too many electrons

[1] Additionally, the third-neighbor hopping along $\boldsymbol{a}_3$ was set to 0. The lower band then has a similarly flat dispersion as in the topological case.

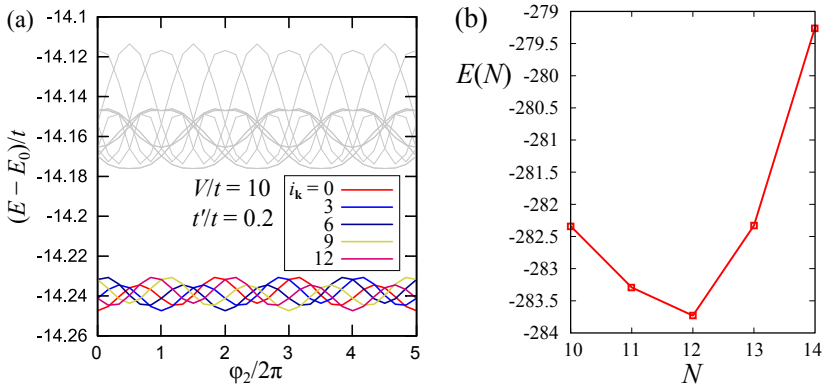

Figure 7.5: (a) Spectral flow of the eigenvalues of the effective honeycomb lattice – denoted by thick black lines in Figure 4.1(a) – with 6 particles in a 3×5-cell cluster ($\nu = 2/5$) with $V/t = 10$ and $t'/t = 0.2$, which models the residual lattice after assuming perfect charge order. (b) Total energy as a function of particle number on the 30-site cluster for $V_1/t = 10, V_2/t = V_3/t = 2$.

occupying NN sites, i.e., only states with an "almost perfect" CDW have to be kept. The Hamiltonian can then be diagonalized for a cluster of 6×6 sites (18 unit cells) and a filling of 14 electrons. In this treatment, 0, 1, or 2 faults are allowed in the CDW. The consistent results found lead to the conclusion that the approximated Hilbert space still captures all relevant states. In agreement with the expectations for a topological pinball liquid, nine-fold degenerate ground state, 3-fold for the CDW and 3-fold for the FCI, is found. The latter can be understood in terms of two electrons that fill one third of the lowest subband resulting from the effective lattice. Accordingly, one finds $\sigma = -1/3$ in each of the nine states and inserting fluxes reveals that three groups of three states each show spectral flow, with $6\pi = 3 \times 2\pi$ bringing the system back to the original point. Parameter sets treated include: $V/t = 100, V_2/1 = V_3/t = 1$; $V/t = 100, V_2/1 = V_3/t = 2$; $V/t = 10, V_2/1 = V_3/t = 2$. In all cases, $t_3/t = 0.2$.

The above results also further ascertain the robustness of the CDW part of the TPL states as the system size is increased. Taking this robustness into account, we can now treat larger systems, in which the "pins" of the pinball are now kept fixed. This allows us to treat the interacting particles on the residual lattice using the effective honeycomb-lattice model shown in Fig. 1(b) of the main text. For this model, we have studied the $\nu = 2/5$ state for up to 6 particles. We have verified that the ground state is 5-fold degenerate (since we have removed by hand the 3-fold degeneracy of the CDW), the levels that comprise it exhibit spectral flow (see Fig. 7.5), and the corresponding states have a very precicely quantized $\sigma = 2/5$ in units of e^2/h. Therefore, as long as the CDW component of a TPL state remains robust when the system size is increased (as was seen above), it is reasonable to expect that TPL states survive for larger systems as well. This suggests that TPL states will be, in principle, stable in the thermodynamic limit, at least in a perfect system at zero temperature, since there is no intrinsic feature of these states that prevents thermodynamic stability. Phase separation into a charge ordered and an FCI domain within the lattice would be hard to reconcile with the observables discussed above. Addi-

tionally, the total energy depending on filling is convex for fillings between 10 and 14 electrons on the 30-site cluster, as shown in Fig. 7.5(b), also arguing for a thermodynamically stable phase.

Chapter 8

Conclusions & outlook

After an introduction to the quintessential properties characterizing quantum Hall effects and topological phases in Part I of the present text, Part II has ventured into the less explored realm of correlated topological states in lattices. Haldane-like models were doped to fractional fillings of the gapped lower band and short-range interactions were used to induce lattice reincarnations of fractional quantum Hall states, called fractional Chern insulators (FCI). Unlike their Landau-level predecessors, these states require no externally applied magnetic field and arise in dispersive bands, characterized by a non-zero Chern number. These attributes render FCIs a novel class of topologically ordered phases with distinctive properties. Bands in solids are never fully isolated and the presence of a band structure must often be taken into account, especially when strong interactions and competing phases are present. In Chapter 5, it was shown that band dispersion, which is usually taken to be zero to mimic Landau levels, can affect the competition between CDW and FCI states and actually favor the latter against the former. Furthermore, a first rudimentary look at the effect of magnetic disorder on a fractionally quantized topological invariant indicated that, even though the impact of disorder is intricate, the quantization of the invariant remains intact. The results presented in Chapter 6 demonstrate that FCI states do not necessarily need to come purely from a single Chern band, since strong interactions that mix bands seem to enhance their stability. The possibility for obtaining exotic correlated topological states was exemplified by the topological pinball liquid – a composite quantum state comprising of a CDW and a FCI – in Chapter 7.

The conclusions of the preceding Chapters can be now set forth as answers to the questions posed in the beginning of Part II:

- Are weak or strong interactions more favorable to correlated topological states?
  - The answer to this question depends on geometry, filling fraction and commensurability of competing orders. In the absence of competition with charge order, which is the case in dilute systems with short-range repulsion, stronger interactions enhance the stability of FCI states. This statement remains valid, remarkably, even if interactions are cranked up to infinity and Chern bands are considerably mixed. This unexpected feature expands the range of candidate physical settings to include strongly

correlated systems, which were previously avoided as unsuitable for topological ordering. Competing interaction-driven charge order alters this picture drastically. Charge-density modulations destroy the FCI liquid and dominate the phase diagram even at intermediate values of the interaction strength. For weak interactions, the outcome of the competition depends on kinetics.

- Are insulators or semiconductors more suitable hosts?
  - Both can give rise to equally robust correlated topological states, depending on the precise balance of energy scales. The results obtained from various models so far suggest that there is a connection between coordination number and FCI stability, which shines favorably on the triangular-lattice model of Section 3.2. The sensitivity to a sublattice-staggered on-site potential exhibited in the phase diagram of Chapter 6, however, weakens FCI states in this model, even when the gap to bandwidth ratio suggests a robust underlying insulating state. On the other hand, the FCI states of the π-flux model on the checkerboard lattice survive a staggered chemical potential of considerable magnitude, even though the many-body gap is smaller than the one of their triangular-lattice counterparts.

- Are dispersive or flat bands more susceptible to topological order?
  - The flatness of Chern bands matters only in the weakly-correlated regime. Even there, flatter does not necessarily mean better for topological ordering, as shown in Section 5.5, even though in general it does rather help. Strongly correlated states, on the other hand, do not seem to be very affected by the flatness of the underlying band. This is noteworthy, since the interaction term itself is topologically trivial and, even though it is dominant in the strong-correlation regime, it is the weaker kinetic terms that cause the topological non-triviality.

- Are correlated topological phases beyond the fractional quantum Hall paradigm possible in single-species many-particle systems?
  - Yes. Strong correlations in lattice systems are responsible for a zoo of unconventional ordered states. The same is expected to hold for topological orders – a view that is supported by numerous quantum field theory predictions. Chapter 7 has introduced a new class of states, discovered in a simple lattice model, that serves as an example of "unconventional" topological ordering, induced by the simultaneous development of charge order.

These conclusions immediately point towards interesting directions for future work on correlated topological phases, with perhaps the two most obvious ones being generalizations to time-reversal symmetric and / or three-dimensional systems. Even though these possibilities are attractive, this route has already been laid out, to a certain extent, by the developments that led to the discovery of topological insulators. Another appealing prospect that is currently being

pursued is that of topological states arising from topologically trivial bands. Since states like the ones introduced in Chapter 7 have a topological character that cannot be deduced from the non-interacting band structure, it is intriguing to look for complex topological states in systems without underlying topological bands. It is naturally expected that the effects of a topological non-triviality should also be traceable even in gapless systems. This situation may arise in systems that feature an interplay between frustrated magnetic interactions and itinerant electrons, such as metallic spin-ice systems [143, 144]. Somewhat relatedly, it would be interesting to track the fate of a topologically ordered state whenever there are non-trivial correlations between magnetic impurities, as is the case when impurity interactions are frustrated.

In addition to properties already used to detect such states, the evaluation and, possibly, the measurement of quantities related to quantum entanglement, such as the entanglement spectrum, can be employed to further the understanding of correlated topological phases. The prediction of experimental observations is another direction of research on its own. So far, topological states have been primarily identified by detecting edge states. This route, however, may not always be viable and cannot capture key properties of the bulk. It is therefore desirable to find new experimental signatures of topological states. During measurements, excitations are created in a system, which propagate before being detected. Especially in the case of fractional topological states, the highly non-trivial and exciting phenomenon of fractionalization arises, in which electrons are effectively split into quasiparticles with fractional charge and exchange / exclusion statistics, as described in Section 1.2. It is crucial to understand how such quasiparticle excitations, some of which can become the building blocks of a quantum computer, can be generated and how they behave during experiments. The next step would then be to address the manipulation of topological states and their excitations, perhaps reverse-engineering desired properties into suitably designed models. An example is furnished by the composite states of Chapter 7: the fact that charge order can in principle be detected and manipulated relatively easily offers the possibility of controlling the topologically non-trivial component of a composite state indirectly.

Publication list

6. *Fractional Chern insulators with strong interactions that far exceed band gaps*
S. Kourtis, T. Neupert, C. Chamon, and C. Mudry
Physical Review Letters **112**, 126806 (2014)

Abstract: We study two models for spinless fermions featuring topologically nontrivial bands characterized by Chern numbers $C = \pm 1$ at fractional filling. Using exact diagonalization, we show that, even for infinitely strong nearest-neighbor repulsion, the ground states of these models belong to the recently discovered class of quantum liquids called fractional Chern insulators (FCI). Thus, we establish that FCI states can arise even if interaction strengths are arbitrarily larger than the noninteracting band gap, going beyond the limits in which FCI states have been previously studied. The strong-coupling FCI states, therefore, depart from the usual isolated-band picture that parallels the fractional quantum Hall effect in Landau levels and demonstrate how a topologically ordered state can arise in a truly multiband system.

A large part of this publication has been included in Chapter 6 of this dissertation.

5. *Femtosecond dynamics of magnetic excitations from resonant inelastic x-ray scattering in $CaCu_2O_3$*
V. Bisogni, S. Kourtis, C. Monney, K. Zhou, R. Kraus, C. Sekar, V. Strocov, B. Büchner, J. van den Brink, L. Braicovich, T. Schmitt, M. Daghofer, and J. Geck
Physical Review Letters **112**, 147401 (2014)

Abstract: Taking as an example spinon excitations in the quantum antiferromagnet $CaCu_2O_3$, we demonstrate that femtosecond dynamics of magnetic electronic excitations can be probed by direct resonant inelastic x-ray scattering (RIXS). To this end, we isolate the contributions of single and double spin-flip excitations in experimental RIXS spectra, identify the physical mechanisms that cause them, and determine their respective time scales. By comparing theory and experiment, we find that double spin flips need a finite amount of time to be generated, rendering them sensitive to the core-hole lifetime, whereas single spin flips are, to a very good approximation, independent of it. This shows that RIXS can grant access to time-domain dynamics of excitations and illustrates how RIXS experiments can distinguish between excitations in correlated electron systems based on their different time dependence.

This publication has not been included in this dissertation.

4. *Combined topological and Landau order from strong correlations in Chern bands*
S. Kourtis and M. Daghofer
arXiv:1305.6948 (2013)

Abstract: We present a class of states with both topological and conventional Landau order that arise out of strongly interacting spinless fermions in fractionally filled and topologically non-trivial bands with Chern number $C = \pm 1$. These quantum states show the features of fractional Chern insulators, such as fractional Hall conductivity and interchange of ground-state levels upon insertion of a magnetic flux. In addition, they exhibit charge order and a related additional trivial ground-state degeneracy. Band mixing and geometric frustration of the charge pattern place these lattice states markedly beyond a single-band description.

A large part of this preprint has been included in Chapter 7 of this dissertation.

3. *Fractional Chern insulator on a triangular lattice of strongly correlated t_{2g} electrons*
S. Kourtis, J. W. F. Venderbos, and M. Daghofer
Physical Review B **86**, 235118 (2012)

Abstract: We discuss the low-energy limit of three-orbital Kondo-lattice and Hubbard models describing t2g orbitals on a triangular lattice near half-filling. We analyze how very flat single-particle bands with nontrivial topological character, a Chern number $C = \pm 1$, arise both in the limit of infinite on-site interactions as well as in more realistic regimes. Exact diagonalization is then used to investigate an effective one-orbital spinless-fermion model at fractional fillings including nearest-neighbor interaction V; it reveals signatures of fractional Chern insulator (FCI) states for several filling fractions. In addition to indications based on energies, e.g., flux insertion and fractional statistics of quasiholes, Chern numbers are obtained. It is shown that FCI states are robust against disorder in the underlying magnetic texture that defines the topological character of the band. We also investigate competition between a FCI state and a charge density wave (CDW) and discuss the effects of particle-hole asymmetry and Fermi-surface nesting. FCI states turn out to be rather robust and do not require very flat bands, but can also arise when filling or an absence of Fermi-surface nesting disfavor the competing CDW. Nevertheless, very flat bands allow FCI states to be induced by weaker interactions than those needed for more dispersive bands.

A large part of this publication has been included in Chapter 5 of this dissertation.

2. *Fractional quantum-Hall liquid spontaneously generated by strongly correlated t_{2g} electrons*
J. W. F. Venderbos, S. Kourtis, J. van den Brink, and M. Daghofer
Physical Review Letters **108**, 126405 (2012)

Abstract: For topologically nontrivial and very narrow bands, Coulomb repulsion between electrons has been predicted to give rise to a spontaneous

fractional quantum-Hall (FQH) state in the absence of magnetic fields. Here we show that strongly correlated electrons in a t_{2g}-orbital system on a triangular lattice self-organize into a spin-chiral magnetic ordering pattern that induces precisely the required topologically nontrivial and flat bands. This behavior is very robust and does not rely on fine-tuning. In order to go beyond mean field and to study the impact of longer-range interactions, we map the low-energy electronic states onto an effective one-band model. Exact diagonalization is then used to establish signatures of a spontaneous FQH state.

Parts of this publication have been included in Chapter 2 of this dissertation.

1. *Exact diagonalization results for resonant inelastic x-ray scattering spectra of one-dimensional Mott insulators*
   S. Kourtis, J. van den Brink, and M. Daghofer
   Physical Review B **85**, 064423 (2012)

   Abstract: We examine the momentum-dependent excitation spectra of indirect as well as direct resonant inelastic x-ray scattering (RIXS) processes in half-filled (extended) Hubbard rings. We determine the fundamental features of the ground-state RIXS response and discuss the experimental conditions that can allow for the low-energy part of these features to be distinguished in one-dimensional copper-oxide materials, focusing particularly on the different magnetic excitations occurring in indirect and direct RIXS processes. We study the dependence of spin and charge excitations on the choice of and detuning from resonance. Moreover, final-state excitation weights are calculated as a function of the core-hole potential strength and lifetime. We show that these results can be used to determine material characteristics, such as the core-hole properties, from RIXS measurements.

   This publication has not been included in this dissertation.

Bibliography

[1] K. von Klitzing, G. Dorda, and M. Pepper, Phys. Rev. Lett. **45**, 494 (1980).

[2] D. C. Tsui, H. L. Stormer, and A. C. Gossard, Phys. Rev. Lett. **48**, 1559 (1982).

[3] R. B. Laughlin, Phys. Rev. Lett. **50**, 1395 (1983).

[4] J. K. Jain, Phys. Rev. Lett. **63**, 199 (1989).

[5] A. Lopez and E. Fradkin, Phys. Rev. B **44**, 5246 (1991).

[6] B. I. Halperin, Phys. Rev. B **25**, 2185 (1982).

[7] C. W. J. Beenakker, Phys. Rev. Lett. **64**, 216 (1990).

[8] A. H. Macdonald, Phys. Rev. Lett. **64**, 220 (1990).

[9] B. Jeckelmann and B. Jeanneret, in The Quantum Hall Effect, Progress in Mathematical Physics, Vol. 45, edited by B. Douçot, V. Pasquier, B. Duplantier, and V. Rivasseau (Birkhäuser, 2005) pp. 55–131.

[10] B. A. Bernevig, L. Susskind, N. Toumbas, and J. H. Brodie, J. High Energy Phys. **02**, 003 (2001).

[11] J. K. Jain, Phys. Today **53**, 39 (2000).

[12] L. Landau and E. Lifshitz, Quantum Mechanics: Non-relativistic Theory, Butterworth Heinemann (Butterworth-Heinemann, 1977).

[13] R. B. Laughlin, Phys. Rev. B **23**, 5632 (1981).

[14] E. Brown, Phys. Rev. **133**, A1038 (1964).

[15] J. Zak, Phys. Rev. **134**, A1602 (1964).

[16] R. Kubo, J. Phys. Soc. Japan **12**, 570 (1957).

[17] Q. Niu, D. J. Thouless, and Y. S. Wu, Phys. Rev. B **31**, 3372 (1985).

[18] R. E. Prange, Phys. Rev. B **23**, 4802 (1981).

[19] R. Joynt and R. E. Prange, Phys. Rev. B **29**, 3303 (1984).

[20] X.-G. Wen and Q. Niu, Phys. Rev. B **41**, 9377 (1990).

[21] D. J. Thouless, M. Kohmoto, M. P. Nightingale, and M. den Nijs, Phys. Rev. Lett. **49**, 405 (1982).

[22] M. Kohmoto, Ann. Phys. (N. Y). **354**, 343 (1985).

[23] R. Tao and Y. S. Wu, Phys. Rev. B **30**, 1097 (1984).

[24] V. J. Goldman and B. Su, Science **267**, 1010 (1995).

[25] R. de Picciotto, M. Reznikov, M. Heiblum, V. Umansky, G. Bunin, and D. Mahalu, Nature **389**, 162 (1997).

[26] L. Saminadayar, D. C. Glattli, Y. Jin, and B. Etienne, Phys. Rev. Lett. **79**, 2526 (1997).

[27] F. Wilczek, Phys. Rev. Lett. **49**, 957 (1982).

[28] D. P. Arovas, J. R. Schrieffer, and F. Wilczek, Phys. Rev. Lett. **53**, 722 (1984).

[29] B. I. Halperin, Phys. Rev. Lett. **52**, 1583 (1984).

[30] R. Tao and Y. S. Wu, Phys. Rev. B **31**, 6859 (1985).

[31] F. Camino, W. Zhou, and V. Goldman, Phys. Rev. B **72**, 075342 (2005).

[32] E.-A. Kim, M. Lawler, S. Vishveshwara, and E. Fradkin, Phys. Rev. Lett. **95**, 176402 (2005).

[33] S. An, P. Jiang, H. Choi, W. Kang, S. H. Simon, L. N. Pfeiffer, K. W. West, and K. W. Baldwin, arXiv:1112.3400v1 (2011).

[34] F. D. M. Haldane, Phys. Rev. Lett. **67**, 937 (1991).

[35] S. He, X. C. Xie, and F. C. Zhang, Phys. Rev. Lett. **68**, 3460 (1992).

[36] M. D. Johnson and G. S. Canright, Phys. Rev. B **49**, 2947 (1994).

[37] B. A. Bernevig and F. D. M. Haldane, Phys. Rev. Lett. **100**, 246802 (2008).

[38] F. D. M. Haldane and E. H. Rezayi, Phys. Rev. B **31**, 2529 (1985).

[39] A. Fayyazuddin and D. Li, Phys. Rev. Lett. **76**, 1707 (1996).

[40] E. H. Rezayi and F. D. M. Haldane, Phys. Rev. Lett. **61**, 1985 (1988).

[41] S. M. Girvin and A. H. Macdonald, Phys. Rev. Lett. **58**, 1252 (1987).

[42] M. Levin and X.-G. Wen, Phys. Rev. Lett. **96**, 3 (2006).

[43] H. Li and F. D. M. Haldane, Phys. Rev. Lett. **101**, 010504 (2008).

[44] D. R. Hofstadter, Phys. Rev. B **14**, 2239 (1976).

[45] Y. Hatsugai and M. Kohmoto, Phys. Rev. B **42**, 8282 (1990).

[46] G. S. Kliros and N. D'Ambrumenil, J. Phys. C Solid State Phys. **3**, 4241 (1991).

[47] C. Albrecht, J. Smet, K. von Klitzing, D. Weiss, V. Umansky, and H. Schweizer, Phys. Rev. Lett. **86**, 147 (2001).

[48] F. D. M. Haldane, Phys. Rev. Lett. **51**, 605 (1983).

[49] S. Kourtis, J. W. F. Venderbos, and M. Daghofer, Phys. Rev. B **86**, 235118 (2012).

[50] F. D. M. Haldane, Phys. Rev. Lett. **61**, 2015 (1988).

[51] Y. H. Wu, J. K. Jain, and K. Sun, Phys. Rev. B **86**, 165129 (2012).

[52] P. W. Anderson and H. Hasegawa, Phys. Rev. **100**, 675 (1955).

[53] E. Müller-Hartmann and E. Dagotto, Phys. Rev. B **54**, R6819 (1996).

[54] M. V. Berry, Proc. R. Soc. A Math. Phys. Eng. Sci. **392**, 45 (1984).

[55] D. Xiao, M. C. Chang, and Q. Niu, Rev. Mod. Phys. **82**, 1959 (2010).

[56] I. Martin and C. D. Batista, Phys. Rev. Lett. **101**, 156402 (2008).

[57] Y. Akagi and Y. Motome, J. Phys. Soc. Japan **79**, 083711 (2010).

[58] S. Kumar and J. van den Brink, Phys. Rev. Lett. **105**, 216405 (2010).

[59] Y. Kato, I. Martin, and C. D. Batista, Phys. Rev. Lett. **105**, 266405 (2010).

[60] K. Ohgushi, S. Murakami, and N. Nagaosa, Phys. Rev. B **62**, 6065 (2000).

[61] Y. Taguchi, Y. Oohara, H. Yoshizawa, N. Nagaosa, and Y. Tokura, Science **291**, 2573 (2001).

[62] B. G. Ueland, C. F. Miclea, Y. Kato, O. A. Valenzuela, R. D. McDonald, R. Okazaki, P. H. Tobash, M. A. Torrez, F. Ronning, R. Movshovich, Z. Fisk, E. D. Bauer, I. Martin, and J. D. Thompson, Nat. Commun. **3**, 1067 (2012).

[63] H. Takatsu, S. Yonezawa, S. Fujimoto, and Y. Maeno, Phys. Rev. Lett. **105**, 137201 (2010).

[64] C.-Z. Chang, J. Zhang, X. Feng, J. Shen, Z. Zhang, M. Guo, K. Li, Y. Ou, P. Wei, L.-L. Wang, Z.-Q. Ji, Y. Feng, S. Ji, X. Chen, J. Jia, X. Dai, Z. Fang, S.-C. Zhang, K. He, Y. Wang, L. Lu, X.-C. Ma, and Q.-K. Xue, Science **340**, 167 (2013).

[65] P. Kurz, G. Bihlmayer, K. Hirai, and S. Blügel, Phys. Rev. Lett. **86**, 1106 (2001).

[66] T. Momoi, K. Kubo, and K. Niki, Phys. Rev. Lett. **79**, 2081 (1997).

[67] J. W. F. Venderbos, M. Daghofer, and J. van den Brink, Phys. Rev. Lett. **107**, 116401 (2011).

[68] J. W. F. Venderbos, S. Kourtis, J. van den Brink, and M. Daghofer, Phys. Rev. Lett. **108**, 126405 (2012).

[69] C. L. Kane and E. J. Mele, Phys. Rev. Lett. **95**, 226801 (2005).

[70] B. A. Bernevig and S.-C. Zhang, Phys. Rev. Lett. **96**, 106802 (2006).

[71] C. L. Kane and E. J. Mele, Phys. Rev. Lett. **95**, 146802 (2005).

[72] L. Fu and C. Kane, Phys. Rev. B **76**, 045302 (2007).

[73] B. A. Bernevig, T. L. Hughes, and S.-C. Zhang, Science **314**, 1757 (2006).

[74] M. König, S. Wiedmann, C. Brüne, A. Roth, H. Buhmann, L. W. Molenkamp, X.-L. Qi, and S.-C. Zhang, Science **318**, 766 (2007).

[75] D. Hsieh, D. Qian, L. Wray, Y. Xia, Y. S. Hor, R. J. Cava, and M. Z. Hasan, Nature **452**, 970 (2008).

[76] A. Schnyder, S. Ryu, A. Furusaki, and A. Ludwig, Phys. Rev. B **78**, 195125 (2008).

[77] S. Ryu, A. P. Schnyder, A. Furusaki, and A. W. W. Ludwig, New J. Phys. **12**, 065010 (2010).

[78] C. Lanczos, J. Res. Natl. Bur. Stand. (1934). **45**, 255 (1950).

[79] C. Lanczos, J. Res. Natl. Bur. Stand. (1934). **49**, 33 (1952).

[80] T. Neupert, L. Santos, C. Chamon, and C. Mudry, Phys. Rev. Lett. **106**, 236804 (2011).

[81] K. Sun, Z. Gu, H. Katsura, and S. Das Sarma, Phys. Rev. Lett. **106**, 236803 (2011).

[82] X.-G. Wen, F. Wilczek, and A. Zee, Phys. Rev. B **39**, 11413 (1989).

[83] C. Nayak, Phys. Rev. B **62**, 4880 (2000).

[84] S. Chakravarty, R. B. Laughlin, D. Morr, and C. Nayak, Phys. Rev. B **63**, 094503 (2001).

[85] L. Li, Y. Wang, S. Komiya, S. Ono, Y. Ando, G. D. Gu, and N. P. Ong, Phys. Rev. B **81**, 054510 (2010).

[86] S. Tewari, C. Zhang, V. Yakovenko, and S. Das Sarma, Phys. Rev. Lett. **100**, 217004 (2008).

[87] P. Kotetes and G. Varelogiannis, Phys. Rev. Lett. **104**, 106404 (2010).

[88] J. Levallois, K. Behnia, J. Flouquet, P. Lejay, and C. Proust, Europhys. Lett. **85**, 27003 (2009).

[89] K. Izawa, K. Behnia, Y. Matsuda, H. Shishido, R. Settai, Y. Onuki, and J. Flouquet, Phys. Rev. Lett. **99**, 147005 (2007).

[90] X. Chen, S. Dong, and J.-M. Liu, Phys. Rev. B **81**, 064420 (2010).

[91] F. Ning, S. Golin, K. Ahilan, T. Imai, G. Shu, and F. Chou, Phys. Rev. Lett. **100**, 086405 (2008).

[92] E. J. Bergholtz and Z. Liu, Int. J. Mod. Phys. B **27**, 1330017 (2013).

[93] S. A. Parameswaran, R. Roy, and S. L. Sondhi, Comptes Rendus Phys. **14**, 816 (2013).

[94] N. Y. Yao, A. V. Gorshkov, C. R. Laumann, A. M. Läuchli, J. Ye, and M. D. Lukin, Phys. Rev. Lett. **110**, 185302 (2013).

[95] P. Ghaemi, J. Cayssol, D. N. Sheng, and A. Vishwanath, Phys. Rev. Lett. **108**, 266801 (2012).

[96] A. G. Grushin, A. Gómez-León, and T. Neupert, Phys. Rev. Lett. **112**, 156801 (2014).

[97] D. Xiao, W. Zhu, Y. Ran, N. Nagaosa, and S. Okamoto, Nat. Commun. **2**, 596 (2011).

[98] Y. Onose, T. Ideue, H. Katsura, Y. Shiomi, N. Nagaosa, and Y. Tokura, Science **329**, 297 (2010).

[99] G. Grüner, Rev. Mod. Phys. **60**, 1129 (1988).

[100] J. M. Tranquada, B. J. Sternlieb, J. D. Axe, Y. Nakamura, and S. Uchida, Nature **375**, 561 (1995).

[101] T. Wu, H. Mayaffre, S. Krämer, M. Horvatić, C. Berthier, W. N. Hardy, R. Liang, D. A. Bonn, and M.-H. Julien, Nature **477**, 191 (2011).

[102] G. Ghiringhelli, M. Le Tacon, M. Minola, S. Blanco-Canosa, C. Mazzoli, N. B. Brookes, G. M. De Luca, a. Frano, D. G. Hawthorn, F. He, T. Loew, M. Moretti Sala, D. C. Peets, M. Salluzzo, E. Schierle, R. Sutarto, G. a. Sawatzky, E. Weschke, B. Keimer, and L. Braicovich, Science **337**, 821 (2012).

[103] H. Seo, C. Hotta, and H. Fukuyama, Chem. Rev. **104**, 5005 (2004).

[104] J. Wilson, F. Di Salvo, and S. Mahajan, Adv. Phys. **24**, 117 (1975).

[105] M. Vojta, Adv. Phys. **58**, 699 (2009).

[106] E. Tang, J.-W. Mei, and X.-G. Wen, Phys. Rev. Lett. **106**, 236802 (2011).

[107] D. N. Sheng, Z.-C. Gu, K. Sun, and L. Sheng, Nat. Commun. **2**, 389 (2011).

[108] Y.-F. Wang, Z.-C. Gu, C.-D. Gong, and D. N. Sheng, Phys. Rev. Lett. **107**, 146803 (2011).

[109] N. Regnault and B. A. Bernevig, Phys. Rev. X **1**, 021014 (2011).

[110] Y.-L. Wu, B. A. Bernevig, and N. Regnault, Phys. Rev. B **85**, 075116 (2012).

[111] T. Liu, C. Repellin, B. A. Bernevig, and N. Regnault, Phys. Rev. B **87**, 205136 (2013).

[112] A. M. Läuchli, Z. Liu, E. J. Bergholtz, and R. Moessner, Phys. Rev. Lett. **111**, 126802 (2013).

[113] M. Trescher and E. J. Bergholtz, Phys. Rev. B **86**, 241111(R) (2012).

[114] S. Yang, Z.-C. Gu, K. Sun, and S. Das Sarma, Phys. Rev. B **86**, 241112(R) (2012).

[115] F. Wang and Y. Ran, Phys. Rev. B **84**, 241103(R) (2011).

[116] Z. Liu, E. J. Bergholtz, H. Fan, and A. M. Läuchli, Phys. Rev. Lett. **109**, 186805 (2012).

[117] A. Sterdyniak, C. Repellin, B. A. Bernevig, and N. Regnault, Phys. Rev. B **87**, 205137 (2013).

[118] A. G. Grushin, T. Neupert, C. Chamon, and C. Mudry, Phys. Rev. B **86**, 205125 (2012).

[119] B. A. Bernevig and N. Regnault, Phys. Rev. B **85**, 075128 (2012).

[120] X.-L. Qi, Phys. Rev. Lett. **107**, 126803 (2011).

[121] Y.-L. Wu, N. Regnault, and B. A. Bernevig, Phys. Rev. B **86**, 085129 (2012).

[122] C. H. Lee, R. Thomale, and X.-L. Qi, Phys. Rev. B **88**, 035101 (2013).

[123] G. Murthy and R. Shankar, Phys. Rev. B **86**, 195146 (2012).

[124] S. A. Parameswaran, R. Roy, and S. L. Sondhi, Phys. Rev. B **85**, 241308 (2012).

[125] M. O. Goerbig, Eur. Phys. J. B **85**, 15 (2012).

[126] D. N. Sheng, X. Wan, E. H. Rezayi, K. Yang, R. N. Bhatt, and F. D. M. Haldane, Phys. Rev. Lett. **90**, 256802 (2003).

[127] S. Yang, K. Sun, and S. Das Sarma, Phys. Rev. B **85**, 205124 (2012).

[128] S. Kourtis, T. Neupert, C. Chamon, and C. Mudry, Phys. Rev. Lett. **112**, 126806 (2014).

[129] P. Fendley, K. Schoutens, and J. de Boer, Phys. Rev. Lett. **90**, 120402 (2003).

[130] P. Fendley and K. Schoutens, Phys. Rev. Lett. **95**, 046403 (2005).

[131] N. G. Zhang and C. L. Henley, Phys. Rev. B **68**, 014506 (2003).

[132] N. G. Zhang and C. L. Henley, Eur. Phys. J. B **38**, 409 (2004).

[133] S. Kourtis and M. Daghofer, arXiv:1305.6948 (2013).

[134] T. Neupert, L. Santos, S. Ryu, C. Chamon, and C. Mudry, Phys. Rev. B **84**, 165107 (2011).

[135] F. Trousselet, A. Ralko, and A. M. Oleś, Phys. Rev. B **86**, 014432 (2012).

[136] C. Hotta and N. Furukawa, Phys. Rev. B **74**, 193107 (2006).

[137] S. Nishimoto, M. Shingai, and Y. Ohta, Phys. Rev. B **78**, 035113 (2008).

[138] L. Cano-Cortés, A. Ralko, C. Février, J. Merino, and S. Fratini, Phys. Rev. B **84**, 155115 (2011).

[139] J. Merino, A. Ralko, and S. Fratini, Phys. Rev. Lett. **111**, 126403 (2013).

[140] C. Chamon and C. Mudry, Phys. Rev. B **86**, 195125 (2012).

[141] A. Kol and N. Read, Phys. Rev. B **48**, 8890 (1993).

[142] S. Wessel and M. Troyer, Phys. Rev. Lett. **95**, 127205 (2005).

[143] G.-W. Chern, A. Rahmani, I. Martin, and C. D. Batista, arXiv:1212.3617 (2012).

[144] H. Ishizuka and Y. Motome, Phys. Rev. B **87**, 081105 (2013).